

2012

# Self-organization of contractile ring in fission yeast: aggregation kinetics and instability regimes

Ojkic Nikola  
*Lehigh University*

Follow this and additional works at: <http://preserve.lehigh.edu/etd>

---

## Recommended Citation

Nikola, Ojkic, "Self-organization of contractile ring in fission yeast: aggregation kinetics and instability regimes" (2012). *Theses and Dissertations*. Paper 1070.

This Dissertation is brought to you for free and open access by Lehigh Preserve. It has been accepted for inclusion in Theses and Dissertations by an authorized administrator of Lehigh Preserve. For more information, please contact [preserve@lehigh.edu](mailto:preserve@lehigh.edu).

# Self-organization of contractile ring in fission yeast: aggregation kinetics and instability regimes

by

Nikola Ojkić

A Dissertation

Presented to the Graduate and Research Committee

of Lehigh University

in Candidacy for the Degree of

Doctor of Philosophy

in

Physics Department

Lehigh University

May 2012

© 2012 Copyright  
Nikola Ojkic

Approved and recommended for acceptance as a dissertation in partial fulfillment of the requirements for the degree of Doctor of Philosophy.

Nikola Ojkic  
Self-organization of contractile ring in fission yeast: aggregation kinetics and instability regimes

10/04/12

---

Defense Date

---

Dimitrios Vavylonis  
Dissertation Director

19/04/12

---

Approved Date

Committee Members:

---

Daniel Ou-Yang

---

Slava V. Rotkin

---

Michael Stavola

---

Svetlana Tatić-Lučić

## ACKNOWLEDGMENTS

I would like to thank my mother Anđelija Ojkić, my father Radovan Ojkić, and my brother Nemanja Ojkić for their endless love and support.

Especially, I would like to thank my physics professor Edita Čehak for her enthusiasm during my early studies of physics and math.

During my PhD studies my grandmother Marija Stefanović passed away. I would always be grateful for her love and support.

At the end, I would like to thank my PhD advisor Dimitrios Vavylonis for sharing his great knowledge, effort, ambition, and endless passion for science.

## TABLE OF CONTENTS

List of Figures .....	vii
List of Tables .....	x
Abstract .....	1
<b>1 Introduction.....</b>	<b>3</b>
<b>2 Search, capture, pull, and release model.....</b>	<b>10</b>
<b>3 Stochastic aggregation model.....</b>	<b>15</b>
<b>3.1 Homogeneous 2D system.....</b>	<b>17</b>
<b>3.2 2D band of nodes.....</b>	<b>22</b>
<b>3.3 Comparison to experiment.....</b>	<b>24</b>
<b>4 Node condensation into a ring in a model that includes node alignment.....</b>	<b>26</b>
<b>4.1 Model of SCPR with local node alignment.....</b>	<b>29</b>
<b>4.2 Simulation results.....</b>	<b>35</b>
<b>4.3 Discussion.....</b>	<b>46</b>

<b>5</b>	<b>Role of actin filament cross-linkers <math>\alpha</math>-actinin and fimbrin.....</b>	<b>49</b>
<b>5.1</b>	<b>Cross-linker depletion experiments.....</b>	<b>51</b>
<b>5.2</b>	<b>Cross-linker overexpression experiments.....</b>	<b>54</b>
<b>6</b>	<b>Model of role of actin cross-linker in ring assembly.....</b>	<b>57</b>
<b>6.1</b>	<b>Model.....</b>	<b>58</b>
<b>6.2</b>	<b>Results.....</b>	<b>63</b>
<b>6.3</b>	<b>Discussion.....</b>	<b>75</b>
<b>7</b>	<b>Conclusion.....</b>	<b>77</b>
Appendix	.....	79
Supplementary figures	.....	87
Supplementary tables	.....	89
Bibliography	.....	90
Vita	.....	102

## LIST OF FIGURES

1	Confocal microscopy images of dividing wild type cells expressing myosin marker Rlc1p-3GFP.....	4
2	Initial node distribution along long axis of the cell.....	5
3	Actin and myosin distribution during ring formation process.....	6
4	Defective actomyosin aggregates in different mutants.....	7
5	SCPR model of node condensation.....	11
6	Properties of actin filaments and node movements during early stages of ring formation.....	13
7	Cartoon of 2D stochastic aggregation model.....	16
8	Monte Carlo simulations of node aggregation showing kinetics of clump formation in Regime 1.....	19
9	Simulations for Regime 2.....	21
10	Simulations of condensation of a band of nodes.....	23
11	Cartoon of ring formation. In the SCPR model, nodes condense into rings through connections established by actin filaments.....	27
12	The search, capture, pull, and release model with the addition of local node alignment.....	30
13	Snapshots of simulations showing the initial node distribution and nodes condensed into a ring structure.....	36
14	Results of Monte Carlo simulations of a model with local node alignment.....	39
15	Statistics and snapshots of simulations using parameters corresponding to Point A.....	41
16	Same as Figure 15 but for Point B.....	42



17	Snapshots of simulations for <i>cdc25-22</i> cells showing the formation of meshwork structures.....	44
18	Results of simulations showing the ratio of band width at 500 s over initial band width versus unconnected filament turnover time $t_{\text{turn}}$ and initial band width.....	46
19	Cartoon of actin filament cross-linkers.....	50
20	Normal node condensation during contractile-ring assembly depends on $\alpha$ -actinin Ain1 and fimbrin Fim1.....	53
21	Ain1 overexpression promotes the formation of stable linear structures during contractile-ring formation.....	55
22	Summary of basic processes of SCPR model with actin filament cross-linking.....	60
23	Snapshots of 2D simulations of node condensation for different values of parameter $\alpha = r_{\text{cross}}/l_0$ .....	65
24	Width and largest gap of node bands in experiments and simulations...	67
25	Node band porosity and number of cross-linkers in experiments and simulations.....	68
26	Dependence of node aggregate structures on cross-linker model parameters.....	70
27	Model prediction of cooperation between Myo2 activity and Ain1 cross-linking.....	72
28	Experimental result showing cooperation between Myo2 activity and Ain1 cross-linking.....	74
29	Simulations of node condensation in <i>cdc25-22</i> cells.....	75
30	Tangent correlation function analysis of semi-flexible filaments in thermal equilibrium.....	81

31	Curvature distribution of semi-flexible filaments.....	82
32	Cartoon showing how the Fourier modes are calculated.....	83
33	Fourier mode analysis.....	84
34	Dynamic properties of semi-flexible filaments in the thermal equilibrium.....	86
S1	Node condensation dependence on model parameters.....	87
S2	Node movement statistics.....	88

## LIST OF TABLES

S1	SCPR model parameters used in simulations of Chapter 6.....	89
----	---	----

## ABSTRACT

One of the most important steps during the division of eukaryotic cells is the formation of the actomyosin contractile ring. The constriction of the contractile ring drives the mechanical splitting of a mother cell in two daughter cells, a process known as cytokinesis. A model organism for investigating cytokinesis is fission yeast (*S. pombe*) where the contractile ring forms through the condensation of a broad band of  $\approx 65$  cortical “nodes”. The nodes are macromolecular complexes containing several dozens of motor-protein myosin-II (Myo2p), a few actin filament nucleators (formin Cdc12p), and other proteins. Recent experiments showed that cortical nodes in various cytokinesis mutants form clumps and actomyosin meshworks instead of rings, demonstrating a fascinating flexibility of the cytoskeletal system.

The focus of my work has been to describe the biophysical mechanism of clump/ring/meshwork formation in fission yeast through quantitative modeling. My work was based on the previously-proposed Search, Capture, Pull, and Release (SCPR) model of how the nodes self-organize into rings. In this model, myosin motors associated with nodes pull on dynamic actin filaments and move the nodes toward one another. The SCPR model predicted clump and ring formation numerically but did not address how meshworks form.

First, to understand how clump and ring formation depends on model parameters, I developed a stochastic aggregation model that is a simplified version of the original SCPR model. This simplified SCPR model allowed me to derive scaling arguments that described regimes of clump and ring formation as a function of model parameters. I

found that bands of nodes condense into rings when the average length of actin filaments is larger than the initial band width. If the average length of actin filaments is smaller than the band width, clumps form due to node density fluctuations, consistent with observations in *cdc12-112* mutants.

Second, to model meshwork formation, I proposed an additional local node alignment mechanism. With this new model I successfully described meshwork structure formation as observed in *cdc25-22* mutant cells. This result motivated new experimental investigations of the molecular origin of the proposed local alignment mechanism.

Third, to study the local alignment mechanism we collaborated with Damien Laporte and Jian-Qiu Wu at The Ohio State University. We investigated the role of actin filament cross-linkers alpha-actinin and fimbrin during ring formation in fission yeast. We found that alpha-actinin and fimbrin stabilize the actin cytoskeleton and modulate node movement, which promotes the formation of linear structures and prevents nodes from aggregating into clumps, thus allowing normal ring formation. I developed numerical simulations of node aggregation with actin filaments as semi-flexible polymers that describe how different actomyosin aggregates form depending on cross-linker concentrations. By varying the degree of cross-linking from low to high, my numerical simulations showed transitions from clumps to rings to mesworks, reproducing experimental observations.

Together, by combining experiments by collaborators, analytical calculations, and simulations, our work provides an initial mechanistic description to one of the most complex but fundamental processes in cell biology.

# 1. Introduction

The ability of eukaryotic cells to move and change shape relies on the plasticity of the cellular cytoskeleton. The molecular components of the cytoskeleton (actin, tubulin, and molecular motors) spontaneously come together to generate filamentous structures over scales much larger than the size of individual proteins. Cooperativity among various protein components is essential for the formation of cytoskeletal structures at the cell scale. Understanding the physics that govern the assembly and cooperative mechanisms in these adaptive materials is an area of considerable current studies [1-11]. These studies have provided insights into how cells organize their cytoskeleton to form subcellular structures such as stress fibers [12], contractile rings [8, 13, 14], and mitotic spindles [15, 16].

One of the best examples of a subcellular self-organization process driven by the cytoskeleton is the assembly of the actomyosin contractile ring during cytokinesis. The contractile ring plays a role in mechanical separation of mother cell in two daughter cells, see Figure 1. One of the model organisms for the study of cytokinesis is fission yeast [17-23]. In fission yeast the contractile ring forms from a condensation of a broad band of  $\approx 65$  “nodes”, see Figure 1. The nodes are large macromolecular complexes bound to the inner part of the cell membrane. Nodes contain motor protein myosin-II (Myo2p) and nucleators (formin Cdc12p) for actin filament polymerization [17], and other proteins [24].

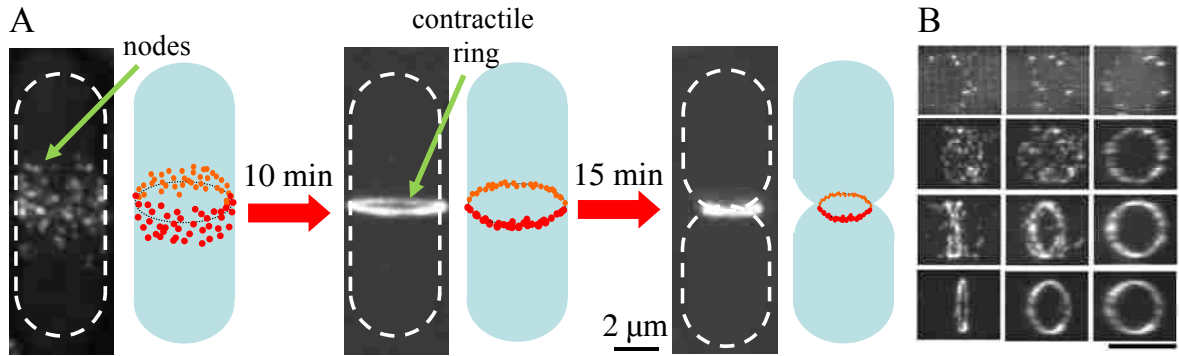


**Figure 1:** Confocal microscopy images of dividing wild type cells expressing myosin marker Rlc1p-3GFP. (A) A broad band of nodes bound in the inner part of the cell membrane condenses into a ring in  $\approx 10$  minutes. The ring subsequently constricts [25]. (B) 3D reconstructions showing formation of the contractile ring from a band of cortical nodes. Each row shows a cell at a different stage of ring assembly. Each column shows the same cell rotated successively by  $45^\circ$  around an axis normal to the long axis of the cell [13]. Scale bar 5  $\mu\text{m}$ .

The first stage of ring assembly is the formation of the stationary cortical nodes in the cell cortex [17, 24]. During this stage, node components Myo2p and Cdc12p are recruited to the cortical nodes. Each node contains  $\approx 55$  Myo2p motor proteins and  $\approx 2-4$  molecules of formin Cdc12p [17, 24, 26]. The initial node distribution is approximately Gaussian along the long axis of the cell with a maximum in the middle, see Figure 2. The nodes remain localized just beneath the cell membrane throughout the ring formation process, see Figure 1B.

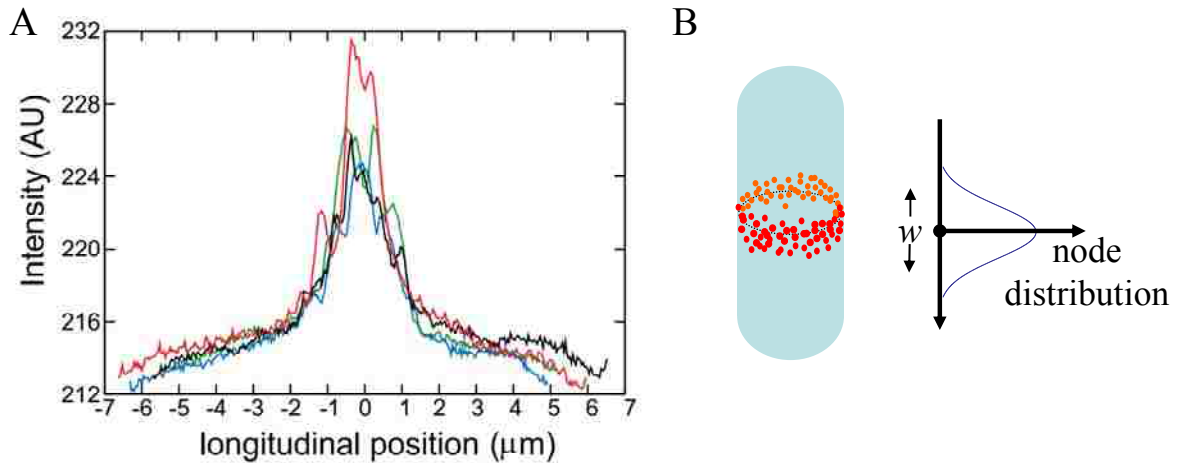


**Figure 2:** Initial node distribution along long axis of the cell. (A) Average intensity of Rlc1p-3GFP fluorescence along the long axes of four cells with fully formed but uncondensed broad bands [13]. (B) Cartoon illustrating that node distribution at early stages of ring assembly is approximately Gaussian.

The second stage of ring assembly is the stage of node coalescence into rings. After about 10 min once the nodes are formed, they start to exhibit a biased random walk toward the cell middle with many starts and stops [13]. During this stage actin filaments polymerized through formin Cdc12p form a dynamic network in the middle of the cell that connects nodes with one another (see Figure 3). The force exerted by myosin motors on actin filaments is believed to generate the force that is required for the biased node movement [13, 17].



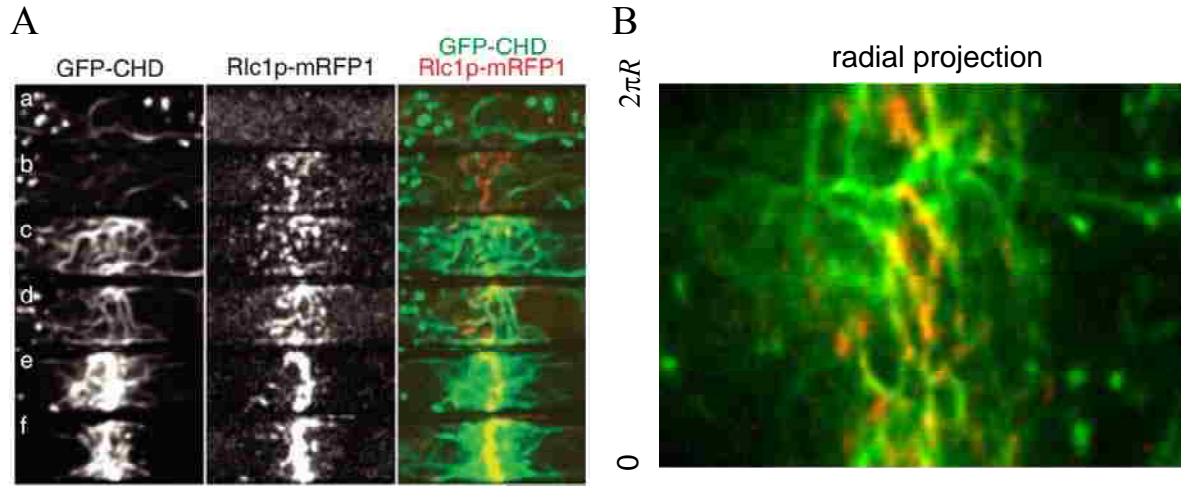


**Figure 3:** Actin and myosin distribution during ring formation process. Cells express markers for both myosin light chain (Rlc1p-mRFP1) and actin filaments (GFP-CHD). (A) Six cells from the same field arranged according to cell-cycle stage showing networks of actin filaments connecting nodes. Left column: actin filaments; middle column: myosin nodes; right column: dual color image showing actin and myosin in the same cell. Scale bar, 5 $\mu$ m. (B) Radial projection of the cell cortex during ring formation process in *cdc25-22* cells [13].

Many cells with mutations in the proteins involved in cytokinesis fail to condense the nodes into rings. For example, cells expressing mutated formin Cdc12p-112 (a temperature-sensitive mutation), form local clumps of nodes instead of contractile rings, see Figure 4A. Clump structures are also observed in mutants with defective protein cofilin, an actin filament severing agent, that contributes to actin turnover [27]. Similarly, in cells with increased level of actin filament cross-linker alpha-actinin meshworks of actomyosin structures form instead of rings, see Figure 4B.

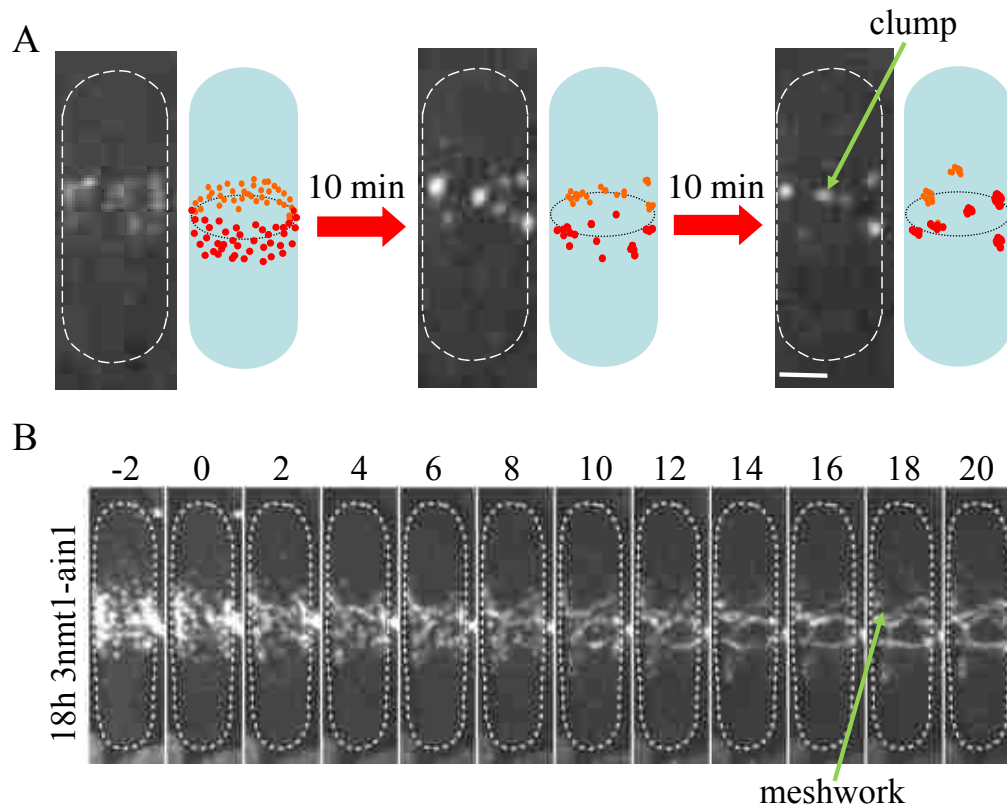


**Figure 4:** Defective actomyosin aggregates in different mutants. (A) Images of mitotic *cdc12-112* cells (formin mutants) expressing Rlc1p-GFP at the restrictive temperature: clumps form instead of rings [25, 28]. Scale bar, 2  $\mu\text{m}$ . (B) Images of cells overexpressing *Ain1*; nodes marked with Rlc1-tdTomato condensate into mesworks instead of rings, see Chapter 5. Time is in min.

The results of Figure 4 demand quantitative modeling and better understanding of biophysical principles that govern formation and stability of cortical actomyosin aggregates. Such models can propose testable hypothesis that can be of the greatest importance for biomedical and health research.

Therefore, the focus of my PhD work was developing theoretical models to understand the mechanism of how different node aggregates (rings/clumps/meshworks) arise through dynamic actomyosin interactions. I started by further developing a previously-proposed model of node coalescing into rings: the “search, capture pull and

release” (SCPR) model [13], see Chapter 2. This is a kinetic model of transient node interaction that proposes a mechanism for the origin of cortical node movements. In Chapter 2, I briefly introduce the SCPR model and supporting experimental evidences.

Chapter 3 describes a stochastic aggregation model that I developed [25]. This stochastic model is a simplified version of the original SCPR model and allowed me to derive scaling arguments that described regimes of clump and ring formation as a function of model parameters. I found that bands of nodes condense into rings when the average length of actin filaments is larger than the initial band width. If the average length of actin filaments is smaller than the band width, clumps form due to node density fluctuations, consistent with observations in *cdc12-112* mutants, see Figure 4A. The work of Chapter 3 is published in 2010 (N. Ojkic and D. Vavylonis, "Kinetics of Myosin Node Aggregation into a Contractile Ring", *Physical Review Letters* , **105**, 048102, 2010).

Chapter 4 describe how I further developed the SCPR model by introducing a ‘local alignment’ mechanism [29]. This new proposed mechanism was developed in order to understand aggregation of nodes into observed meshworks and star-like-structures in actin cross-linker mutants, as well as double ring structures observed in cells with increased level of actin cross-linker alpha-actinin, see Figure 4B. The work of Chapter 4 was published in 2011 (N. Ojkic, J.-Q. Wu and D. Vavylonis, “Model of Myosin Node Aggregation into a Contractile Ring: the Effect of Local Alignment”, *Journal of Physics: Condensed Matter*, **23**, 374103, 2011).

In Chapters 5 and 6 I present experimental work by Damien Laporte and Jian-Qiu Wu and my quantitative modeling on the role of actin cross-linkers during ring formation process. This collaborative work addresses a possible molecular mechanism for the local

node alignment of Chapter 4. Using numerical simulations we proposed a mechanistic role of actin cross-linker proteins during ring formation process. With these numerical simulations we explored ability of contractile actomyosin components to form rings and the origin of various condensation defects such as clumps, stars and mesworks. The collaborative work of Chapters 5 and 6 is currently under review in the *Molecular Biology of the Cell* (D. Laporte, N. Ojkic, D. Vavylonis and J.-Q. Wu).

## 2. Search, capture, pull, and release model

The Search, Capture, Pull and Release (SCPR) model was developed by Vavylonis *et al.*, see Figure 5 [13]. The mechanism of this model is based on the list of proteins found in the nodes and their known functions [13]. Each node contains actin filament nucleators formin Cdc12p and motor proteins Myo2p [18, 24]. It was previously shown that formins are actin nucleators that can increase the rate of polymerization while being processively attached to a barbed end of the filament [30-34]. As a filament is polymerized out of node the formin attached to the filament barbed end is assumed to remain processively at the node [13]. In the SCPR model, two actin filaments are assumed to polymerize out of each node along a random direction and along the cell cortex, see Figure 5B. This is consistent with experiments showing random actin filament orientation during ring assembly see Figure 6A. When a polymerizing filament tip comes in the vicinity of another node, the myosin in the target node grabs the filament and exerts a force resulting in movement of nodes toward each other, see Figure 5B. All actin filaments (connected and polymerizing) are assumed to have a typical life-time, since the simulations with permanent connections between each two nearest neighbors generates clumps, see Figure 5C top panels. Furthermore, severing of growing actin filaments is experimentally observed [13]. Actin filament severing agent cofilin is believed to be at least responsible for this process [27, 35, 36]. The typical life-time of filaments connecting two nodes was estimated to be  $\tau_{\text{break}}$

= 20s, while the typical lifetime of freely elongating filaments is  $\tau_{\text{turn}} = 20\text{s}$  [13].

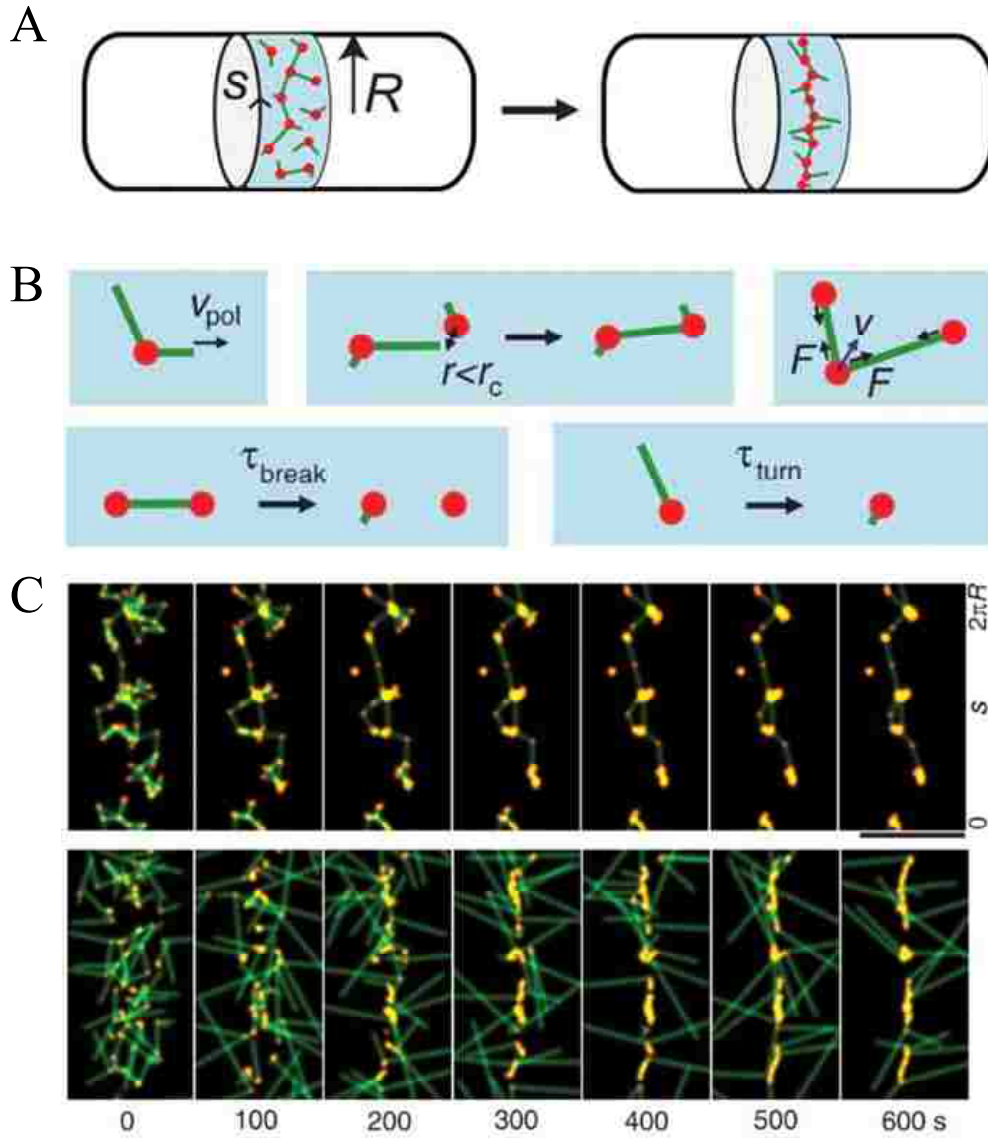


**Figure 5:** SCPR model of node condensation. (A) SCPR model [13]. (B) Prediction of SCPR model for different set of parameters as a function of time [13]. Nodes shown in red; actin filaments in green. (C) Cartoon showing condensation of band of nodes into a ring. The  $y$  axis represents arc length around cell cortex;  $x$  axis is along the long axis of the cell. The top row corresponds to a set of parameter values where nodes form permanent connections and lead to the clumps; the bottom row predicts smooth ring formation using parameters obtained from wild type cells with a filament lifetime of 20s.

Filament severing allows polymerization of a new actin filament along a new random direction. In experiments, actin filaments were observed to grow to a length of order  $1\mu\text{m}$  (see Figure 6B). The result of random connection establishment, traction, and connection breakage resulted in a pattern of stochastic start-stop node motion, similarly to the pattern of motion observed in experiments in which nodes were observed to move toward each other every 15s with an average speed of order  $30\text{nm/s}$  (see Figure 6C, D).

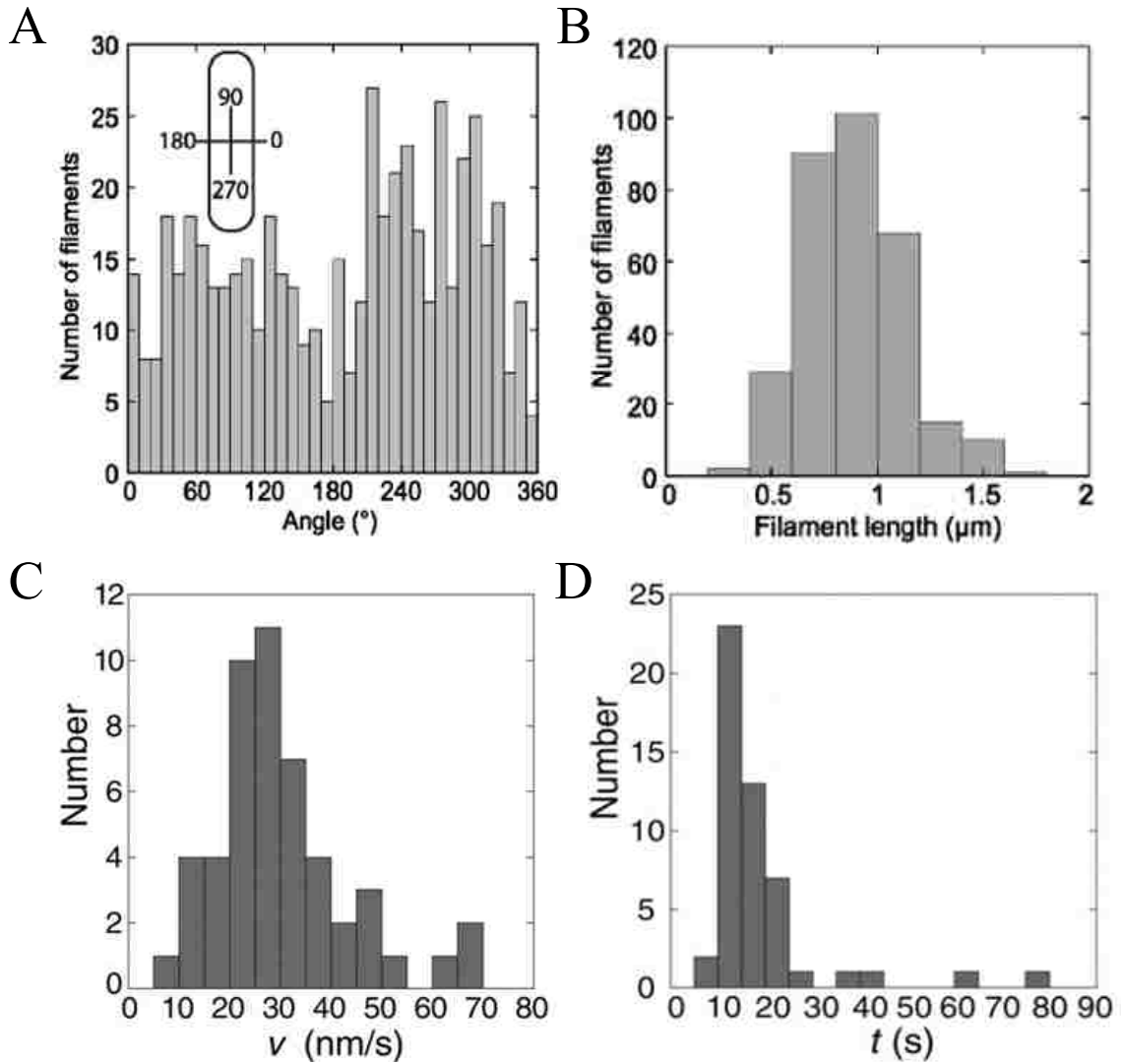


**Figure 6:** Properties of actin filaments and node movements during early stages of ring formation. (A) Distribution of actin filament orientation imaged at the top and bottom of the cell [37]. (B) Histogram of length of actin filaments emerging from a single node [37]. (C) Histogram of node velocity [13]. (D) Histogram of time duration of each node movement [13].

Using parameter values obtained from experiments, numerical simulations of the model generate rings out of nodes within a time consistent with experiment (see Figure 5C, bottom). However, using parameter values different from those observed in



experiments, the model generates local clumps of node aggregates instead of rings (Figure 5C, top). These clumps are similar to those observed in experiments (Figure 4A).

One of the aims of my work was to go beyond the numerical simulations of reference [13] in order to: *(i)* better understand the robustness of ring assembly versus clump formation using numerical simulations and scaling arguments, *(ii)* model the effects of actin cross-linking proteins that were not included in the SCPR model, and *(iii)* to develop and test model predictions in collaboration with the lab of Jian-Qiu Wu (The Ohio State University).

Actin asters that are seen occasionally during fission yeast contractile ring assembly have provided evidence for the ‘leading cable’ model, an alternative to SCPR [20, 38-40]. In this model a Cdc12p spot nucleates many actin filaments at the cell cortex (‘asters’) that initiate the process of ring assembly. However the observed spot has been shown to disappear without nucleating actin filaments [26]. Therefore, due to the lack of further evidence, I will assume actin is nucleated at multiple sites in the nodes as in the SCPR model.

### **3. Stochastic aggregation model**

Recently, Hachet and Simanis [28] observed that cells expressing mutated actin nucleator formin Cdc12-112 form clumps rather than continuous rings, see Figure 1 and Figure 4A. To better understand the mechanism of clumps vs ring formation, here I present numerical results of a stochastic node aggregation model. This model is a simplified version of the original SCPR model described in Chapter 2. The simple stochastic aggregation model allowed us to develop scaling arguments that show dependence of clump formation on SCPR model parameters. Also, the stochastic aggregation model gave us comprehensive description of aggregation instabilities that were just numerically studied in the original SCPR model [13].

In the model, nodes with attached myosin form clumps through connections by filaments of varying length. This mechanism differs from previous studies in which filaments collapse into bundles through mobile motors [1, 3, 6, 10, 41, 42].

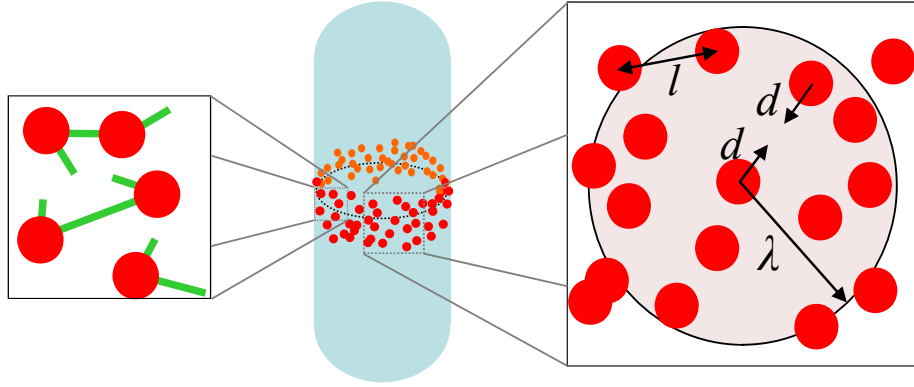


**Figure 7:** Cartoon of 2D stochastic aggregation model. Left: nodes attract one another through transient connections by actin filaments polymerized by formins at the nodes. Right: model parameters.  $l$ , average distance between neighboring nodes;  $d$ , size of pairwise node movement per connection event; and  $\lambda$ , typical length of actin filaments.

We consider the model of Figure 7 in which each node on a 2D surface representing the inner cell membrane can establish a connection with another node at a distance  $r$  away with rate:

$$q(r) = Q \frac{a}{r} e^{-r/\lambda} . \quad 1$$

Here, the  $1/r$  dependence reflects the diluteness in the search process as the actin filaments grow out of Cdc12p nucleators in the nodes,  $Q$  is a rate that depends on total number of Cdc12p per node, and the exponential term introduces an upper cutoff of order  $\lambda$  representing the typical length at which actin filaments grow before severing by cofilin. Parameter  $a$  is a capture radius: it represents the distance over which the tips of the growing actin filaments are captured by target nodes [13]. Myosin pulling and severing of connections is modeled as follows. When a connection between two nodes is established, the nodes move toward one another by distance  $d$  instantaneously (when  $r < 2d$ , they are moved by  $r/2$  such that they overlap). After this movement, the connection is assumed broken. For simplicity, excluded volume interactions are neglected.

The model of Figure 7 combines two types of node movement: (i) active diffusion due to the randomness in connections with neighbors (described by a diffusion coefficient,  $D$ ), and (ii) directed transport towards regions of higher density with local velocity  $v$ . Monte Carlo simulations showed that active diffusion is not strong enough to maintain an initially homogeneous 2D state of nodes at initial concentration  $c$ . Plots of the mean square node displacement vs time indicate that an initial diffusive  $t^{1/2}$  regime is followed by directed transport and clump formation, see Figure 8. The following scaling arguments that neglect numerical prefactors describe the kinetics of clump formation observed in simulations.

### 3.1. Homogeneous 2D system

In a homogeneous 2D system, clumps form near regions that happen to have a higher density initially due to Poisson fluctuations around the average concentration. Consider a node at  $t = 0$ . Since the step size of the node's walk is  $d$ , its initial diffusion coefficient is

$$D_0 \approx Q_{\text{tot}} d^2, \quad Q_{\text{tot}} \equiv \int_0^\infty c q(r) 2\pi r dr \approx Q \frac{a\lambda}{l^2}. \quad 2$$

Here  $Q_{\text{tot}}$  is the total rate of making connections to other nodes and  $l \equiv c^{-1/2}$  is the typical distance between neighboring nodes, see Figure 7. Note that most connections are made at distance of order  $\lambda$  since the integral in equation above is dominated by  $r \sim \lambda$ . Thus a node can connect with approximately  $N_\lambda \equiv \lambda^2/l^2$  nodes at distance of order  $\lambda$ . The

initial Poisson fluctuations in the number of nodes over such a distance is  $\Delta N_\lambda = N_\lambda^{1/2} = \lambda/l$ . Therefore, initially, there is a direction in space along which the node is attracted to by an excess of  $\Delta N_\lambda$  nodes. The node will move along this direction with an initial velocity:

$$v_0 \approx Q'd\Delta N_\lambda = Q'd \lambda / l, \quad Q' \equiv Q a / \lambda, \quad 3$$

where  $Q'$  is the connection rate for nodes separated by distance  $\lambda$ . The expressions in Equations 2 and 3 define a length scale  $l^*$  and time  $t^*$  after which transport dominates diffusion,  $l^* = v_0 t^* = (D_0 t^*)^{1/2}$  [43],

$$l^* = \lambda d / l, \quad t^* = 1 / Q'. \quad 4$$

There are two asymptotic limits: (1) Regime 1 (R1):  $d \ll l$ , or, equivalently,  $l^* \ll \lambda$ , and (2) Regime 2 (R2):  $d \gg l$  ( $l^* \gg \lambda$ ). Throughout this Chapter we consider  $d \ll \lambda$ , and  $l \ll \lambda$ .

For R1, active diffusion is not strong enough to move nodes over distances beyond their interaction range. Thus, nodes continue to move and coalesce with speed  $v_0$  according to the initial concentration fluctuations past  $t^*$ . This linear transport of nodes persists until nodes travel a distance of order  $\lambda$ ; at about this point in time, regions of high initial density absorb the nodes of the less dense regions, see Figure 8B. As a result, denser regions of size  $\lambda$  separate from regions depleted of nodes of the same size and form clumps separated from one another by  $r_{\text{clump}}$  over a time  $t_{\text{clump}}$ , where

$$r_{\text{clump}} \approx \lambda, \quad t_{\text{clump}} \approx \lambda / v \approx l / (Q'd) \quad (\text{Regime 1}). \quad 5$$

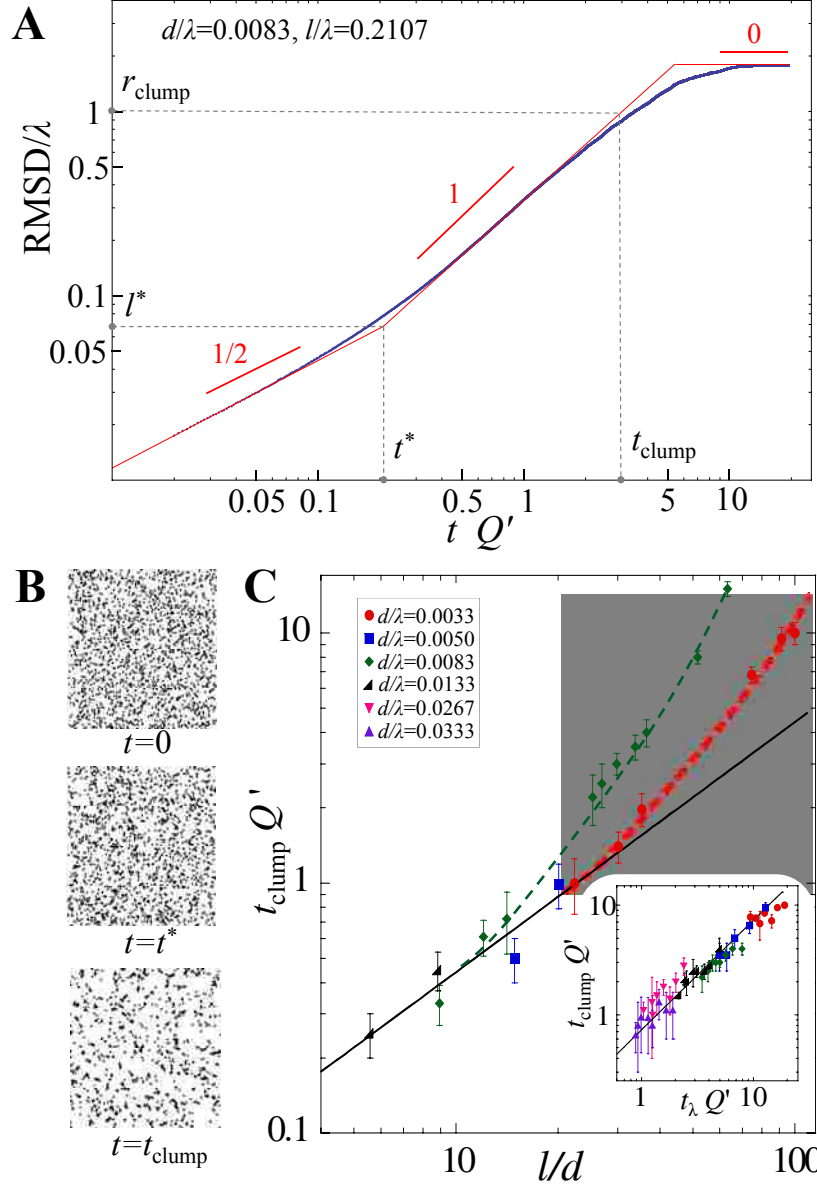


**Figure 8:** Monte Carlo simulations of node aggregation showing kinetics of clump formation in Regime 1 ( $d \ll l$ ). Nodes were placed according to a 2D uniform probability distribution.  $q(r)$  was set to zero for  $r > 3\lambda$ . Periodic boundary conditions were used. (A) RMS displacement vs time. Slope 1/2 regime: active diffusion up to  $t^*$ ; slope 1 regime: clump formation that ends at  $t_{\text{clump}}$ ; slope 0 regime: nodes trapped in isolated clumps. (B) Snapshots of node configurations at different times. (C) Test of  $t_{\text{clump}} Q' \approx l/d$ .  $t_{\text{clump}}$  is the time at which the slope of the linear regime in A decreases by 20%  $\pm$  10%. Solid (black) line:  $t_{\text{clump}} Q' \approx 0.044(6) l/d$  is a linear fit to the subset of the data most asymptotic in R1. Dashed lines are guide-to-the-eye curves indicating approach to common asymptotic regime; deviations occur for  $l$  approaching  $\lambda$ . Inset shows  $t_{\text{clump}} \approx t_\lambda$  in agreement with Equation 5.

These isolated clumps subsequently self-collapse rapidly: as the interaction of nodes with their neighbors that segregate into different clumps is lost, clumps condense into spots over a time much shorter than  $t_{\text{clump}}$ . We tested this scaling expression for  $t_{\text{clump}}$  in Figure 8. We also tested  $r_{\text{clump}} \approx \lambda$  by showing that  $t_{\text{clump}} \approx t_\lambda$  numerically, where  $t_\lambda$  is the time when the root mean square displacement (RMSD) reaches  $\lambda$ .

For R2, active diffusion is strong: nodes travel distances  $L(t)$  larger than the interaction range  $\lambda$ , see Figure 9. This leads to different kinetics. As nodes get displaced over  $L(t) > \lambda$ , the diffusion coefficient remains unchanged from Equation 2. However, nodes experience an increasingly larger transport rate  $v_t$  due to Poisson fluctuations over distances  $L(t)$ . Since 2D diffusion is marginally compact [44], nodes sample their exploration volume uniformly, within logarithmic corrections. Thus, replacing  $\lambda$  by  $L(t)$  in Equation 2:

$$v_t \approx Q' d L(t) / l \tag{6}$$

The distance at which transport by  $v(t)$  dominates diffusion marks the time at which clumps start to form,  $r_{\text{clump}} = v_{t_{\text{clump}}} t_{\text{clump}} = (D t_{\text{clump}})^{1/2}$ . This gives:

$$r_{\text{clump}} \approx \lambda (d/l)^{1/2}, \quad t_{\text{clump}} \approx l / (Q'd). \text{ (Regime 2)} \tag{7}$$

The simulations of Figure 9 verify that, unlike in Figure 8, there is no intermediate linear regime: once transport dominates diffusion at  $t_{\text{clump}}$ , groups of nodes within  $r_{\text{clump}} = L(t_{\text{clump}})$  of one another collapse rapidly into isolated clusters; see Figure 9 B. The scaling of  $t_{\text{clump}}$  in Figure 9C is consistent with Equation 7. The exponent of  $r_{\text{clump}}$  in Figure 9C differs from 1/2, possibly due to a slow crossover from R1 (slope 0), logarithmic terms, or unaccounted many-body correlations that develop over time.

Further numerical tests, deeper in R2, were prohibited by the large number of nodes required ( $>10^7$ ).

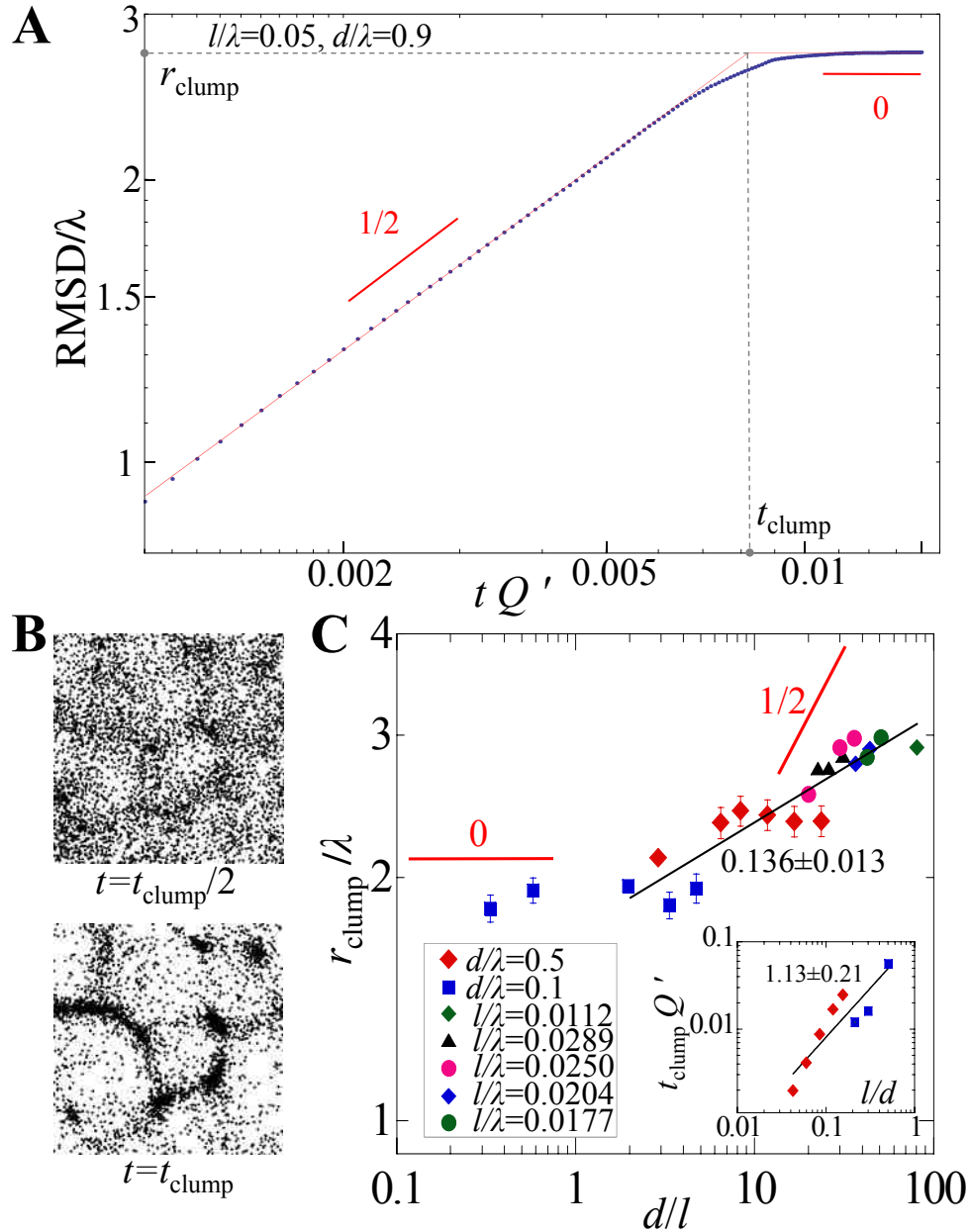


**Figure 9:** Simulations for Regime 2 ( $l \ll d \ll \lambda$ ). (A) RMS displacement vs time. Slope  $1/2$  regime: active diffusion; slope  $0$  regime: nodes trapped in clumps. (B) Snapshots of node configurations. (C) Test of Equation 7. Thick (red) lines show predicted slopes in R1, R2; thin (black) lines show fits.  $t_{\text{clump}}$  is time required to reach RMSD plateau (panel A) and  $r_{\text{clump}}$  is corresponding distance.



### 3.2. 2D band of nodes

The results of Section 3.1 describe a bulk system. Consider now a 2D band of nodes of width  $w$ . The following arguments agree with simulations in Figure 10. Because of concentration gradients, nodes at distances of order  $w$  from the middle of the band experience directed transport towards the center with velocity  $v_w \approx \int_{-\pi/2}^{\pi/2} \int_0^\infty d\phi dr d \cos(\phi) q(r) c(r, \phi)$ . This integral is over a radial coordinate system centered at a node,  $c(r, \phi)$  is node concentration, and  $d \cos(\phi)$  is distance traveled towards the center for connections at angle  $\phi$ . The integral is dominated by  $r$  of order the smallest of  $w$  and  $\lambda$ :

$$v_w = \begin{cases} Qadcw, & w \ll \lambda \\ Qadc\lambda^2 / w, & w \gg \lambda \end{cases} \quad 8$$

assuming that the typical gradient across the band is of order  $c/w$ , where  $c$  is concentration in the middle. For narrow bands,  $w \ll \lambda$ , the velocity  $v_w$  defines a time over which boundary nodes travel distance  $w$ :

$$t_{\text{shrink}} \equiv w / v_w = l^2 / (Qad) \quad (w \ll \lambda). \quad 9$$

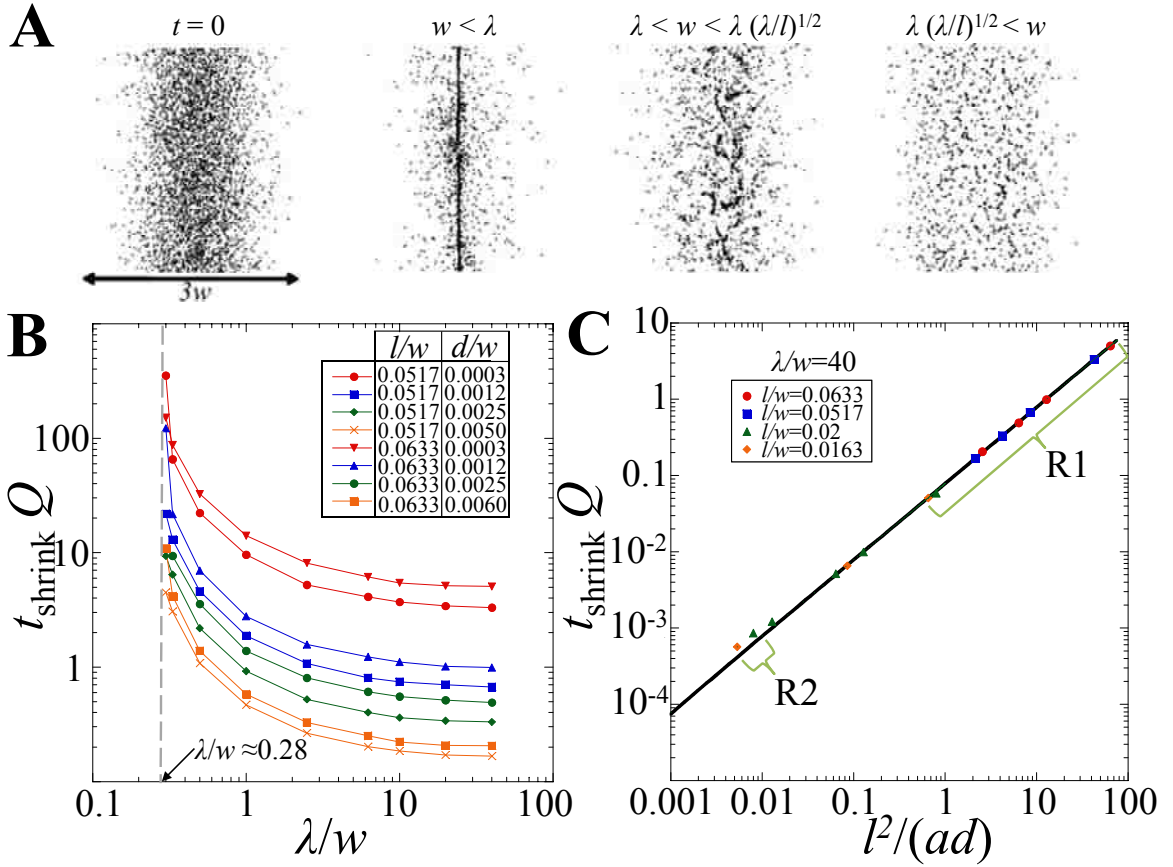


**Figure 10:** Simulations of condensation of a band of nodes (periodic boundary conditions vertically). Nodes were placed according to Gaussian distribution with variance  $w/2$ . (A). Initial distribution (first panel) and snapshots of successful condensation or clump formation for different ( $l/w = 0.0315$ ,  $d/w = 0.0125$ ,  $a/w = 0.25$ ). (B) Condensation time (time required for the standard deviation to decrease by 1/2) vs  $\lambda/w$  using  $a/w = 0.25$ . For  $\lambda/w < 0.28$  the band does not shrink. (C) Test of  $t_{\text{shrink}} \approx l^2/(Qad)$ . Solid (black) line is linear fit to R1 data:  $t_{\text{shrink}} = 0.078(5) l^2/(Qad)$ .

This time is shorter than  $t_{\text{clump}}$ , for both R1 and R2, since  $t_{\text{shrink}}/t_{\text{clump}} \approx l/\lambda \ll 1$ . Thus narrow bands condense (“shrink”) into rings before clumps have sufficient time to form.

Wide bands,  $w \gg \lambda$ , do not condense into rings. In this case,  $t_{\text{shrink}} \approx w^2 l^2/(Qad\lambda^2)$ . There are two subcases: (i) For very wide bands,  $w \gg \lambda(\lambda/l)^{1/2}$  and  $t_{\text{clump}} \ll t_{\text{shrink}}$ . Therefore clumps form before the band condenses. (ii) Bands with  $\lambda \ll w \ll \lambda(\lambda/l)^{1/2}$  split into smaller bands over a time of order  $t_{\text{shrink}}$ . To see this, consider two nodes within

interaction range, i.e., within  $\lambda$  of one another. Because of the density gradient, the difference in their condensation velocities toward the middle is of order  $\Delta v_\lambda \approx Qad\lambda^2\Delta c_\lambda/w$ , where  $\Delta c_\lambda \approx c\lambda/w$ . These nodes lose contact with one another when their relative velocity transports them over distances of order  $\lambda$ . This occurs over time  $t_{\text{split}} = \lambda / \Delta v_\lambda \approx t_{\text{shrink}}$  causing the band to lose internal connectivity as it is about to form a ring, see Figure 10A.

### 3.3. Comparison to experiment

We can apply above results to fission yeast, using parameter values obtained from prior experiments [13, 26]:  $d = 0.45 \mu\text{m}$ ,  $l = 0.77 \mu\text{m}$ ,  $w = 1.8 \mu\text{m}$ ,  $a = 0.1 \mu\text{m}$ ,  $\lambda = 1\mu\text{m}$ , and  $1/Q=0.67 \text{ min}$ . These values are near the R1-R2 boundary. Since  $\lambda/w = 0.56$ , the band is just narrow enough to allow condensation. Simulations using these values indicate  $t_{\text{shrink}} \approx 15 \text{ min}$  (13 min using Equation 9), very close to experiments; see Figure 7. For a 2D bulk of nodes we find  $t_{\text{clump}} = 15 \text{ min}$  with simulations (12 min using Equation 5). We suggest that the small difference in these two times leads to clump formation in *cdc12-112* mutants in Figure 4A: a small change in the polymerization rate of actin, for example, may result in slightly shorter actin filaments causing the cell to shift to the  $\lambda < 0.28 w$  regime of Figure 10C. Since node protein Cdc15p recruits Cdc12p to the nodes, and since the septation initiation network (SIN) pathway promotes proper Cdc15p localization, we suggest that a similar mechanism explains clump formation in Cdc15p and SIN pathway mutants [28]. Image analysis of actin in these cells [26, 28] could test this prediction.

Another prediction of the model is the formation of fragmented linear structures for intermediate values of  $\lambda$ , Figure 10.

Cells may have optimized parameter values. Presumably, the width of the node band is limited by the accuracy with which cells locate their middle [45]. We speculate that yeast establishes filaments long enough ( $\lambda \sim w$ ) to achieve condensation without clumps, but not much longer; the latter would provide little benefit since the condensation time is independent of  $\lambda$ , to leading order. Condensation is accelerated by smaller  $l$  (high node densities); thus, the number of nodes may reflect the balance between speed and cost required to generate nodes. Additionally, the condensation time decreases with increasing node step  $d$ , whose upper limit is  $\sim \lambda/2$ . This could be the reason why  $d/\lambda \approx 0.5$  in cells.

The stochastic model developed in this Chapter was successful in describing the kinetics of node condensation and predicted node condensation times similar to those measured in experiments. However, this model fails to generate long-lived linear actomyosin filamentous structures (meshworks) that were previously illustrated in Figure 4B. Therefore in the next Chapter I will develop a model that describes a mechanism of how long-lived meshworks may form.

## 4. Node condensation into a ring in a model that includes node alignment

In this Chapter I will address a morphological feature of condensing bands of nodes that is not captured by either the SCPR model or the stochastic aggregation model described in the previous Chapter. In images of cells expressing node marker Rlc1p-3GFP (a myosin light chain), linear transient structures are frequently observed, see Figure 11. Such linear structures are not seen in simulations of the SCPR model. These linear structures are even more pronounced during condensation of the broad band of nodes in *cdc25-22* mutant cells after release from arrest, see Figure 11C and D. *cdc25-22* cells grow longer and accumulate more nodes (~100 compared to ~65 in wild-type) in a wider band of about ~3.2  $\mu\text{m}$  compared to wild-type cells that is only 1.8  $\mu\text{m}$  [33]. The linear structures often condense to meshwork-like structures rather than contractile rings [17]. In some *cdc25-22* cells two partially-merged parallel bundles form structures that appear as two rings.

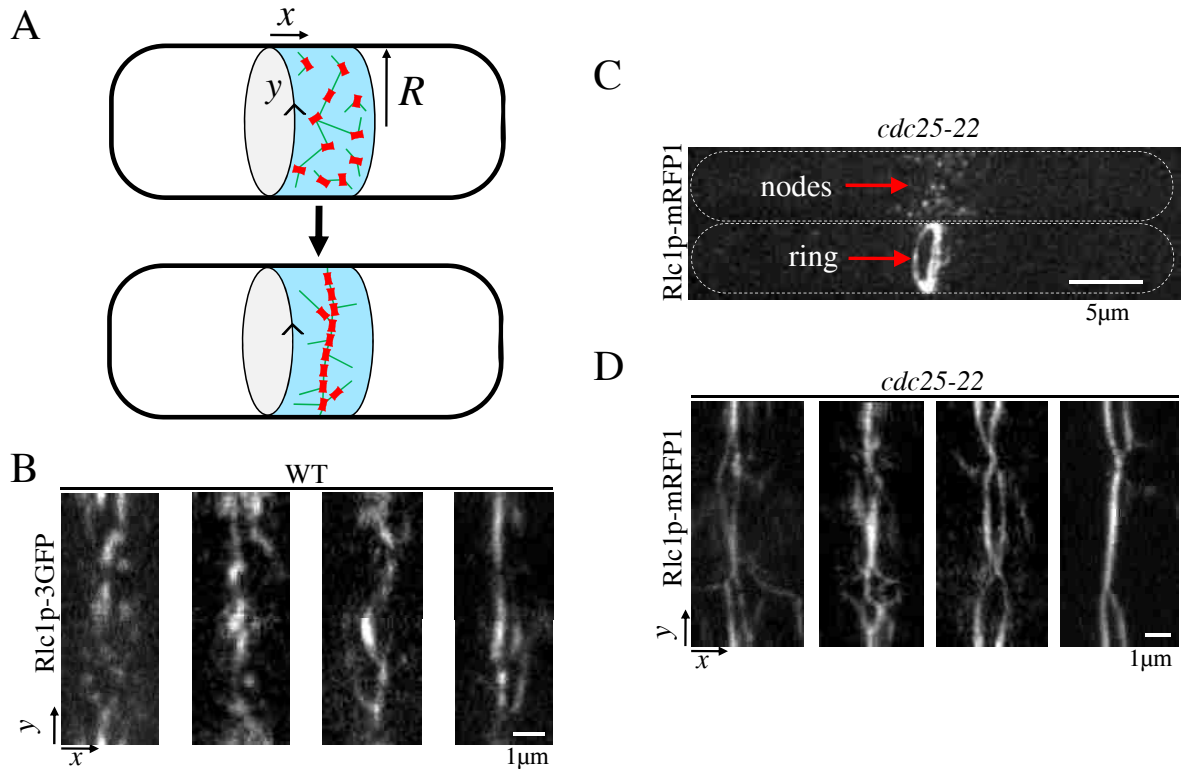


**Figure 11:** (A) Cartoon of ring formation with the  $x$ -axis parallel to the long axis of the cell;  $y$  measures arc length along the cell circumference. In the SCPR model, nodes condense into rings through connections established by actin filaments (green). (B) Images showing examples of wild-type cells expressing Rlc1p-3GFP during the process of ring formation [29]. Transient linear structures are seen, in addition to isolated nodes. The images are ‘radial projections’ obtained by projecting the intensity of a hollow tube aligned along the axis of the cell onto a surface of radius  $R = 1.73 \mu\text{m}$  representing the cell surface. In this projection the  $x$  and  $y$  directions are those illustrated in panel A. The projection was obtained using 26  $z$ -slices, separated by  $0.2 \mu\text{m}$ . (C)  $z$ -projections of *cdc25-22* cells expressing Rlc1p-mRFP1 [13]. *cdc25-22* cells grow longer and accumulate more nodes in a wider band compared to wild-type cells during arrest from entering mitosis. After release into mitosis, nodes condense to contractile rings [17]. Top: cell with nodes; bottom: cell with ring. (D) Radial projection of four representative *cdc25-22* cells in the process of ring assembly (obtained by 24  $z$ -slices separated by  $0.3 \mu\text{m}$ ). Long linear structures are more evident compared to wild-type cells. These linear elements extend along many directions, forming meshworks. Near the end of ring assembly, parallel bundles resembling ‘two rings’ appear. In some cells, those bundles that form a ring around the cell constrict independently of the other parts of the bundle structure.

Each node contains about 55 myosin-II molecules which may assemble into bipolar minifilaments (though no evidence for minifilament formation in nodes exists yet) [17, 18, 24]. It is conceivable that transient binding of myosin heads to actin filaments that connect the nodes helps align the nodes into linear structures. Actin cross-linker proteins fimbrin Fim1p and  $\alpha$ -actinin Ain1p are also involved in node alignment [46, 47], see Chapters 5 and 6. Fimbrin can bundle actin filaments into tight bundles while  $\alpha$ -actinin cross-links actin filaments more loosely. They both play a role during fission yeast contractile ring formation and deletions of their genes are synthetically lethal [46, 47]. Another candidate molecule for node alignment is IQGAP Rng2p. This node component protein can bundle actin filaments [48]. Finally, node scaffold protein Mid1p could also play a role through oligomerization [49].

We assume that each node has an internal polarization represented by the orientation of a line element (see Figure 12). Nodes are assumed to be bipolar, i.e. we do not distinguish between the two poles of the node. While a monopolar structure cannot be excluded, a bipolar orientation is a reasonable starting assumption. Recent measurements in [24] indicated that the tails of Myo2p in the nodes are oriented at  $71^\circ$  with respect to the plasma membrane. Since myosin tails generally associate with one another, this would be consistent with an internal organization with a preferred axis. It remains unknown however if Myo2p assembles into bipolar minifilaments in nodes as in other sarcomeric-like structures.

In the following Section 4.1 a simple model for the formation of linear node structures is presented. We keep the basic processes of SCPR but we add a local alignment mechanism. In this new model, nodes have a preferred axis of polarization.

They align along the same direction when in close proximity (see Figure 12). This node alignment process is a coarse-grained representation of all the factors that contribute to the formation of linear node structures. We examine the results of this combination of long-range transport of nodes through search and capture with local alignment and find the range of parameters for which this mechanism promotes ring stability. We further describe how the model can generate condensing broad bands that have morphological features similar to those seen in experiments.

#### **4.1. Model of SCPR with local node alignment**

In the simulations, nodes are constrained to move on a 2D plane that represents the cell membrane. The  $x$ -axis is the direction along the long axis of the cell and the  $y$  - axis is along the cell circumference, see Figure 11. Periodic boundary conditions were applied at  $y = 2\pi R$ , where  $R = 1.73 \mu\text{m}$  [18]. The nodes were initially distributed along the  $x$  - axis according to a Gaussian distribution of standard deviation  $0.9 \mu\text{m}$  equal to the half-width of the node distribution determined experimentally [13]. Nodes were placed according to a uniform probability distribution along the  $y$  - axis. The initial node orientation was random.



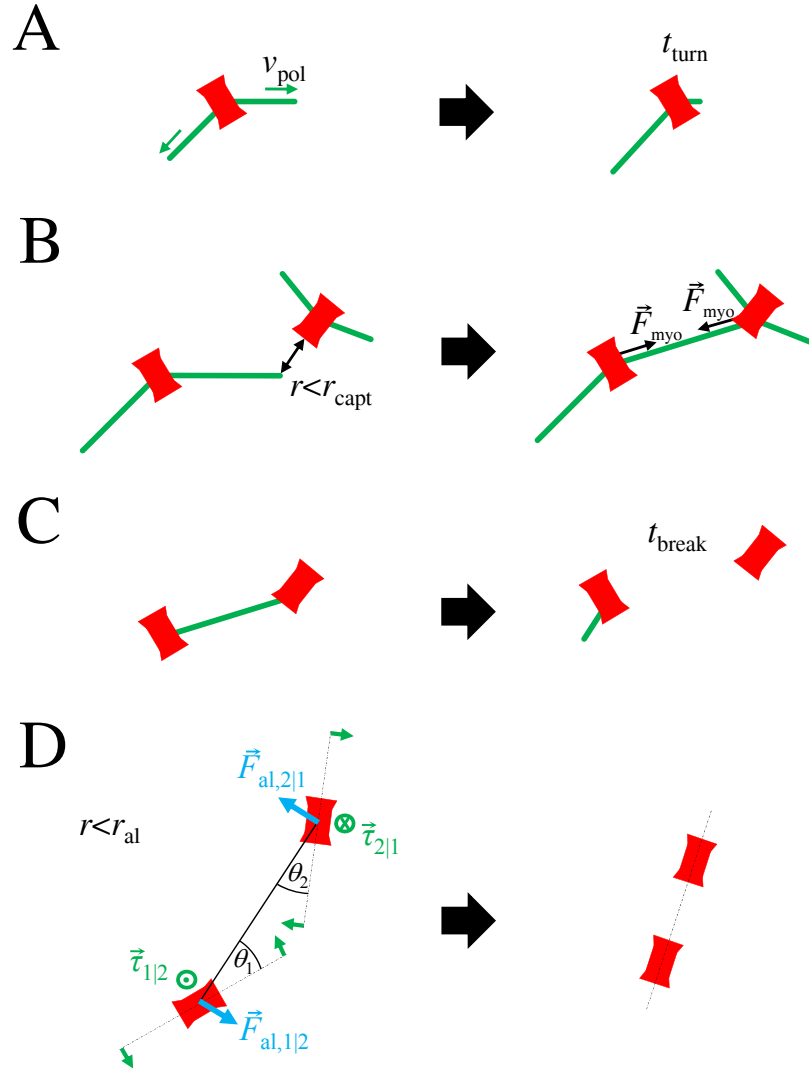


**Figure 12:** The search, capture, pull, and release model with the addition of local node alignment. Nodes are drawn as bars to illustrate their assumed polarization. (A) Search: two actin filaments grow out of each node along randomly chosen directions with rate  $v_{\text{pol}}$ . The average lifetime of actin filaments is  $t_{\text{turn}}$ . Filaments start to grow along a new direction after breakage. (B) Capture and pull: when an actin filament tip approaches another node, a connection is established. Connected nodes move toward one another by pulling force  $F_{\text{myo}}$ . (C) Release: the average lifetime of a connection is  $t_{\text{break}}$ . After breakage, filaments start growing along a random direction as in panel A. (D) Local node alignment: nodes within  $r_{\text{al}}$  of one another experience a torque  $\tau$  that rotates them to point toward one another. Additionally, the force  $F_{\text{al}}$  acts on node centers, perpendicularly to the line that joins two nodes. We note that even though nodes are drawn as elongated objects, the shape of the nodes is not taken into account explicitly: for example, we did not consider anisotropic friction coefficients.

We used the original SCPR mechanism [13] to simulate how nodes make random connections to pull one another over long distances. Below, I first introduce the original SCPR mechanisms and then I introduce the new local alignment process.

Search (Figure 12A): We assume that each node polymerizes two actin filaments (represented as growing lines) along random directions on the 2D plane, as expected from the presence of two formin Cdc12p dimers per node [18, 24, 26]. Formins polymerize actin monomers while remaining attached to the barbed end [32, 33]. As in Chapter 2, we assume that the barbed end of the actin filament resides on the node while the pointed end extends out of the node as node-associated Cdc12p elongates the filament by polymerization. The filament length increases with constant speed  $v_{\text{pol}} = 0.2 \mu\text{m s}^{-1}$  [13]. During elongation, the orientation of actin filaments remains fixed. More recent evidence suggests that Cdc12p is very dynamic in the nodes with a half-time of 30 s and may be distributed to only 50% of the myosin nodes [26]. Here, we assume that all nodes are able to nucleate two actin filaments to compare with previous simulations. Ring assembly by SCPR is not sensitive to the fraction of nodes nucleating actin, as long as this fraction exceeds 50% [13].

Actin filament turnover through cofilin severing is represented by filament disappearance and regrowth along a new direction out of the node. The filament lifetime was  $t_{\text{turn}} = 20 \text{ s}$  [13]. Turnover is simulated by filament disappearance with probability  $dt/t_{\text{turn}}$  per time step  $dt$ .

Capture and pull (Figure 12B): When the pointed end of a polymerizing filament comes within distance  $r < r_{\text{capt}} = 0.2 \mu\text{m}$  of another node, we assume that a connection is established and pulling forces are exerted between nodes. This simulates the process of

myosin heads in the target node binding to the growing actin filament and exerting a pulling force toward the barbed end at the nucleating node. The magnitude of the force is  $F_{\text{myo}} = 4 \text{ pN}$ , acting on each node in the direction of the other node. This force contributes to the total force shown in equation below. Once a filament is captured, filament elongation is terminated [13]. Here,  $r_{\text{capt}}$  is two times larger than in [13], accounting for actin filament pointed end deflection due to thermal fluctuations (about  $0.15 \text{ }\mu\text{m}$  for a filament of length  $1 \text{ }\mu\text{m}$  and persistence length  $10 \text{ }\mu\text{m}$  [50-52]). We do not allow for capture when nodes are within  $0.4 \text{ }\mu\text{m}$  of one another (the distance at which the alignment mechanism is assumed to take over, see below). The combination of these two changes does not lead to significant modifications of the SCPR kinetics, see figure S15 in [13].

Release (Figure 12C): We assume that connected filaments turn over, similarly to unconnected filaments, with lifetime  $t_{\text{break}} = t_{\text{turn}} = 20 \text{ s}$ . In the simulations, each connection breaks with probability  $dt / t_{\text{break}}$  per time step  $dt$ . Upon filament breakage, a new filament starts to grow along a new, randomly chosen direction.

We added additional forces to the SCPR model to simulate a mechanism of local node alignment, see Figure 12D. These additional interactions occur when the distance between the centers of a pair of nodes is shorter than an ‘aligning distance’,  $r_{\text{al}}$ . We choose  $r_{\text{al}} = 0.4 \text{ }\mu\text{m}$  to be a distance of similar magnitude to the physical size of the nodes. This distance is much less than the typical length of an actin filament in the simulations,  $t_{\text{turn}}v_{\text{pol}} \approx 4 \text{ }\mu\text{m}$ . In this model, the long-range interaction responsible for node condensation is due to the SCPR mechanism, while the short-range interaction responsible for linear structure formation is due to the local alignment mechanism. The

alignment mechanism consists of two processes: (i) rotation of node polarization around the center of the node, described by a torque  $\tau$ , and (ii) node movement around a neighboring node described by an aligning force  $F_{al}$ .

Rotation around the node center (Figure 12D): We assume that nodes that are within  $r_{al}$  of one another rotate their polarization in such a way that their axis of polarization points toward the center of their neighbor. Consider a pair of nodes labeled by  $i = 1, 2$ . We define  $\theta_i$  to be the smaller angles measured from the line that joins the centers of nodes 1, 2 to the polarization axis of node  $i$ . The sign of the angle is positive in the counterclockwise direction. To satisfy torque balance we assume a torque of equal magnitude but opposite direction acting on node 2. The equation that describes the magnitude of the torque around the center of node 1 is:

$$\tau_{1|2} = \tau_0 (\sin(\theta_1) e^{-\theta_1/\bar{\theta}}) / C_{\max} - \tau_0 (\sin(\theta_2) e^{-\theta_2/\bar{\theta}}) / C_{\max} . \quad 10$$

Here,  $\tau_0$  is a constant prefactor that sets the amplitude of the torque and  $C_{\max} = 0.12625$  is a normalization constant equal to the maximum value of the function  $\sin(\theta) e^{-\theta/\bar{\theta}}$ . We chose a simple sinusoidal functional dependence on angles, similarly to other studies[1]. An upper cutoff at an angle  $\bar{\theta} = 20^\circ$  represents the decrease in the magnitude of the torque for very large angles [53].

Movement around neighbors: We introduced aligning forces that act on the centers of nodes, perpendicularly to the line that joins their centers (see nodes labeled  $i = 1, 2$  in Figure 12D). We postulate a force on node  $i$  that acts along the direction that decreases the magnitude of angle  $\theta_i$ . The unit vector along this direction is  $\bar{e}_\perp^i$ . To satisfy

force balance, we assume a force of equal magnitude but of opposite direction acting on the neighbor. We used the following expression for the force on node 1 due to node 2:

$$\mathbf{F}_{al,1|2} = f_{al} (\sin(|\theta_1|) e^{-|\theta_1|/\bar{\theta}} / C_{\max}) \hat{e}_{\perp}^1 - f_{al} (\sin(|\theta_2|) e^{-|\theta_2|/\bar{\theta}} / C_{\max}) \hat{e}_{\perp}^2. \quad 11$$

Here,  $f_{al}$  determines the magnitude of the aligning force. The angular dependence is chosen to be the same as in equation for torque. This expression satisfies force balance:

$$\mathbf{F}_{al,1|2} = -\mathbf{F}_{al,2|1}.$$

Short-range repulsion: In addition to the above aligning forces, we introduce a short-range repulsion force to prevent nodes from overlapping with one another, as in the SCPR model [13]. This is achieved by a repulsive radial force of magnitude 80 pN when node centers are within  $r = 2 r_{\text{node}} = 0.2 \mu\text{m}$  of one another, where  $r_{\text{node}}$  is the node radius.

Node movement: The rate of node rotation is proportional to the total torque, which is a superposition of all torques acting on a node:

$$\dot{\phi}_i = -\tau_{\text{tot},i} / \zeta_{\text{rot}}, \quad \tau_{\text{tot},i} = \sum_{j, j \neq i} \tau_{ij}. \quad 12$$

Here,  $\phi$  is the angle of node  $I$  in the node coordinate system and  $\zeta_{\text{rot}}$  is the rotational friction coefficient.

$$\mathbf{F}_{\text{tot},i} = \sum_{j, j \neq i} (\mathbf{F}_{\text{myo},i|j} + \mathbf{F}_{\text{al},i|j} + \mathbf{F}_{\text{rep},i|j}), \quad 13$$

where  $\mathbf{F}_{\text{myo},i|j}$  is the myosin pulling force due to node  $j$  (being nonzero only during a connection).  $\mathbf{F}_{\text{rep}}$  is the short-range repulsion force due to node  $j$ . The resulting node velocity is

$$\mathbf{v}_i = \mathbf{F}_{\text{tot},i} / \zeta_{\text{trans}}, \quad 14$$

where  $\zeta_{\text{trans}} = 400 \text{ pN s } \mu\text{m}^{-1}$  is the node translational friction coefficient [13].

Integration: Using the above equations, the orientations and positions of nodes were evolved with an integration step  $dt = 0.1s$ . We checked that this value was sufficiently small. The friction coefficients were assumed independent of node orientation. In our model, the alignment depends on two parameters. The magnitude of the rotation rate depends on  $\tau_0/\zeta_{rot}$ , see Equations 10 and 12. The magnitude of the aligning force depends on  $f_{al}$ , see equation (2). This is similar to [1], where the aligning of two polar filaments was described by three parameters,  $\alpha$ ,  $\beta$  and  $\gamma$ . Here we have just two parameters because we assume that the nodes are bipolar. As the same molecular mechanisms contribute to torque and movement around neighbors, these two parameters are related to one another. However, since the molecular origin of the alignment mechanism is still unclear, we will explore the effect of the numerical values of the two parameters by treating them as independent variables.

## 4.2. Simulation results

Dependence of ring formation on alignment parameter values: We studied the effect of the proposed local node alignment mechanism using numerical simulations. The process of ring formation was observed, starting from a broad initial distribution of nodes (see Figure 13A). We quantified the degree of success of ring assembly using three observables: largest gap, band width, and porosity (see Figure 13B)[13]. The largest gap is defined as the length of the largest circumferential gap without nodes. The band width is twice the standard deviation of the distribution of the  $x$  coordinates of nodes. Porosity is defined as the ratio of the sum of the lengths of all circumferential gaps (i.e. gaps

without nodes along the  $y$  direction as in the case of the largest gap) to the cell circumference  $2\pi R$ . Porosity values close to zero indicate rings with very few holes. Gap distances are measured from node boundaries (nodes are assumed to have a radius  $r = 0.1 \mu\text{m}$ )

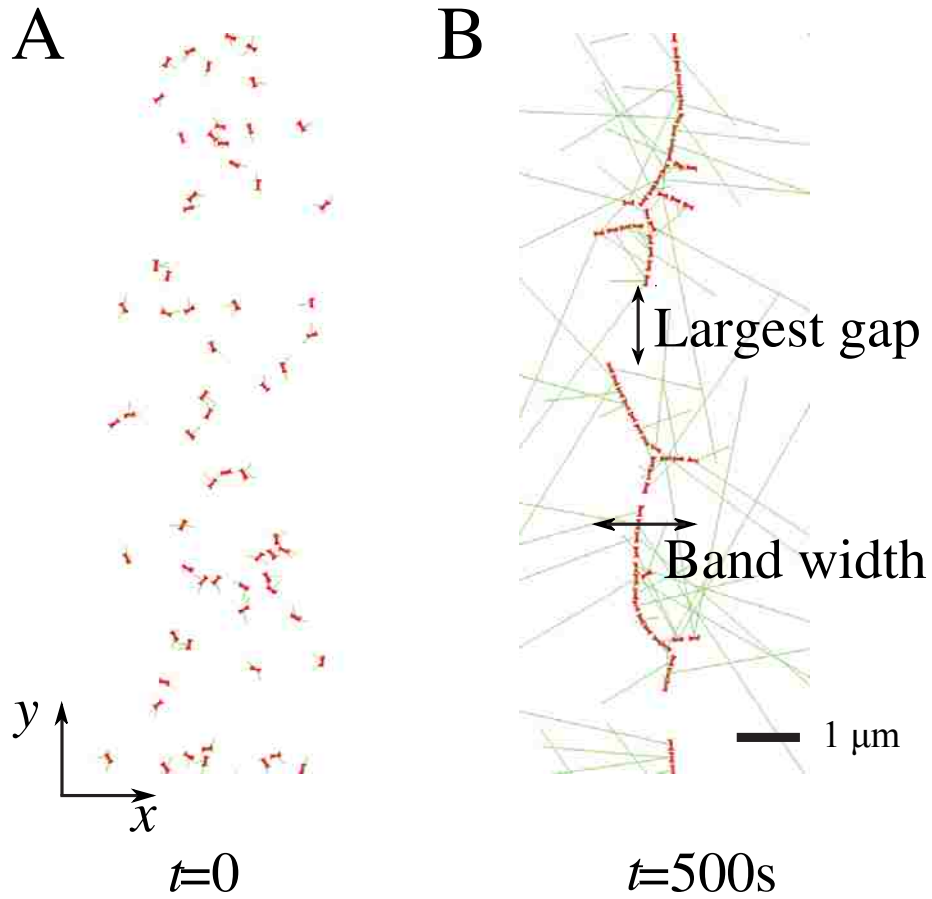


**Figure 13:** Snapshots of simulations showing the initial node distribution in (A) and nodes condensed into a ring structure in (B). The  $x$ -axis is parallel to the long axis of the cell; the  $y$ -axis is arc length along the cell circumference. Nodes are initially distributed according to a Gaussian distribution of standard deviation  $0.9 \mu\text{m}$  along the  $x$ -axis and according to a uniform distribution along the  $y$ -axis [13]. Panel (B) shows largest gap and band width.

We examined the effect of local node alignment by measuring porosity, largest gap, and band width as a function of the two parameters introduced to the SCPR model:

$f_{\text{al}}$  and  $\zeta_{\text{rot}}/\tau_0$ . These two parameters measure the strength of the aligning force and torque, respectively: large  $f_{\text{al}}$  values indicate a large aligning force while large  $\zeta_{\text{rot}}/\tau_0$  values indicate slow rotation of the polarization axis around the node center. All other parameters were kept fixed to the values of the SCPR model, as described in 4.1. Figure 14 shows the results of simulations in which the aligning force and torque were varied. The values in the graphs are averages of 1000 simulations for each pair of parameter values. The values in Figure 14 were calculated 500 s after the start of the simulations. This is approximately equal to the time required for the ring to assemble from a band of nodes [13].

The results of Figure 14 show that the proposed aligning mechanism can generate rings that are improved compared to pure SCPR, depending on the parameter values. In the plots, the line  $f_{\text{al}} = 0$  pN corresponds to SCPR (since in this case there is no aligning, irrespective of the value of  $\zeta_{\text{rot}}/\tau_0$ ). We found that porosity decreases with increasing aligning force  $f_{\text{al}}$ . Forces of a few pN decrease the porosity by an amount that depends weakly on the value of the rotation time  $\zeta_{\text{rot}}/\tau_0$ . This indicates that alignment promotes the formation of more complete rings.

The largest gap in Figure 14 also decreases with increasing aligning force, but only when the rotation time is sufficiently small (smaller than  $\sim 250$  s  $\text{rad}^{-1}$ ). When nodes rotate very slowly, alignment occurs along the random directions in which the nodes happened to point initially, leading to few but large gaps. The effect of the aligning mechanism on band width is shown in figure Figure 14C. This figure shows that an increase in the aligning force beyond 10–15 pN generates wide rings. This effect is more pronounced at slow node rotation rates (large  $\zeta_{\text{rot}}/\tau_0$ ). The reason is that, similarly to panel



B, very large aligning forces initiate ring segments that grow along incorrect directions determined by the random initial node orientation and spatial distribution. In Figure 14D we draw the region of parameter space in which the alignment generates viable rings (i.e. rings with properties consistent with experimental observations), using the following criteria: porosity  $< 0.33$  (more than  $2/3$  of the circumference is populated by nodes), largest gap  $< 1.4 \mu\text{m}$  (less than  $\approx 10\%$  of circumference length), and band width  $< 0.9 \mu\text{m}$  (one half of initial width). The boundaries corresponding to these criteria are indicated by the dashed lines in figures Figure 14A–C. Parameters in the indicated range in figure Figure 14D produce stable rings.

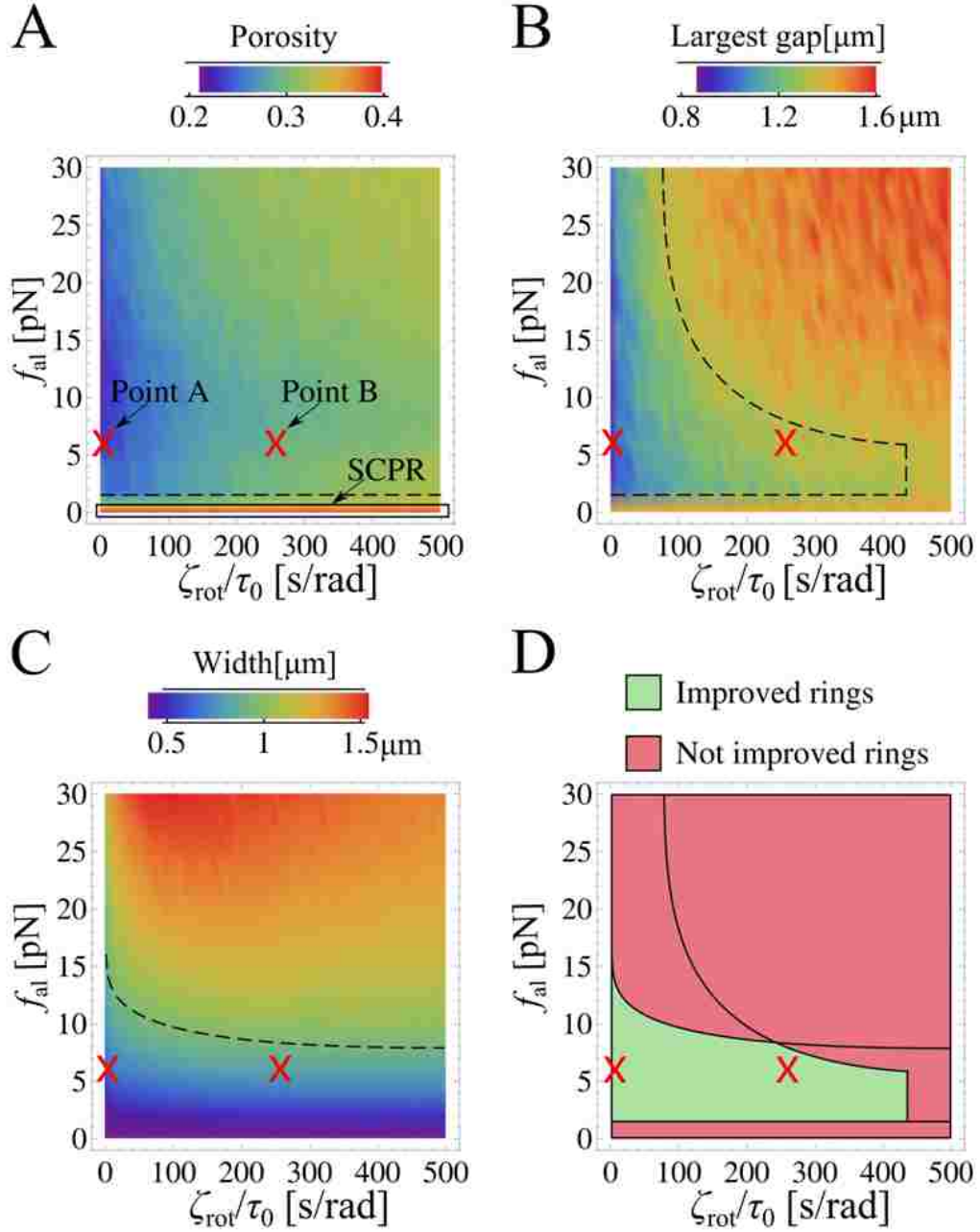


**Figure 14:** Results of Monte Carlo simulations of a model with local node alignment. (A)–(C) Average porosity, largest gap, and band width at 500 s, as a function of the parameter  $\zeta_{\text{rot}}/\tau_0$  (which measures the resistance to rotation of the polarization axis) and the aligning force  $f_{\text{al}}$ .  $\zeta_{\text{rot}}/\tau_0$  was varied in steps of 10 s rad<sup>-1</sup> and  $f_{\text{al}}$  in steps of 2 pN. The results for each pair of parameter values are averages of 1000 simulations. The case  $f_{\text{al}} = 0$  pN reduces to the pure SCPR model (no local node alignment). Dashed lines indicate boundaries of regions of observable quantities consistent with the criteria for viable ring formation of the main text. (D) Plot showing the overlap of regions in parameter space with porosity, largest gap and band width that meet the criteria for viable ring formation of the main text.

*Specific examples:* To further quantify and visualize ring morphologies in the region of parameter space corresponding to viable rings, we examined the two points marked A and B in Figure 14. These two points have the same aligning force  $f_{al} = 6$  pN but different rotation rates to cover the two limits of high and low  $\zeta_{rot}/\tau_0$ , respectively. This aligning force is nearly optimal: it is large enough to result in improved ring formation, small enough to be realistic, and larger values do not result in significant improvements.

Figure 15 shows statistics of 1000 simulations and characteristic ring profiles for point A and for the pure SCPR model. The graphs in Figure 15A show the improved porosity and largest gap distributions with respect to SCPR. The final-width distribution is not changed significantly with respect to SCPR. Note the high peak ( $\approx 23\%$  of events) at zero largest gap: these are rings that completely span the cell circumference, see the snapshots in Figure 15B. Thus, for point A, the aligning mechanism helps in making cohesive rings and in distributing nodes evenly. In comparison with the snapshots obtained for original SCPR, we see that the rings obtained with the additional local node alignment mechanism are more stable and have less clump formation. Therefore, the aligning mechanism improves ring stabilities and ring morphologies.

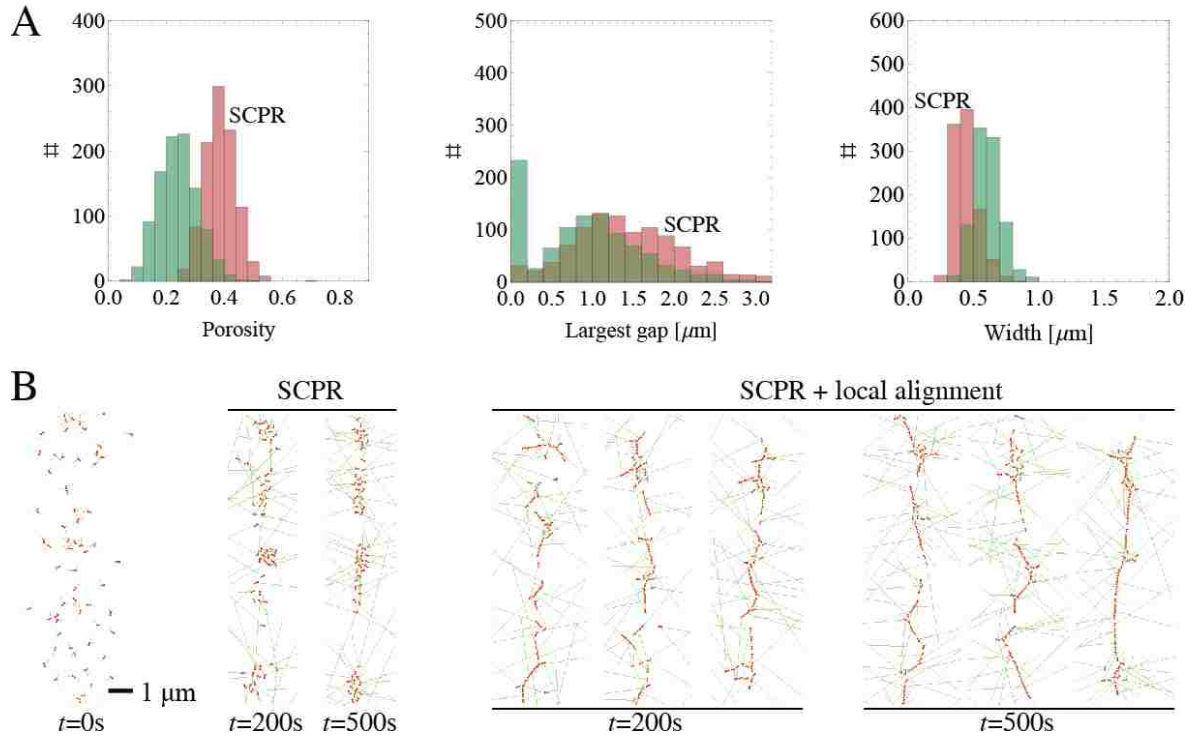


**Figure 15:** Statistics and snapshots of simulations using parameters corresponding to point A in Figure 14 ( $f_{\text{al}} = 6 \text{ pN}$ ,  $\zeta_{\text{rot}}/\tau_0 = 1 \text{ s rad}^{-1}$ ). (A) Distributions of porosity, largest gap and band width for point A (green) and SCPR (red) at 500 s (1000 simulations). The peak at largest gap = 0  $\mu\text{m}$  corresponds to rings that fully span the cell circumference. (B) Snapshots of rings at 200 s and 500 s for pure SCPR and SCPR with local node alignment. In the latter case, rings with no vertical gaps form frequently.

Figure 16 shows the same statistics as Figure 15 but for point B of Figure 14. The overall behavior is similar, but the decrease in porosity and largest gap is less compared with point A. The width of the condensed band is larger. By being unable to rotate fast, nodes align along linear structures that extend in directions different from the ring axis. This results in larger gaps and widths.

An interesting feature of Figure 15B and Figure 16B is the appearance of linear node assemblies during the condensation process (see images of simulations at 200 s).

These shapes are similar to the linear structures observed during the late stages of the condensation process in wild-type cells in Figure 11C.

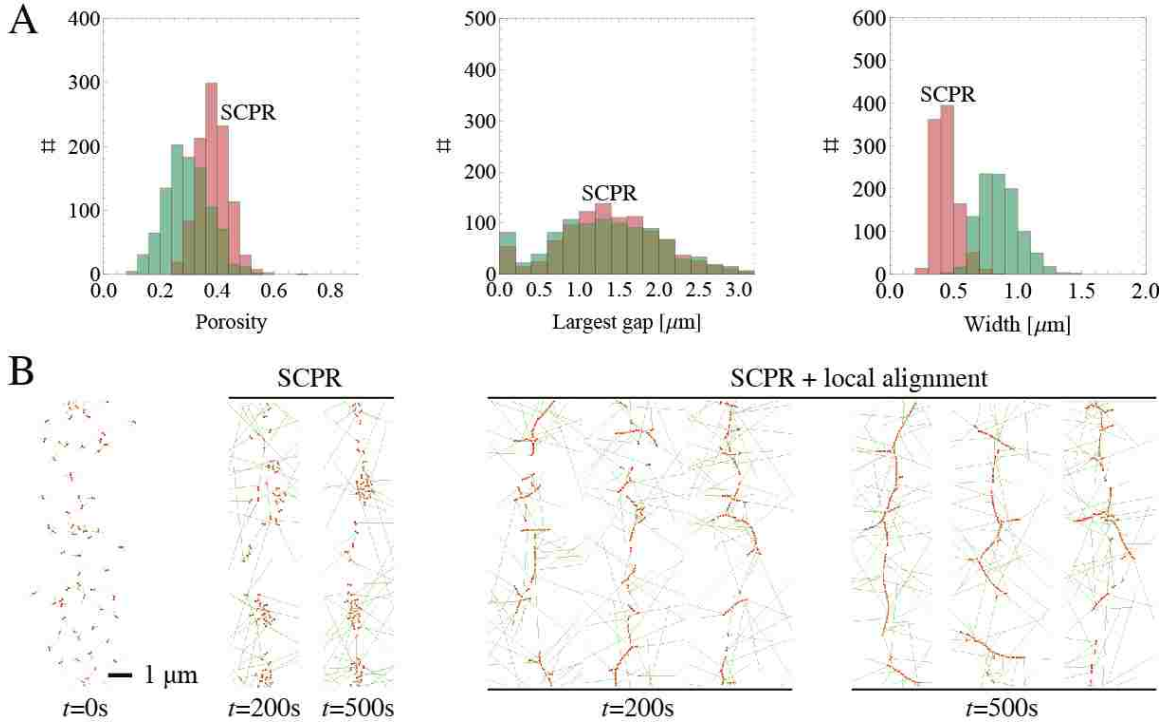


**Figure 16:** Same as Figure 15 but for point B of Figure 14 ( $f_{\text{al}} = 6 \text{ pN}$ ,  $\zeta_{\text{rot}}/\tau_0 = 250 \text{ s rad}^{-1}$ ). Because of node resistance to rotation, side branches and gaps form during ring assembly.

Meshwork structures in simulations of *cdc25-22* cells: The simulations of previous section illustrate the process of local alignment of nodes that come together over long distances through random search and capture. For wild-type cells, this aligning process aids in ring formation and generates transient linear structures. While linear parallel structures are less pronounced in wild-type (WT) cells, they are the typical case in *cdc25-22* cells released from arrest (see Figure 11E). We wanted to test whether our model can reproduce such structures when choosing parameter values that simulate the conditions of *cdc25-22* cells. We performed simulations using alignment parameters

corresponding to those of points A and B in Figure 14. We distributed the nodes in a band of standard deviation  $\sigma = 1.6 \mu\text{m}$ , as observed in those cells [13]. *cdc25-22* cells have  $\approx 100$  cortical nodes. In the simulations, we varied the number of nodes in the range 100–200, and we also varied the aligning distance  $r_{\text{al}}$  in the range 0.4–0.6  $\mu\text{m}$ , since for larger number of nodes and larger  $r_{\text{al}}$  we could see structures very similar to the ones in Figure 11E. We left the number of filaments growing out of the nodes as two, even though in these cells the number of formin dimers per node can be larger than in WT cells (the results described below do not change much by increasing the number of filaments growing out of nodes).

In Figure 17 we show examples of simulation snapshots for *cdc25-22* cells at different times and for different parameter values (point A with  $r_{\text{al}} = 0.4 \mu\text{m}$  and point B with  $r_{\text{al}} = 0.6 \mu\text{m}$ ). In both panels A and B, bundled structures form during condensation, but the extent of large-scale meshwork formation varies. In panel A, because of the wider initial band, the aligning process organizes the nodes into linear elements, before the nodes have enough time to come together into a narrow ring. This phenomenon is similar to the process of clump formation seen in simulations of very wide bands [26]. In panel B, which is a simulation with a higher rotational friction coefficient and a larger aligning distance, the linear elements that form during condensation assemble into a large-scale meshwork structure. Interestingly, as we increase the number of nodes to approach 200, linear structures reminiscent of two parallel rings are noticeable. These structures have a similar morphology to the experimental images of *cdc25-22* cells in Figure 11E. This indicates that, despite its simplicity, the model can capture the important features of ring

assembly, namely the robust ring formation in wild-type cells and the development of meshwork structures in *cdc25-22* cells.

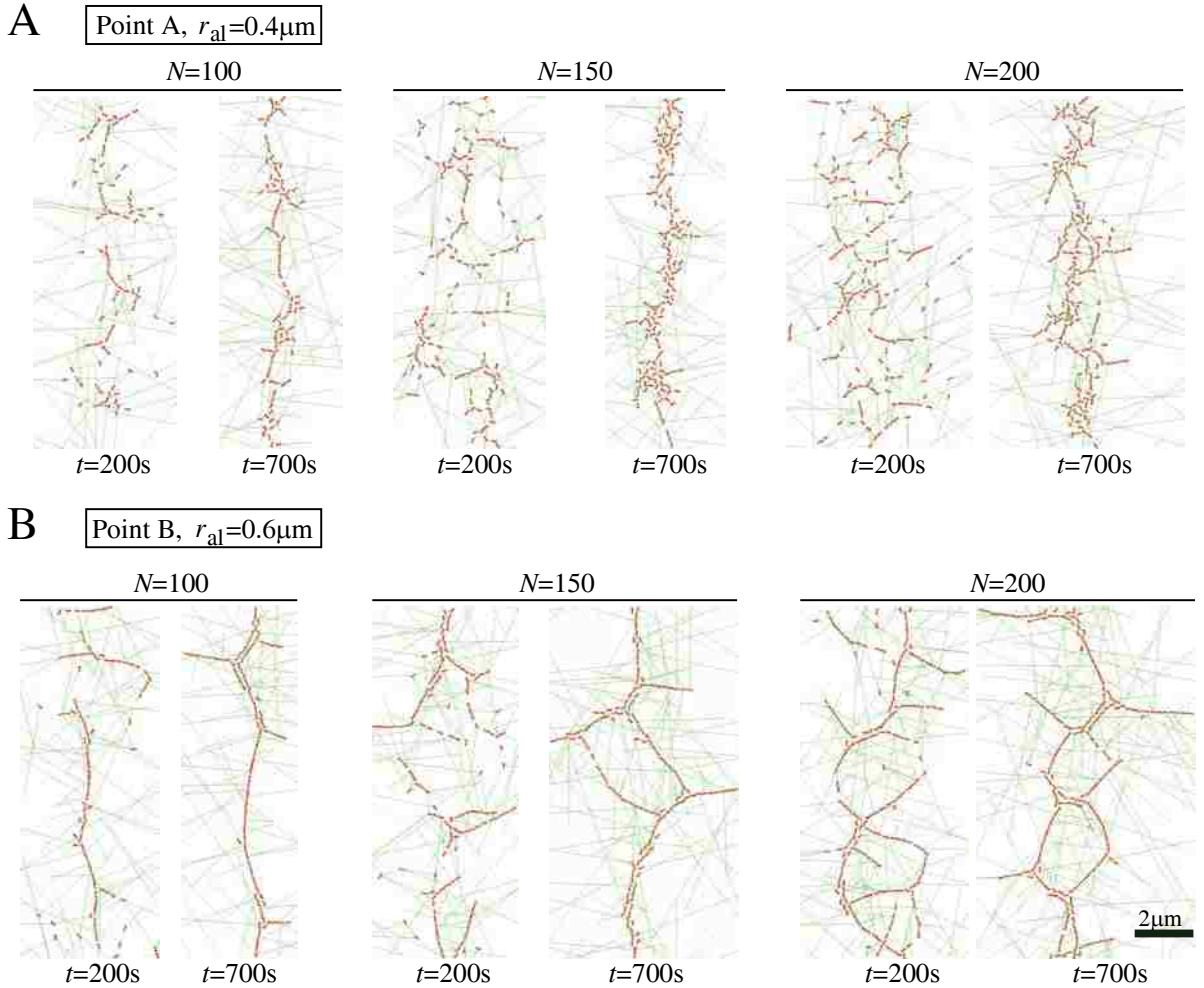


**Figure 17:** Snapshots of simulations for *cdc25-22* cells showing the formation of meshwork structures. (A) Snapshots of rings at different times using the same aligning parameters as point A of Figure 14 ( $f_{al} = 6 \text{ pN}$ ,  $\zeta_{rot}/\tau_0 = 1 \text{ s rad}^{-1}$ ) with  $r_{al} = 0.4 \mu\text{m}$ . Cases with different numbers of nodes are shown ( $N = 100, 150, 200$ ). (B) Snapshots of rings at different times with the same aligning parameters as for point B of Figure 14 ( $f_{al} = 6 \text{ pN}$ ,  $\zeta_{rot}/\tau_0 = 250 \text{ s rad}^{-1}$ ) with  $r_{al} = 0.6 \mu\text{m}$ .

*Local alignment does not prevent clump instabilities:* It is shown earlier in Figure 5 that the SCPR mechanism generates isolated clumps of nodes instead of rings when the parameter values are different from those observed experimentally [13]. Since the nodes

pull one another, inhomogeneities in concentrations are amplified and the nodes tend to segregate into isolated clusters. When the time required for the band to condense to a ring is longer than the time required for clump formation within the interior of the band, condensation fails and isolated aggregates form [25]. The main criterion for successful ring formation is the relationship between the average length of actin filaments,  $\lambda = v_{\text{pol}} t_{\text{turn}}$ , and the initial band width,  $w$ : successful ring formation requires  $\lambda > Aw$ , where  $A$  is a number of order unity [25], see Section 3.2 and Figure 10. We have so far used parameter values corresponding to successful ring formation through pure SCPR (outside of the clump-formation region of parameter space). We wanted to test whether the aligning mechanism introduced in this Chapter prevents clump-formation instabilities in systems that would otherwise form clumps with pure SCPR. In Figure 18 we varied  $\lambda$  and  $w$  by changing the parameters  $t_{\text{turn}}$  and initial width, respectively. The aligning parameters were those of points A and B of Figure 14. We found that the band fails to condense into rings for approximately the same  $\lambda$  and  $w$  values as for pure SCPR. Thus, local alignment did not assist ring assembly in systems that form clumps. This is expected: clumps form by connections and transport of nodes over long distances (of the order of the average filament length). Node alignment over small distances influences the structures of the clump aggregates, but its effect is short-ranged. We note that, depending on the node density, the number of nodes within a clump formed by SCPR could be large. By lining up, these nodes may be able to reach out to a neighboring clump structure. A meshwork with holes of size of order  $\lambda$  or larger may form in this manner. Here we do not consider the slow dynamics of such meshworks.



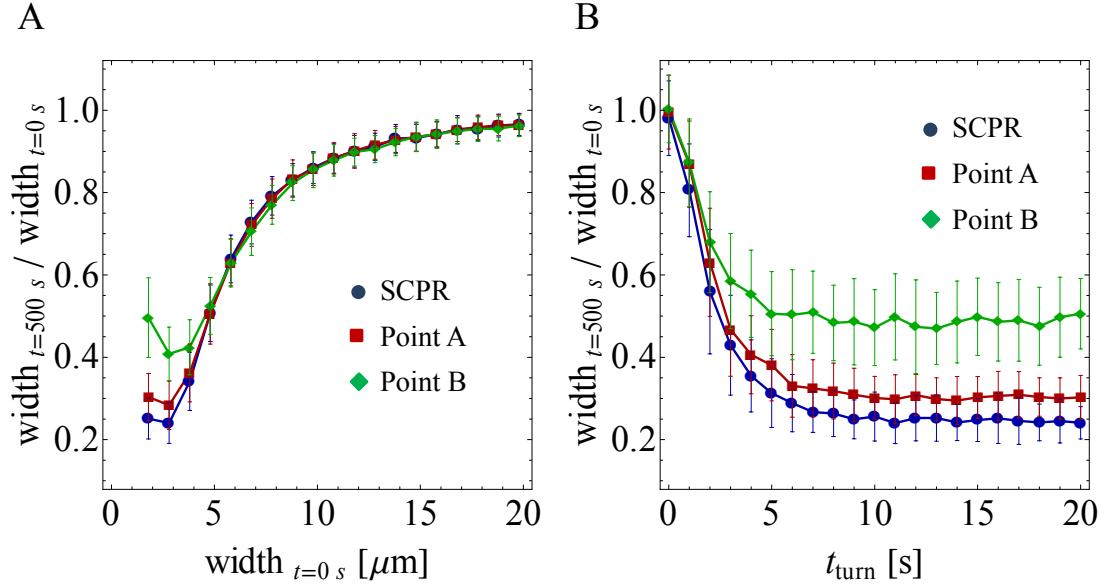


**Figure 18:** Results of simulations showing the ratio of band width at 500 s over initial band width versus unconnected filament turnover time  $t_{\text{turn}}$  and initial band width. Each point is an average of 100 simulations; error bars represent  $\pm$  one standard deviation. (A) Ratio of band width versus  $t_{\text{turn}}$  for parameter values corresponding to pure SCPR, and SCPR with the alignment mechanism. Two sets of alignment parameters are shown, corresponding to points A and B in Figure 14. All other parameters were fixed to the values described in the main text. Changes in  $t_{\text{turn}}$  influence the average filament length of unconnected filaments,  $t_{\text{turn}} v_{\text{pol}}$ , where  $v_{\text{pol}} = 0.2 \mu\text{m s}^{-1}$ . For small values of  $t_{\text{turn}}$ , the band of nodes fails to condense and small aggregates form. The behavior is similar for all three cases. Note that the case of ‘point B’ leads to wider bands compared to the other two cases (see Figure 16). (B) Ratio of band width versus initial width, as in panel (A). The number of nodes was changed in proportion to the initial width such that the average density of nodes remained unchanged. Very wide bands fail to condense to rings and the behavior is similar for all three cases.

### 4.3. Discussion

In the model presented here, the components of the ring are pulled together over long distances by a search and capture mechanism. This is followed by stabilization of these components into linear structures by a local alignment mechanism. The model reproduces morphologies observed in wild-type and mutant cells. Our simple implementation of

alignment motivated future experiments, described in Chapter 5, to resolve its precise molecular origin. In Chapters 5 and 6 the role of actin filament cross-linkers fimbrin *Fim1p* and  $\alpha$ -actinin *Ain1p* in the local alignment mechanism is investigated. Several other molecules may also contribute: *Myo2p*, *IQGAP Rng2p*, *Mid1p*. These proteins play an important role in cytokinesis of fission yeast and other organisms but their precise mechanistic role remains to be resolved. The results of 4.2 describe our expectations of how cells with perturbed alignment properties may behave. For example, we expect the ring porosity to increase when the alignment strength (parameter  $f_{al}$ ) is reduced, see Figure 14A. The alignment process proposed here could involve the recruitment of cytoplasmic proteins that stabilize the linear structures that form in a stochastic manner by search and capture. The cooperative nature of these interactions may be strong. We speculate that in systems with compromised nodes (such as deletions and mutations in the structural node component *Mid1p* [22, 23, 28]) this process may work in the reverse direction: bundling proteins may self-assemble into a linear structure first, recruiting missing node components in a second step. This could be the nature of the proposed ‘backup pathway’ for fission yeast ring assembly in *Mid1p* mutants [54, 55]. This would be consistent with the requirement of an active septation initiation network (SIN) pathway in these mutants [23, 28]: the SIN promotes ring maturation and constriction [56], so it could enhance the alignment mechanism.

The actin asters that are seen occasionally during fission yeast contractile ring assembly have provided evidence for the ‘leading cable’ model, an alternative to SCPR [20, 38-40]. In this model a *Cdc12p* spot at the center of the aster initiates the process of ring assembly. An interesting observation in Figure 15, Figure 16, and Figure 17 is that

intersecting and star-shaped node structures spontaneously form in these simulations. We speculate that the asters are the result of such self-organization processes rather than the result of a single nucleating spot. In the simple model presented here, actin filaments polymerize along random directions and so we do not have a mechanism for actin aster formation. However, coupling between the direction of actin polymerization and local node alignment could generate star-shaped actin structures. This would be reminiscent of star formation in other systems of mixtures of motors and filaments [2-4, 15].

In the following Chapter, I will present experimental findings (by our collaborators) of the role of actin filament cross-linkers during ring formation process and their role in the stability of actomyosin linear structures presented in this Chapter. These new experimental findings provided further motivation for more detailed modeling, described in Chapter 6, of the role of actin filament cross-linkers during the ring formation. In Chapter 6 I present one of the possible molecular mechanisms of actin filament cross-linking by  $\alpha$ -actinin and fimbrin in the process of local node alignment.

## 5. Role of actin filament cross-linkers $\alpha$ -actinin and fimbrin

In Chapter 4, I described a model of local node alignment that successfully accounted for linear structure formation during ring assembly, as well as node meshwork formation in *cdc25-22* cells. In this Chapter I present experimental results demonstrating the role of actin filament cross-linkers during ring formation in fission yeast. These experimental findings support the idea that actin cross-linkers play an important role in the formation and stability of linear structures. The experiments and data analysis were performed by Damien Laporte and Jian-Qiu Wu at The Ohio State University. Inspired by these new exciting findings I further developed the SCPR model, see Chapter 6, to explore a molecular mechanism of the cross-linkers in the ring formation process.

$\alpha$ -Actinins and fimbrins are actin bundling/cross-linking proteins with their biochemical properties characterized in vitro [57-61] and some crystal structures solved [62, 63]. Fimbrin monomers bundle actin filaments into tight bundles with two adjacent actin-binding domains (ABD).  $\alpha$ -Actinin cross-links actin filaments into a network by forming an antiparallel homodimer having one ABD on each polypeptide separated by spectrin-like repeats.  $\alpha$ -Actinins reduce disruption of the actin network in the presence of a severing factor and high-rate deformation in vitro [64, 65] and regulate the movements of single actin filaments through myosin-II [66]. However, the molecular mechanisms of their in vivo functions remain poorly understood.

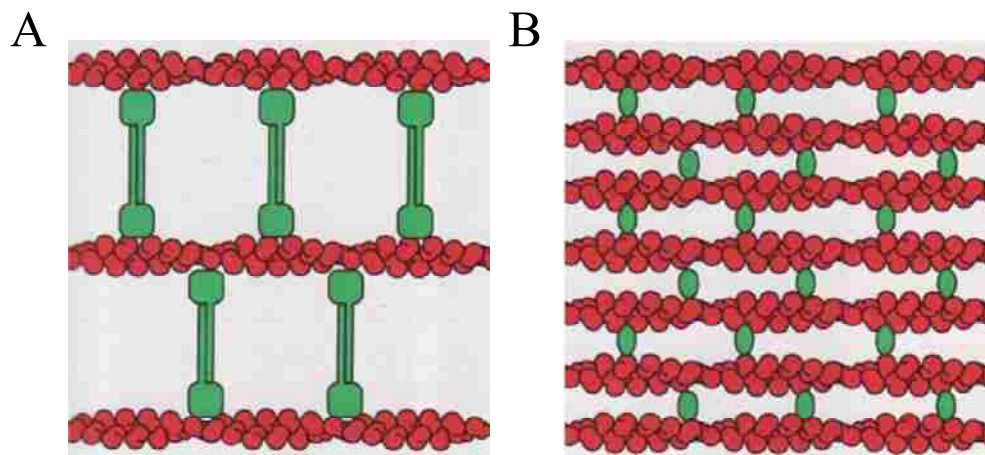


**Figure 19:** Cartoon of actin filament cross-linkers [67] (A)  $\alpha$ -actinin green; actin filaments red.  $\alpha$ -actinin cross-links actin filaments into a loose network with an anti parallel homodimer having one ABD on each polypeptide separated by long spectrin-like repeats. (B) Fimbrin green; actin filaments red. Fimbrin can bundle actin filaments into tight bundles with two adjacent actin-binding domains (ABD).

In fission yeast *S. pombe*,  $\alpha$ -actinin Ain1 and fimbrin Fim1 localize to the division site and have overlapping functions in cytokinesis [58, 60, 61, 68]. Genetic, deletion, and overexpression data indicate that Ain1 and Fim1 participate in contractile-ring formation [58, 68]. We hypothesized that actin cross-linkers  $\alpha$ -actinin Ain1 and fimbrin Fim1 contribute to the local node alignment suggested theoretically in Chapter 4. To test this idea we observed the condensation of nodes labeled with florescent myosin-II light chain Rlc1p or heavy chain Myo2p in strains with modified concentration of Ain1p and/or Fim1p.

Damien Laporte and Jian-Qiu Wu showed that Ain1 and Fim1 are essential for node condensation into the contractile ring. They found that these proteins stabilize linear actomyosin structures that form during late stages of node condensation and thus provide a mechanism for the proposed node alignment [69]. I developed a computational model

of how the observed actin network structures depend on the concentrations of actin cross-linkers and myosin motors, see Chapter 6. Collectively, our work indicates that  $\alpha$ -actinin and fimbrin are critical for contractile ring assembly by stabilizing linear actomyosin structures.

### 5.1. Cross-linker depletion experiments

In wild-type cells, a broad band of nodes condensed into a ring  $11.7 \pm 1.8$  min after the start of node condensation ( $n = 26$  cells; Figure 20A, top left). In *fim1* $\Delta$  cells (mutants that lack the gene for Fim1 protein), the ring formed normally ( $12.1 \pm 2.3$  min;  $n = 11$ ; Figure 20A, top right), consistent with previous reports [58, 68]. In contrast, ring formation was delayed in 62% *ain1* $\Delta$  cells (mutants that lack the gene for Fim1 protein) ( $27.5 \pm 13.0$  min;  $n = 56$ ). In *ain1* $\Delta$ , nodes formed normally but condensed into 1 to 3 clumps (Figure Figure 20A, bottom left), which took 10 to 30 additional min to rearrange into a ring.

The behavior in the absence of both cross-linkers was investigated next. Since *ain1* $\Delta$  *fim1* $\Delta$  (mutants that lack the gene for both Fim1 and Ain1 proteins) is synthetic lethal [68], the double deletion was mimicked by combining *ain1* $\Delta$  with *fim1* expressed from a *4Inmt1* promoter. Under the repressing condition (low levels of Fim1), ring formation was severely affected ( $54.5 \pm 10.4$  min,  $n = 36$ ) with Myo2 nodes always condensing into clumps (Figure 20A, bottom right). Thus, both Ain1 and Fim1 are involved in proper node condensation. In the strain *ain1* $\Delta$  *4Inmt1* *fim1* (absence of Ain1p

and depleted level of Fim1p) node movement was affected. In this strain nodes preferentially move long distances toward already formed clumps as quantified in Figure 20C.

The actin dynamics was also quantified in deletion mutants. Cells expressing GFP-CHD (fluorescent protein that binds to the sides of actin filaments) were treated with 10  $\mu$ M of Latrunculin A (Lat-A). Lat-A is a drug that sequesters actin monomers, preventing formation of F-actin filaments. *ain1* $\Delta$  cells were more sensitive to Lat-A treatment than wild type cells (Figure 20, D and E). The decay rate of GFP-CHD fluorescence intensity in the contractile ring was  $t_{1/2} = 2.3 \pm 0.8$  min in wild-type compared to  $1.0 \pm 0.3$  min in *ain1* $\Delta$  (Figure 20E). This indicates that the actin network in the ring is less stable without Ain1.

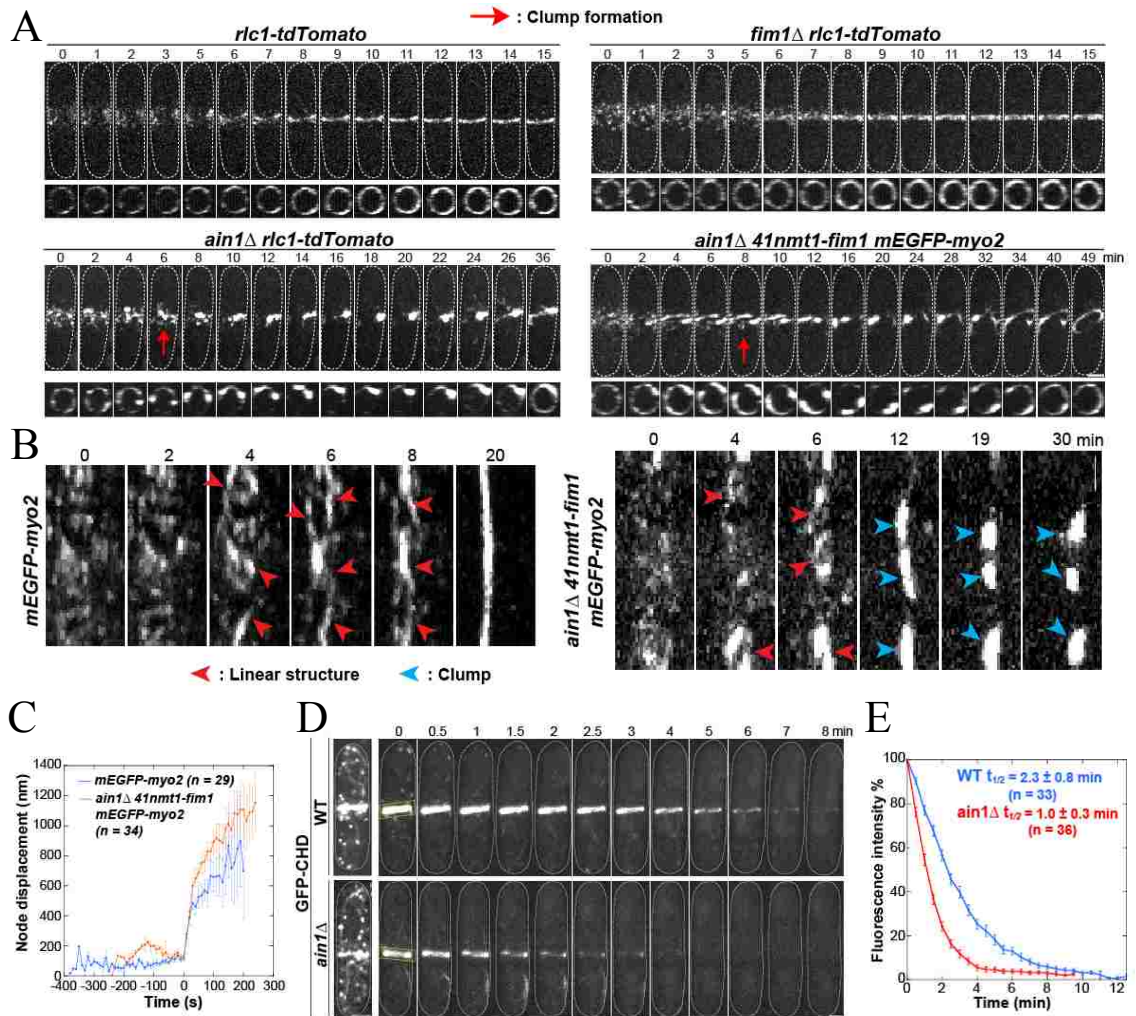


**Figure 20:** Normal node condensation during contractile-ring assembly depends on  $\alpha$ -actinin Ain1 and fimbrin Fim1 (D. Laporte and J.-Q. Wu). Start of node condensation is defined as time 0. (A) Time courses of node condensation in wt, *fim1* $\Delta$ , *ain1* $\Delta$ , and *ain1* $\Delta$  *41nmt1-fim1* cells. Deletion (or depletion) of *ain1* and/or *fim1* induces clump formation during node condensation. Elapsed times are in min. Top panels are maximum intensity projections of 3D confocal microscopy stacks; lower panels are 90° rotations. (B) Radial projections of mEGFP-Myo2 forming linear structures and clumps during node condensation in WT and *ain1* $\Delta$  *41nmt1-fim1* strains respectively. (C) Nodes travel a longer distance (mean  $\pm$  SEM) in *ain1* $\Delta$  *41nmt1-fim1* cells. (D and E) Actin ring is more dynamic in *ain1* $\Delta$ . WT and *ain1* $\Delta$  cells expressing *41nmt1-GFP-CHD* were grown 22 h in EMM5S, pre-incubated with 100  $\mu$ M Arp2/3 inhibitor for 5 min, then treated with 10  $\mu$ M Lat-A and imaged immediately at time 0. (D) The cells before time 0 are untreated with either inhibitor. (E) Fluorescence decay curves of GFP-CHD after Lat-A treatment with half time (mean  $\pm$  SD) and cells analyzed indicated. Fluorescence intensity of GFP-CHD ring within yellow box as depicted in E was measured. Cells were grown in YE5S for 22 h. Bars 2  $\mu$ m.



## 5.2. Cross-linker overexpression experiments

As node condensation depends on actin network dynamics [13], the effect of Ain1p overexpression on actin network stability was analyzed. In most anaphase *3nmt1-ain1* cells that have increased concentration of Ain1p, GFP-CHD labeled actin filaments coalesced slowly into disorganized actin structures instead of a contractile ring, with several thick and stable bundles (Figure 21, A and B). Node movement in Ain1p overexpression was severely reduced, see Figure 21C. In cells overexpressing Ain1p, actin bundles were more stable compared to wild type actin rings, as revealed by treating cells with 10  $\mu$ M Lat-A (Figure 21D). The  $t_{1/2}$  of decay for GFP-CHD was  $5.8 \pm 2.3$  min in *3nmt1-ain1* cells, 2.5-fold slower than that in wild-tupe (Figure 21E). The results of overexpression experiments showed that increasing Ain1p concentration inhibits node movement and disrupt actin filament dynamics.

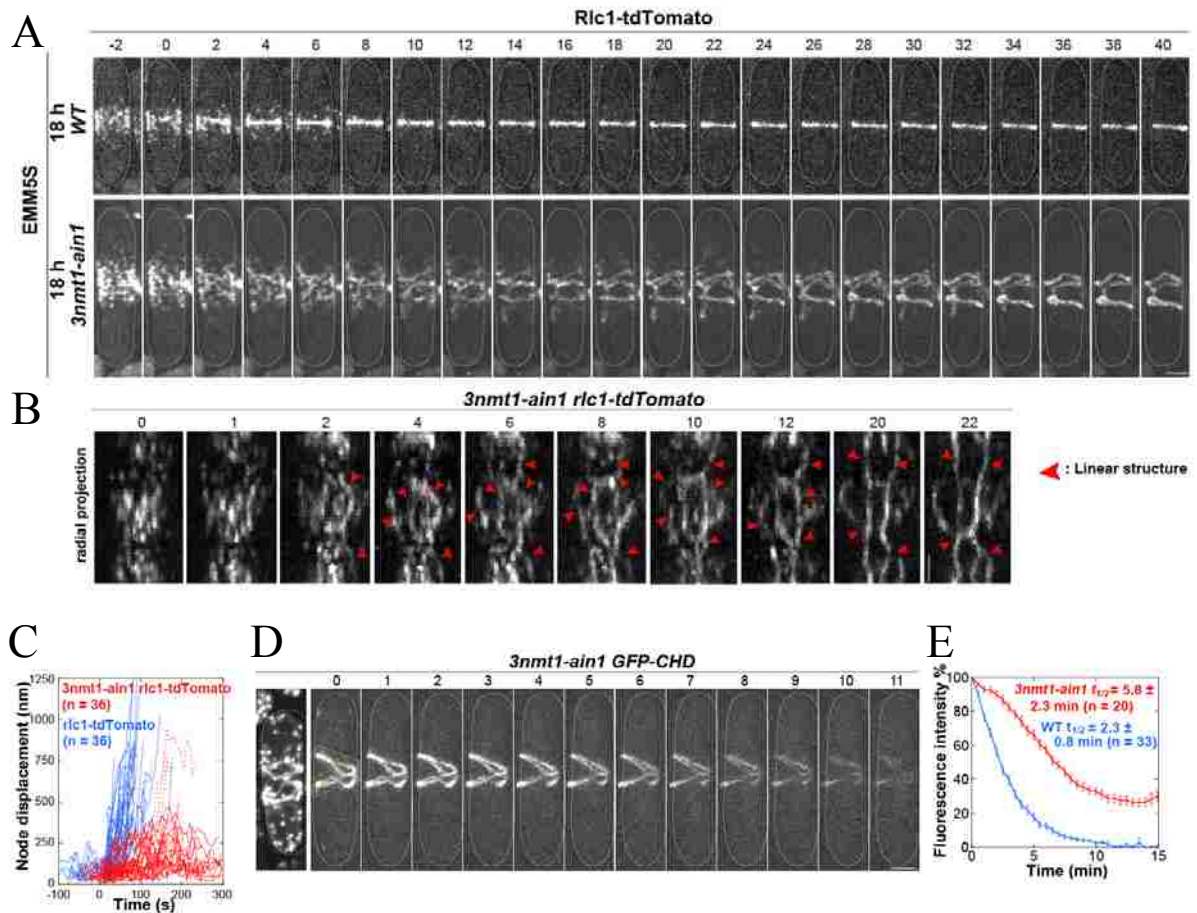


**Figure 21:** Ain1 overexpression promotes the formation of stable linear structures during contractile-ring formation. (A) Ain1 overexpression affects node condensation into the contractile ring. Strains expressing both Ric1-tdTomato and mEGFP-Ain1 (under strong 3nmt1 promoter) were imaged. Inducing time in EMM5S is indicated. (B) Nodes condense into numerous linear structures when Ain1 is overexpressed. Elapsed times are in min. (C) Ain1 overexpression affects individual node displacements. Nodes were tracked over time with a delay of 7 s in wt (blue lines) and 3nmt1-ain1 (red lines). Each line represents an individual node's movement. Red dashed lines are individual displacements > 500nm (6 out of 36 total measurements) for 3nmt1-ain1. (D) The cell before time 0 is untreated with either inhibitor. Times in min. (H) Fluorescence decay curves of GFP-CHD after Lat-A treatment with half time (mean  $\pm$  SD) and cells analyzed indicated. Fluorescence intensity of GFP-CHD ring within yellow polygon as depicted in D was measured. Bars 2  $\mu$ m.

To investigate how actin filament cross-linking may contribute to node alignment into linear structures and ring organization, we revised the SCPR model to include cross-linking among actin filaments. In the model of the following Chapter we assume that the

biological system is robust enough to allow an approximate description with a model that includes the most important mechanisms revealed by experiments, such as actin polymerization, myosin pulling, and cross-linking.

## 6. Model of role of actin cross-linker in ring assembly

In this Chapter I will present a modified version of SCPR model with actin filaments as semi-flexible polymers that can cross-link with one another in the presence of cross-linkers. The purpose of this modeling is to interpret the experimental findings presented in Chapter 5 and thus to develop a mechanistic understanding of actin filament cross-linking during ring self-organization.

In the original SCPR model, filaments are represented as straight lines (see Chapters 2 and 4). Here we model actin filaments as semi-flexible polymers consisting of beads connected by springs, see Appendix. With this new model of actin filaments as semi-flexible polymers, the effect of actin filament cross-linking was explicitly simulated. In our coarse-grained description we represent cross-linking by an attractive interaction between filament beads. In this model linear actomyosin structures self-organize spontaneously through collective interaction among nodes, actin filaments, and cross-linkers (see Section 6.1), unlike in Chapter 4 where we explicitly imposed a node-aligning mechanism.

## 6.1. Model

We used the Langevin equation to model the dynamics of actin filaments in 2D. Filaments are modeled as strings of beads connected with springs. To solve for the position  $\mathbf{r}_i(t)$  of the  $i^{\text{th}}$  filament bead we used following equation [70, 71]:

$$\zeta_b \frac{d\mathbf{r}_i}{dt} = \mathbf{F}_i^{\text{spr}} + \mathbf{F}_i^{\text{bend}} + \mathbf{F}_i^{\text{stoch}} + \mathbf{F}_i^{\text{xlink}} + \mathbf{F}_i^{\text{myo}}. \quad 15$$

Here, the first three terms on the right hand sides are described in Appendix, see Equation 16. In Appendix, I also describe details of how free semi-flexible filaments were modeled and how the expected static and dynamic properties of simulated filaments were reproduced. In the paragraphs below I will describe the basic processes of the model.

Search (See Figure 22A): Each node polymerizes two actin filaments in random directions on a 2D plane, as expected from the presence of  $\sim 2$  formin Cdc12 dimers per node [72-74]. Formins polymerize actin monomers while remaining attached to the barbed end. Single filament polymerization out of nodes was simulated by increasing the equilibrium length of the spring that joins the node and the first filament bead (see Figure 22A). The polymerization rate (the speed of length elongation of the first segment) was  $v_{\text{pol}} = 0.1 \mu\text{m/s}$ , the typical polymerization rate during early stages of cytokinesis [72]. Once the length of the growing segment was larger than  $l_0$ , a new bead was introduced. We kept the polymerization rate constant but we also run simulations with polymerization rate decreasing linearly with force (compressing or extensional) applied to the filament bead on the polymerizing node, up to stall force  $F_{\text{stall}}^{\text{pol}}$ , as suggested in [13]; (see Supplemental Figure 1C).

We assume that each filament starts to grow at a random angle  $\varphi_{\text{pol}}$ . To maintain that angle, we assume a restoring torque on the first bead by applying a force  $F_1^{\text{rot}} = k_{\text{rot}}(\varphi_{\text{pol}} - \varphi_1)/l_0(t)$ , where  $\varphi_1$  is the current angle of the first bead of the filament,  $k_{\text{rot}}$  is a constant and  $l_0(t)$  is the length of the first segment. The direction of the restoring force was perpendicular to the direction of the axis of polymerization. A force of the same magnitude but along the opposite direction was exerted on the polymerizing node. Additionally, to enable rotation of the polymerization axis, we allowed the axis of filament polymerization to rotate towards the current position of the first bead in response to the restoring torque, with rate  $\dot{\varphi}_{\text{pol}} = -k_{\text{rot}}(\varphi_{\text{pol}} - \varphi_1)/\zeta_{\text{rot}}$ , where  $\zeta_{\text{rot}}$  is an orientational drag coefficient (so  $\varphi_{\text{pol}}$  is fixed in the limit of large  $\zeta_{\text{rot}}$ ). In the simulations below we used  $k_{\text{rot}}/l_0 = 10 \text{ pN/rad}$  and  $k_{\text{rot}}/\zeta_{\text{rot}} = 10 \text{ s}^{-1}$ . With these values, the axis of polymerization can rotate due to forces by myosin and cross-linkers. In Supplemental Figure 1B, we examine the effects of  $\zeta_{\text{rot}}$  and show that node condensation into a ring is not strongly influenced by the value of  $\zeta_{\text{rot}}$ . This parameter controls the alignment of actin filaments along nodes and could represent a mechanism related to the process of actin compaction into a bundle during ring maturation [13].

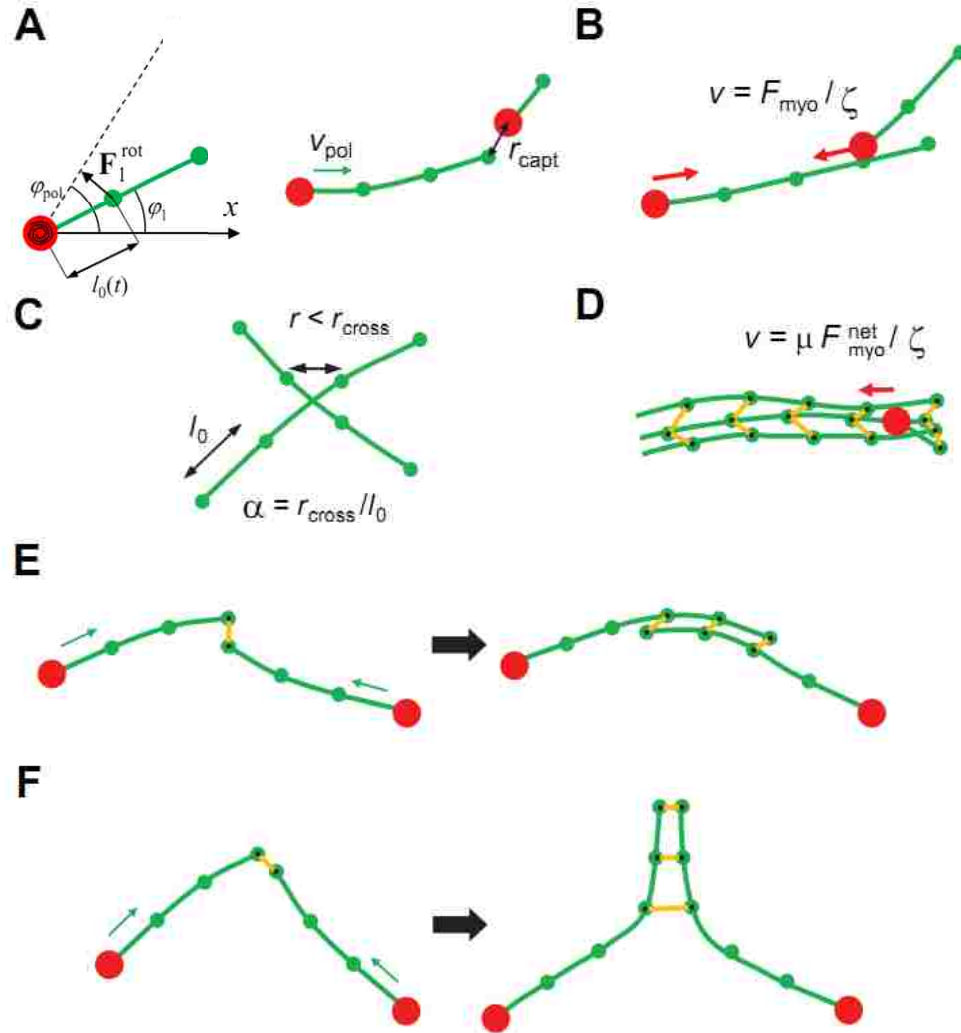


**Figure 22:** Summary of basic processes of SCPR model with actin filament cross-linking (A) Search (Left): The equilibrium length of the spring connecting the node and first filament bead,  $l_0(t)$ , increases with time due to the polymerization of the filament by formins at the node. The actin filament polymerizes at an angle  $\varphi_{\text{pol}}$ . A restoring torque proportional to  $\varphi_{\text{pol}} - \varphi_1$  pushes the filament towards the preferred angle. Capture (Right): Actin filaments polymerize out of nodes  $v_{\text{pol}}$  (the barbed ends of filaments are assumed to associate with formins at nodes). Actomyosin connections are established when filament beads come within  $r_{\text{capt}}$  to the other node. Filament lifetime is  $t_{\text{turn}}$  (“release”). (B) Pull: nodes bound to a filament exert force  $F_{\text{myo}}$  towards the barbed end of the filament at the nucleating node. The force is transmitted through the filament and results in node pairwise movement with velocity  $v = F_{\text{myo}}/\zeta$ . (C) Crosslinking occurs when two actin filament beads are within distance  $r_{\text{cross}}$  of one another (represented by an interaction potential between beads). (D) Nodes that establish multiple actomyosin connections inside an actin bundle exert lower total force per filament. (E and F) Depending on the angle of intersection, growing filaments can align into antiparallel (E) or parallel (F) bundles.

Capture and pull (See Figure 22A and B): When the distance between a filament bead and a node,  $r$ , is less than the capture radius  $r_{\text{capt}} = 0.15 \mu\text{m}$ , an actomyosin connection is established [13]. The bead-node connection was simulated by introducing an elastic interaction between bead and node with spring constant  $k_{\text{bead-node}} = 2 \text{ pN}/\mu\text{m}$  and equilibrium length  $0 \mu\text{m}$  (see Supplementary Table 1). Upon establishing a connection, the node exerts an additional pulling force on the filament bead of magnitude  $F_{\text{myo}}^0 = 4 \text{ pN}$  [13]) directed towards the barbed end and tangentially along the filament, see Equation 15. An equal and opposite force is transmitted through the filament on the connected node. Nodes can establish only one connection with the same filament but are able to connect with many filaments simultaneously. To limit the magnitude of pulling forces when nodes connect with bundles of filaments, we assume that the pulling force exerted on a filament bead is reduced by a factor that depends on the number of bead-bead cross-links  $N_c$  of the filament bead,  $F_{\text{myo}} = \mu F_{\text{myo}}^0 / N_c$  (Figure 22D), for  $N_c \geq 1$ . We used  $\mu = 0.3$  (see model dependence on  $\mu$  in Supplemental Figure 1A). This reduction in force represents the myosin force being distributed over many filaments and interference of myosin activity with actin cross-linkers.

Turnover and release: The average filament lifetime was  $t_{\text{turn}} = 20 \text{ s}$  [13] (thus, the typical filament length was  $t_{\text{turn}} v_{\text{pol}} = 2 \mu\text{m}$ ). In the simulations, each filament disappears with probability  $\Delta t / t_{\text{turn}}$  every  $\Delta t = l_0 / v_{\text{pol}}$  and a new filament starts to grow in a new, randomly chosen direction. Filament beads can disengage from nodes when the applied forces cause the node and connected filament bead to drift apart beyond  $r_{\text{capt}}$ .

Cross-linking (See Figure 22C and E, and F): We modeled actin cross-linkers as elastic springs producing force:  $\mathbf{F}_i^{\text{xlink}} = -\frac{k_{\text{cross}}}{2} \sum_j \frac{\partial (|\mathbf{r}_i - \tilde{\mathbf{r}}_j| - l_x)^2}{\partial \mathbf{r}_i}$ , where the sum is over all beads of other filaments at position  $\tilde{\mathbf{r}}_j$  that are within  $r_{\text{cross}}$  of bead  $i$ . Thus, when bead  $i$  is within  $r_{\text{cross}}$  of bead  $j$  of another filament, we introduce an elastic interaction between



the beads, with spring constant  $k_{\text{cross}}$  and natural length  $l_x$ . The rate of cross-linking was tuned by adjusting the range of this interaction potential, described by parameter  $\alpha$  (which is defined to be equal to the ratio of the range of the interaction potential over the distance between the beads). Small (large) values of  $\alpha$  correspond to slow (fast) cross-linking rates between filaments. The magnitude of the cross-linker dissociation rate depends on both  $\alpha$  and the depth of the interaction potential,  $k_{\text{cross}}$ . We assume  $k_{\text{cross}}$  is sufficiently small to allow antiparallel bundles to form by filaments that grow towards one another while remaining aligned (Figure 22E and F). Strong cross-linking of growing filaments (large  $k_{\text{cross}}$ ) results in filament buckling and alignment into parallel cable-like bundles (Figure 22F). Most actin cross-linkers bind to actin filaments transiently in vitro [75, 76], consistent with our assumption of small enough  $k_{\text{cross}}$ . We do not impose node alignment by forces other than those that arise from cross-linkers, unlike in Chapter 4 [69]. This simple linear spring model is sufficient to illustrate the main qualitative changes in network morphologies as a function of degree of cross-linking. However, the precise location of these morphological transitions in parameter-space may depend on additional affects such as non-linear torques that lead to cooperative effects and geometric alignment that we do not include in the model. In simulations below we used  $k_{\text{cross}} = 0.5 \text{ pN}/\mu\text{m}$  and  $l_x = 0.05 \mu\text{m}$ . Since  $l_x$  represents the average distance between two cross-linked actin filament segments, we used a value slightly larger than the length of the  $\alpha$ -actinin dimer [62, 63]. Values of  $l_x$  in the range 0 - 80 nm produced similar results (see Supplementary Table 1). Parameters  $k_{\text{cross}}$  and  $\alpha \equiv r_{\text{cross}} / l_0$  represent the effective strength and dynamics of cross-linking and their importance are examined in Figure 26.

*Forces on nodes:* The position of a node,  $\mathbf{r}_{\text{node}}$ , is found by solving  $d\mathbf{r}_{\text{node}}/dt = \mathbf{F}_{\text{node}}^{\text{total}} / \zeta_{\text{node}}$ , where the node drag coefficient was  $\zeta_{\text{node}} = 400 \text{ pN s}/\mu\text{m}$  [13]. The total force on the node,  $\mathbf{F}_{\text{node}}^{\text{total}}$ , is the sum of the following four forces. (i) Elastic forces transmitted through filaments polymerizing out of the node. We calculate these

forces by treating the node as a bead of an actin filament. (ii) Forces due to the elastic spring that connects the node to filaments that polymerized out of other nodes. (iii) Myosin pulling force when nodes connect to actin filaments polymerizing out of other nodes. This force is of equal and opposite magnitude to the force that the node exerts on the actin filaments. (iv) Force due to excluded volume interactions among neighboring nodes when two nodes are within  $0.20\ \mu\text{m}$  of one another, represented by a repulsive radial force of magnitude  $80\ \text{pN}$  [13] (see Supplementary Table 1).

*Numerical integration:* Nodes were distributed in a sufficiently long 2D strip with density 65 nodes per  $12\ \mu\text{m}$ , according to a Gaussian distribution with standard deviation  $0.9\ \mu\text{m}$ . The positions of nodes and filament beads were calculated by integrating the above equations using a time step  $5 \cdot 10^{-4}\text{s}$ . We validated the simulations of actin as semi-flexible filaments by checking that we obtain the correct persistence length, tangent correlation function and curvature distribution in thermal equilibrium, see Appendix. We also confirmed that the relaxation time of each Fourier mode of the simulated filaments was in agreement with the analytical results, see Appendix.

## 6.2. Results

Simulations reproduced the formation of the clumps, rings, or meshworks during node condensation as the strength of cross-linking is varied through parameter  $\alpha$ . Snapshots in Figure 23 for three values of  $\alpha$  closely match the phenotypes observed in cross-linker deletion mutants, wild type, and *Ain1* overexpression cells. Without cross-linkers ( $\alpha = 0$ ), clumps form (clump instabilities were enhanced compared to the original SCPR model by allowing filaments to make contact with multiple nodes [13], see

Chapter 2). In the simulations that correspond to wild type cells ( $\alpha = 0.7$ ), alignment of nodes through cross-linked actin filaments prevents them from coalescing into clumps. However, this alignment is transient and does not trap nodes into stable linear meshwork structures, as observed when growing filaments are strongly cross-linked ( $\alpha = 1$ ). When nodes condense into rings, the rings consist of bundles of antiparallel filaments, see Figure 23B. For more details on node statistics and comparison with experiments see Supplementary Figure 2.

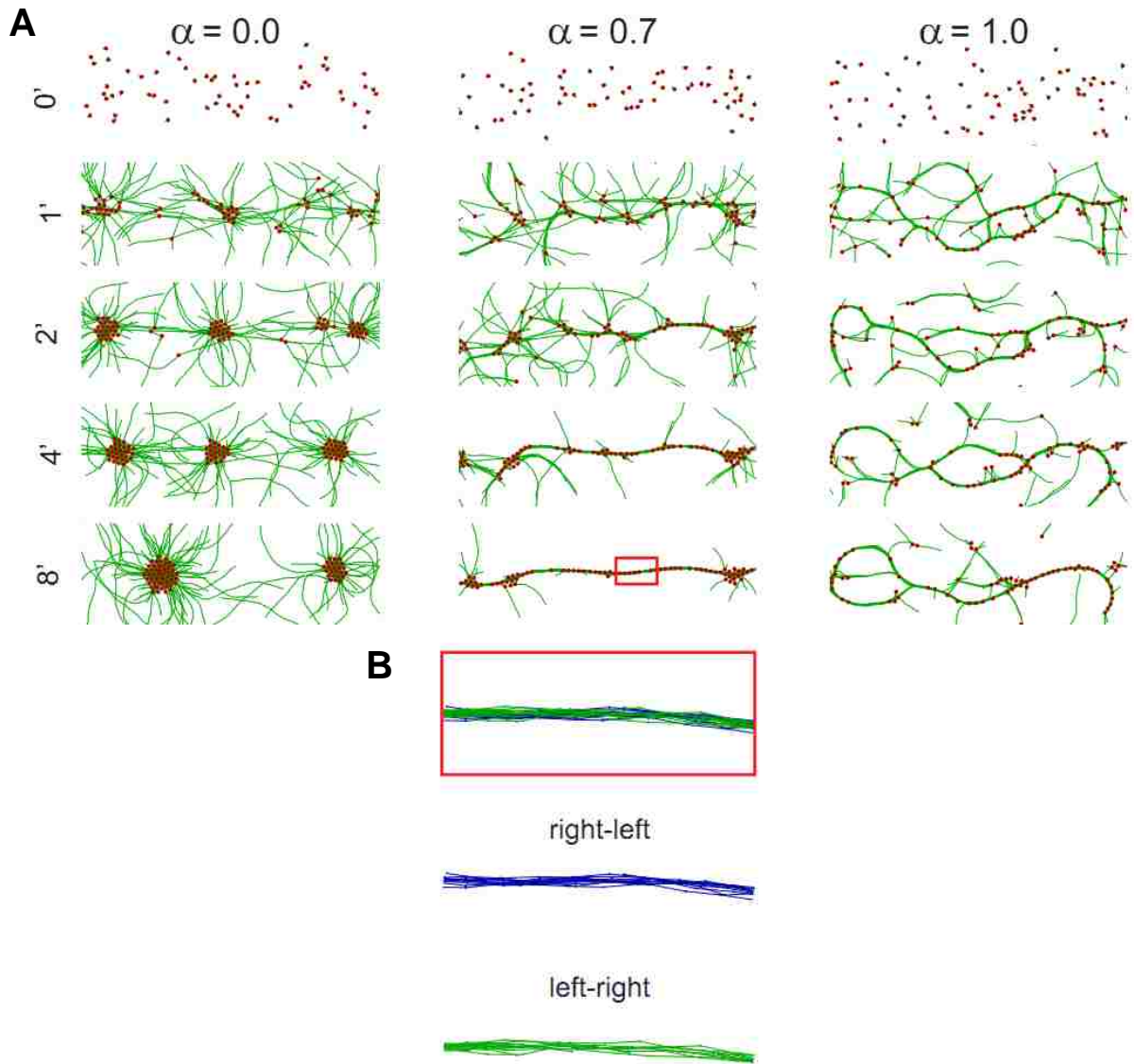


**Figure 23:** Snapshots of 2D simulations of node condensation for different values of parameter  $\alpha = r_{\text{cross}}/l_0$ . (A) Cases  $\alpha = 0$  (no cross-linking, similar to *ain1Δ fim1Δ* cells), 0.7 (moderate cross-linking as in wt cells), and 1 (excessive cross-linking as in *Ain1p* overexpression cells) show formation of clumps, rings, and meshworks, respectively. Times in min. (B) Snapshots of actin filament arrangements in the red box in A ( $\alpha = 0.7$ , 8 min). The bundle consists of both parallel and antiparallel filaments: blue (green) indicates filaments whose barbed-to-pointed end direction is towards left (right).

Plots of broad band width versus time (Figure 24A and B) match experimental observations: with increasing cross-linker concentration (increasing  $\alpha$ ) bands condense slower and slower and eventually fail to condense. Figure 24C and D shows how the largest gap develops over time. Gaps do not grow far above the diffraction limit for sufficiently high  $\alpha$  while large gaps that correspond to the formation of 2-3 clumps develop for  $\alpha = 0$ , see clump formation in Figure 20B. Similar agreement is found for 2D porosity and cross-linker concentration (Figure 25): The 2D porosity for large times of order 400 s increases with increasing *Ain1p* concentration, similarly to simulations where porosity was increasing by increasing parameter  $\alpha$ .

Experimental measurements of the number of *Ain1p* cross-linker molecules at the division site are shown in Figure 25C. The decay in the number of molecules at the times larger than 40 min corresponds to the ring constriction process; while the ring constricts, it loses most of its material. Our simulations do not model these late stages, however, a trend similar to experiments is found for the first 10 minutes, see Figure 25D.

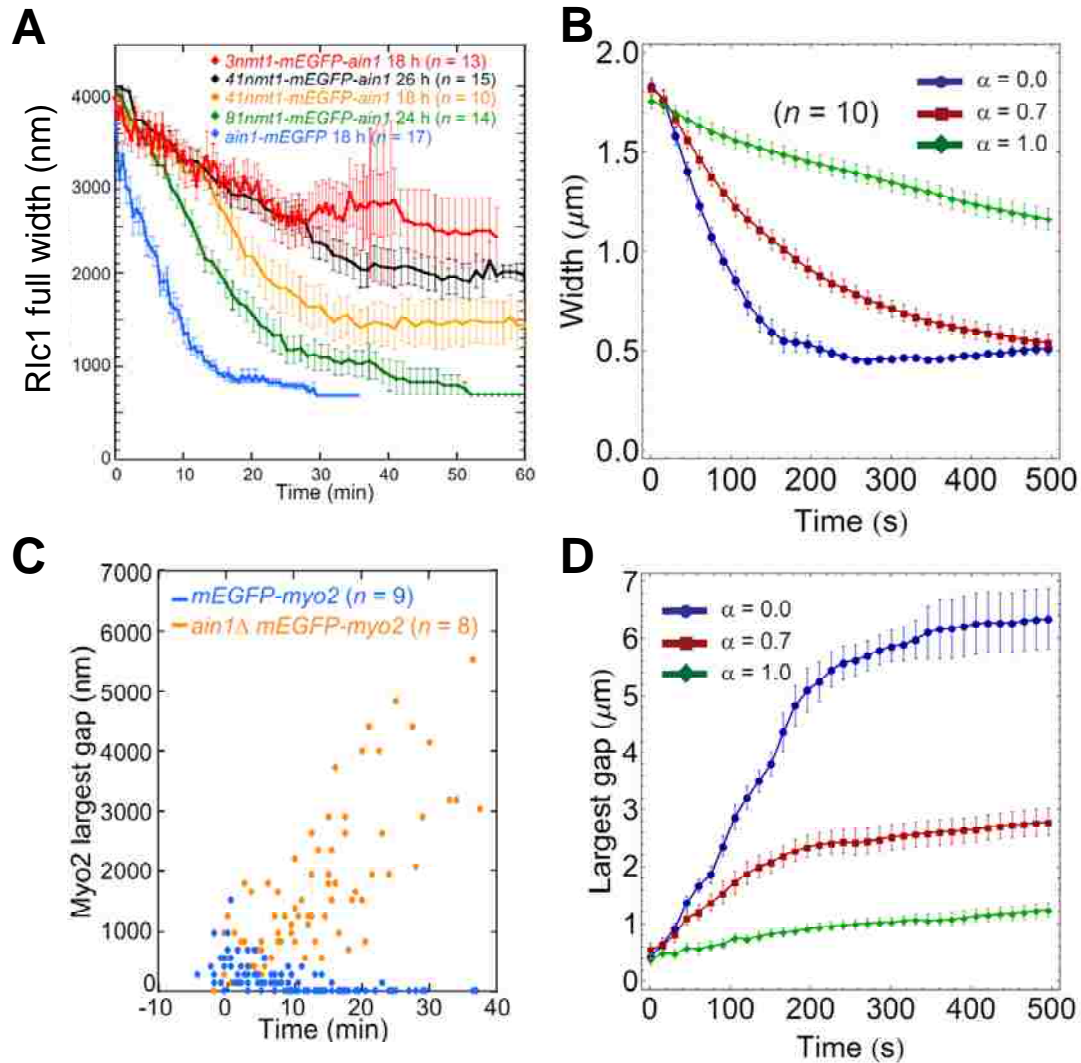


**Figure 24:** Width and largest gap of node bands in experiments and simulations. Experimental data in left column (D. Laporte); simulation data in right column. (A) Rates of node condensation have an inverse relationship with *Ain1* concentrations. Full width of Rlc1 broad band (mean  $\pm$  SEM) was measured over time. Strains, times grown in EMM5S, and numbers of cells analyzed are depicted. (B) Node band width vs. time for different values of parameter  $\alpha$ . Band width is calculated as 2 SDs of  $y$  node coordinates. Increased cross-linking slows down condensation. (C) Largest gap visualized by mEGFP-Myo2 during node condensation in *ain1* $\Delta$ . (D) Largest gap vs. time and  $\alpha$ . Absence of cross-linking results in disconnected node aggregates, similarly to experiments.

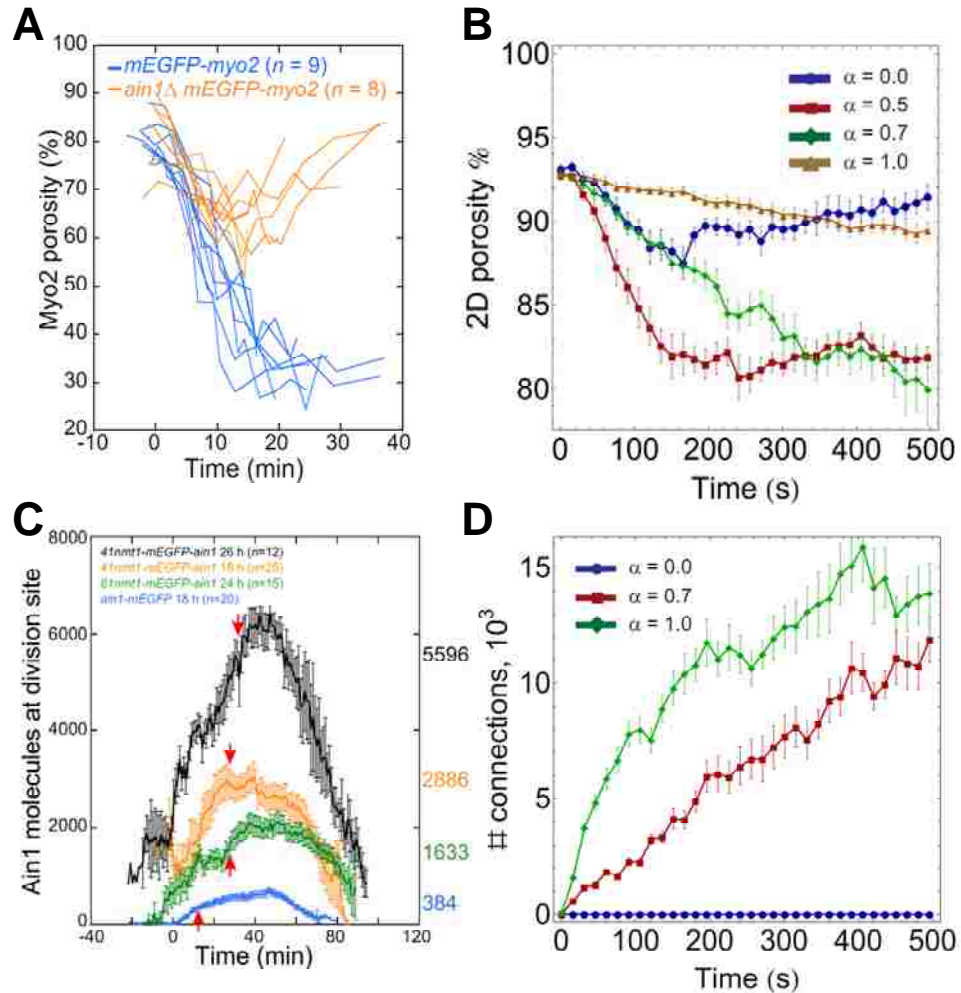


**Figure 25:** Node band porosity and number of cross-linkers in experiments and simulations. Experimental data in the left column (D. Laporte); simulation data in the right column. (A) 2D band porosity measured in wt and strain without alpha-actinin vs time. (B) 2D porosity vs. time for different values of parameter  $\alpha$ , with other parameters kept constant. Porosity was calculated using a grid box size of  $0.2 \mu\text{m}$  and counting empty boxes. As time progresses the total width of the grid was considered to be equal to two standard deviations of  $y$  node coordinates. The total length of the grid was kept constant and equal to the cell circumference. 2D porosity was defined as total number of empty boxes divided by total number of boxes. Failure of condensation into rings in the absence or over-expression of cross-linkers is indicated by large porosity at long times. Error bars are SEM ( $n = 10$  simulations). (C) Local Ain1p abundance at the division site (mean  $\pm$  SEM) increases with the strength of *nmt1* promoters. Number of node molecules is measured as in [24]. The colored numbers are the Ain1p molecules at the end of node condensation, indicated by red arrows. Inducing time in EMM5S is indicated. (D) Total number of actin filament bead cross-links vs. time and  $\alpha$  shows a trend similar to experiments. Average  $\pm$  SEM is shown ( $n = 10$ ).

The full dependence of resulting node aggregation on model parameters  $\alpha$  and  $k_{\text{cross}}$  is shown in Figure 26 that illustrates how cross-linker properties lead to different cytoskeletal organization and recapitulates the in vivo observations. Width, largest gap, and 2D porosity were used to determine the region of parameter space where cross-linkers have a beneficial role. For large  $k_{\text{cross}}$  we observed predominantly parallel filament bundles while for smaller  $k_{\text{cross}}$  we observed parallel and anti-parallel bundles. With changing parameter  $\alpha$  from low to high we can see a transition from clumps to rings to meshwork as observed in experiments (increasing Ain1p abundance). Fission yeast may have optimized cross-linker concentration and rate constants to lie in the functional region. Our simulations thus support a mechanism in which actin cross-linking aligns actin filaments within transient bundles, which in turn define how nodes condense.



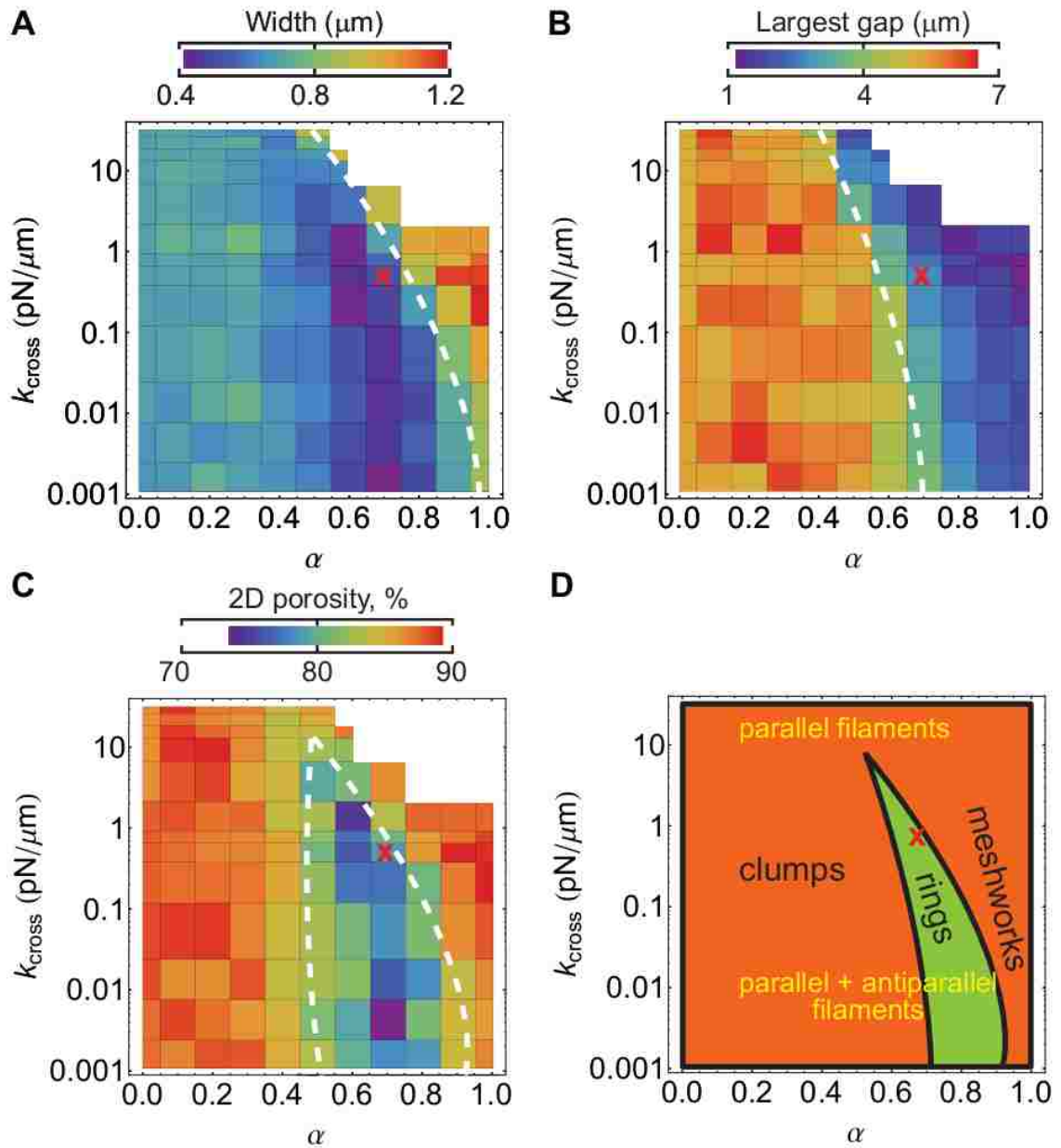


**Figure 26:** Dependence of node aggregate structures on cross-linker model parameters. (A-C) Width, largest gap, and 2D porosity vs.  $\alpha$  and  $k_{\text{cross}}$ , calculated 500 s after the start of simulation (mean of 10 runs). Dashed lines separate physiological from non-physiological regions. White area: cross-linking is too strong for meaningful simulations. Red X mark: parameters used in Figure 23, wild-type case (the optimal case). The  $\alpha$ -dependence for very small  $k_{\text{cross}}$  is due to our use of  $\alpha$  in counting actin filaments in a bundle and resulting reduction of myosin pulling (Figure 22D). 2D porosity is measured as in Figure 25B. (D) Summary of preceding panels showing region with successful ring formation.

The above numerical simulations show node condensation is a cooperative process in which the actin network and nodes affect each other. Without myosin pulling, actin cross-linking in the model does not provide enough force to pull nodes together, resulting in a transient meshwork structure of actin filaments (Figure 27, A and B). Interestingly, when  $\alpha = 1$ , the simulations show that cross-linking resists node movement induced by myosin pulling (Figure 27C). We thus predict that sufficiently high myosin pulling forces can overcome the restriction imposed by cross-linking activity and condense actomyosin meshworks into rings in *Ain1* overexpression cells (Figure 27, C and D).

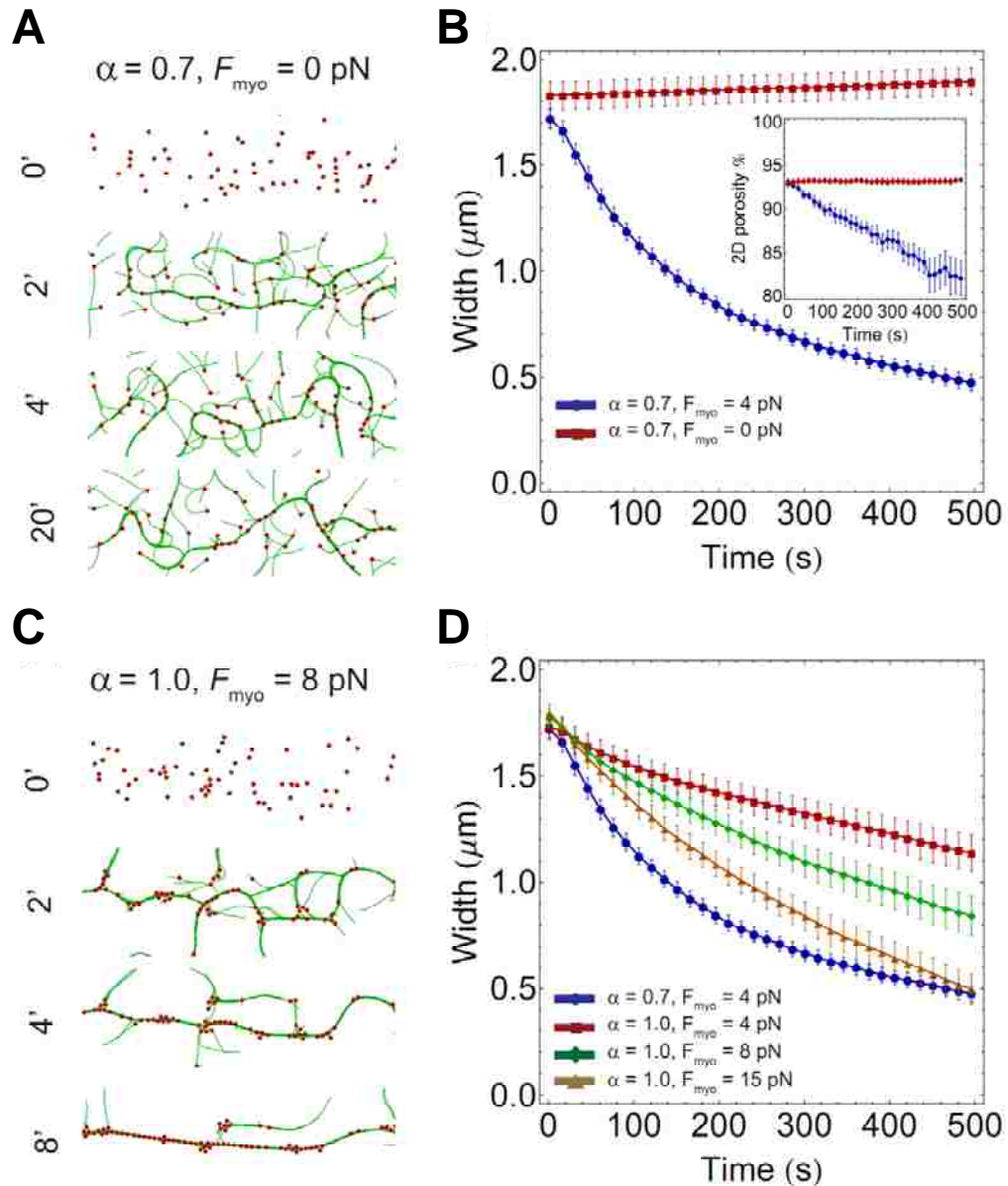


**Figure 27:** Model prediction of cooperation between Myo2 activity and Ain1 cross-linking. (A and B) Simulations including cross-linking but insufficient myosin motor activity predict meshwork of bundles that fail to condense into rings. (A) Snapshots show ring formation with  $\alpha = 0.7$ ,  $F_{\text{myo}} = 0$  pN. (B) Band width vs. time and  $F_{\text{myo}}$  with all other parameters fixed. Inset: 2D porosity vs. time (measured as in Figure 25B) shows porous meshworks at small  $F_{\text{myo}}$ . (C and D) Nodes that freeze into meshworks due to excessive cross-linking ( $\alpha = 1$ ) can condense into rings by increasing the myosin pulling force in simulations. (C) Snapshots show ring formation with  $\alpha = 1$ ,  $F_{\text{myo}} = 8$  pN (compare to meshwork for  $\alpha = 1$ ,  $F_{\text{myo}} = 4$  pN in Figure 23A). (D) Band width (measured as in Figure 24B) vs. time and  $F_{\text{myo}}$ , keeping other parameters fixed, shows faster condensation with increasing  $F_{\text{myo}}$ . (B and D) Error bars are SEM ( $n = 10$  simulations).

Damien Laporte performed experiments to test my predictions that are summarized in Figure 27. Consistent with prior reports [72, 77], he found that *myo2-E1* cells with defective Myo2 motor activity could not condense nodes and the actin network into a contractile ring, forming instead a dynamic meshwork similar to the simulations (Figure 28A). We expect that increasing myosin concentration increases the node pulling force, since nodes condense into a compact ring 2-fold faster in cells with two copies of the *myo2* gene [77]. As predicted by the simulations, in *2x myo2 4Inmt1-ain1* (overexpression of Myo2p and Ain1p) cells, nodes condensed more normally with less tilted/double rings compared to *4Inmt1-ain1* cells that only overexpress Ain1p (Figure 28B and C). The overall node condensation speed was 106 nm/min in *2x myo2 4Inmt1-ain1* cells, compared to 206 nm/min in wild-type and 53 nm/min in *4Inmt1-ain1* (Figure 28C). Together, these results further support that node condensation is a cooperative process in which myosin-II and actin cross-linkers affect each other.

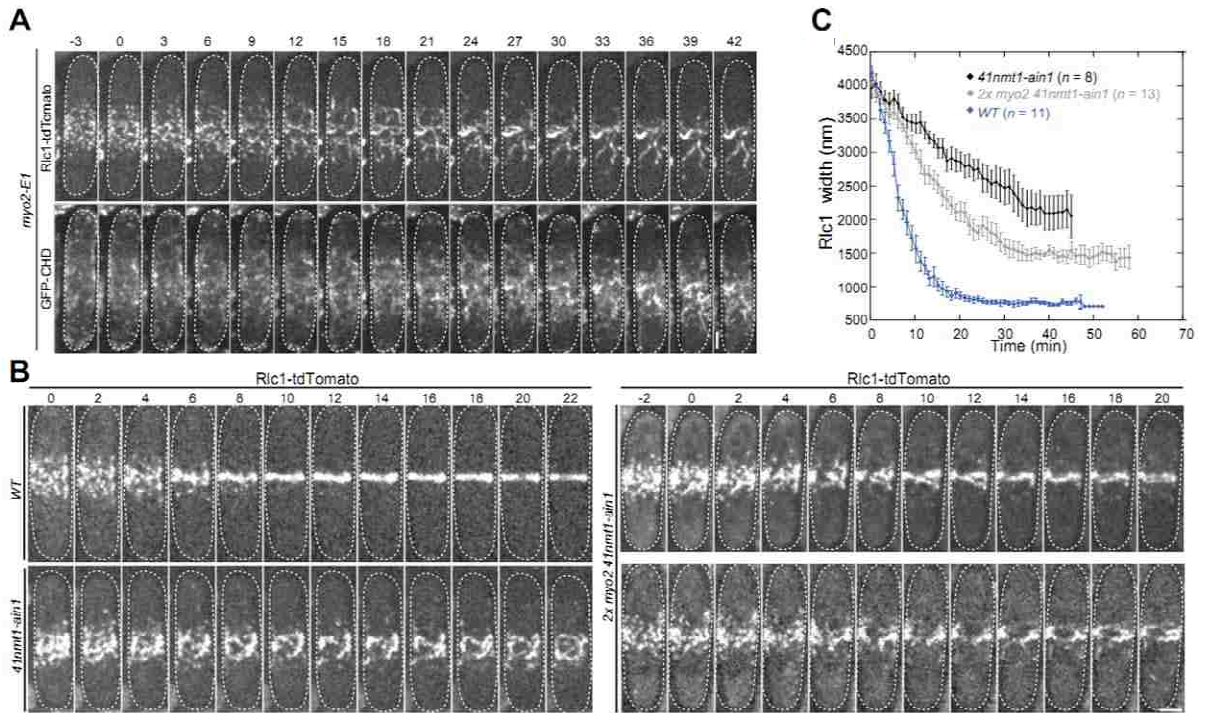


**Figure 28:** Experimental result showing cooperation between Myo2 activity and Ain1 cross-linking (D. Laporte). (A) Rlc1 nodes form unstable linear structures with defective myosin-II activity. Time courses of Rlc1-tdTomato and GFP-CHD localization in *myo2-E1* cells grown at 36°C for 2 h and imaged at 36°C. *41nmt1-GFP-CHD* was induced in EMM5S for 24 h at 25°C before shifting to 36°C. (B) Doubling Myo2 level partially rescues the ring-formation defect in Ain1 overexpression cells. Time courses of Rlc1 localization in wt, *41nmt1-ain1*, and two representative *2x myo2 41nmt1-ain1* cells. Strains were grown 22 h in EMM5S. (C) Width of Rlc1 broad band over time (mean  $\pm$  SEM). Times in min. Bars, 2  $\mu$ m.

Finally, we also used the model described in this chapter to simulate conditions observed for *cdc25-22* cells. As shown in Figure 3B, Figure 11C and D, filamentous structures that look like double rings are observed in these cells. We distributed 100 nodes in a Gaussian band of standard deviation  $\sigma = 1.6 \mu\text{m}$  as seen in *cdc25-22* cells [13]. A high concentration of cross-linkers in these cells is expected since *cdc25-22* cells grow longer and their extended cell cycle probably causes protein accumulation [13]. In Figure 29 parameter  $\alpha$  is varied. For large  $\alpha$ , the case that corresponds to a large concentration of

cross-linkers, double-ring structures are observed. Thus, the model developed in this chapter successfully reproduced meshwork defects that are typical for *cdc25-22* cells.

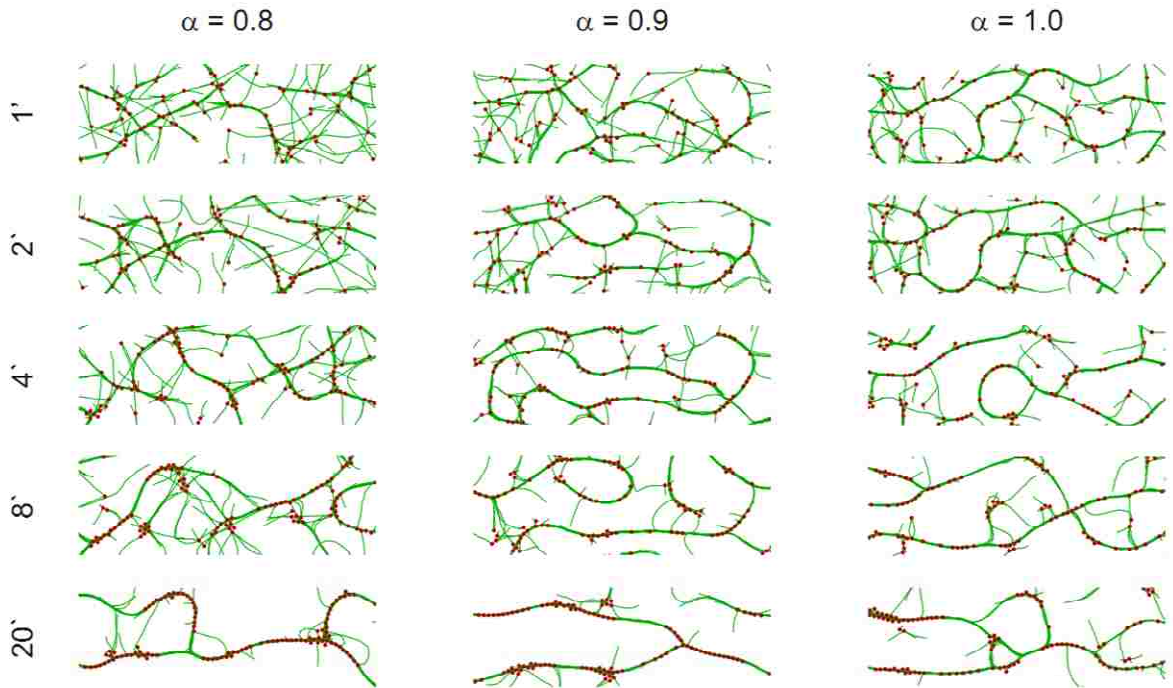


**Figure 29:** Simulations of node condensation in *cdc25-22* cells. Nodes are distributed in a Gaussian band of standard deviation  $\sigma = 1.6 \mu\text{m}$  [13]. For larger  $\alpha$ , stable double rings form. Compare with experimental results of Figure 3B, Figure 11C and D.

### 6.3. Discussion

I showed numerically that starting from an approximately Gaussian distribution along the long cell axis, nodes condense into clumps/rings/meshworks depending on the actin filament cross-linking, as observed experimentally by Damien Laporte and Jian-Qiu Wu. Without the cross-linkers, nodes condense into clumps that attract surrounding nodes. By contrast, nodes condense into numerous linear structures that form meshworks when *Ain1* is overexpressed. This stabilization of actin cytoskeleton by  $\alpha$ -actinin is consistent with a mammalian  $\alpha$ -actinin study [78].

An important assumption in my simulations was the fact that cross-linking activity (described by parameters  $\alpha$  and  $k_{\text{cross}}$ ) is dynamic. This allows actin filaments to slide past one another as they polymerize. In the simulations, the resistance force between two actin filaments polymerizing at 100 nm/s against one another (as in Figure 23B) is of order  $\alpha k_{\text{cross}} l_0 \approx 0.07$  pN, per length  $l_0$ . At that speed, the drag force by an  $\alpha$ -actinin molecule *in vitro* is estimated to be 0.012 pN [79], corresponding to a few  $\alpha$ -actinin molecules per micron of actin filaments in the simulations. With these numbers, the total amount of cross-linkers in simulations is close to that measured in experiments (see Figure 25C). This indicates that our chosen values for  $\alpha$  and  $k_{\text{cross}}$  are realistic.

The importance of dynamic cross-linking is that it provides the ability of antiparallel bundle formation. Fim1 bundles actin filaments in both parallel and antiparallel orientations [60] and  $\alpha$ -actinin is known to have this ability in other cell systems [80], both consistent with the assumption in our simulations. With this assumption, the simulations reveal that different filament orientations may prevail depending on system parameters, see Figure 26D. Actin filaments that grow out of clumps are cross-linked in a parallel fashion while those that link linear node structures have both parallel and antiparallel orientations Figure 23. These different organizations of actin filaments in different cells may explain both node-dependent and independent pathways for contractile-ring formation [55, 81-84].

By using the model of this Chapter we successfully reproduced linear structures, rings, and meshworks. These actomyosin structures emerge in a natural way from the collective interactions of our model components (nodes, filaments, and cross-linkers) compared to the imposed local alignment mechanism of Chapter 4.

## 7. Conclusion

In this thesis I presented theoretical work supported by experimental results by the other groups and by collaborators Damien Laporte and Jian-Qiu Wu from The Ohio State University. Simulations supported a mechanism of contractile ring formation in fission yeast that includes for the following basic components:

(i) actin filaments polymerizing out of actin nucleator formin (Cdc12p)

(ii) actin turnover, likely by cofilin (Adf1p) severing

(iii) myosin motors (Myo2p) that exert forces on actin filaments

(iv) actin filament cross-linkers (Ain1p, Fim1p) that arrange filaments into bundles.

During ring formation, various other proteins ( $\approx 130$ ) appear at the cell equator and contribute to the ring formation and maturation process [28, 54, 85]. Since the function of many of these different protein components is still unknown, future experiments and modeling will be required to determine their precise mechanistic role. These future studies will test how successful the current model is in capturing the main mechanism of contractile ring formation and the origin of clumps/rings/meshworks in different mutants.

In fission yeast, once the contractile ring is formed it matures for  $\approx 10$  minutes before constriction. During this maturation time various protein components are recruited from the cytoplasm to the ring such as actin filament capping proteins and unconventional myosin II (Myp2) [54]. Our model can be used as a starting point in



future explorations of the origin of a contractile forces in the ring constriction [14, 86-88].

Different organisms form different actomyosin contractile units such as stress fibers, vertical junctions, and muscle fibers [89-92]. Models similar to the ones developed in this thesis could be applied to the formation kinetics of these different systems. Thus, our approach can contribute to better understanding of these highly complex, but presumably evolutionary-preserved actomyosin structures.

Another future challenge would be to determine the exact mechanisms of how the different steps (node formation, node movements, and onset of constriction) during cytokinesis are controlled by signaling molecules [55, 56, 93]. A mechanism of how cell size coordinates with the mitotic entry in fission yeast was proposed in 2008 [94, 95]. It was shown that protein Pom1 which localizes to cell tips regulates a signaling network in interphase nodes, which are precursors to the cytokinesis nodes of this work. Most importantly, the signaling pathway responsible for formin Cdc12p activation and its recruitment into nodes is still unknown [54]. Future investigations of signaling pathways that control cytokinesis, as well as studies to resolve the exact structure of cortical nodes [24], would address these challenging problems. Using quantitative modeling and numerical simulations in combination with new experimental techniques such as high resolution imaging [96-100], these challenging problems may be successfully resolved.

# Appendix

## Semi-flexible filament simulation

In Chapter 6, actin filaments were simulated as semi-flexible polymers as in [70, 71]. Actin filaments were simulated in 2D as strings of beads connected with springs of equilibrium length  $l_0$ . We used  $l_0 = 0.2 \mu\text{m}$  (value of order the node size, the smallest scale or relevance in the simulations). For free filaments Langevin dynamics was used to solve for the position  $\mathbf{r}_i(t)$  of the  $i^{\text{th}}$  filament bead [70, 71]:

$$\zeta_b \frac{d\mathbf{r}_i}{dt} = \mathbf{F}_i^{\text{spr}} + \mathbf{F}_i^{\text{bend}} + \mathbf{F}_i^{\text{stoch}}, \quad i \in \{1, 2, \dots, N\}. \quad 16$$

Here  $N$  is the total number of beads,  $\zeta_b$  is the drag coefficient of a filament segment of length  $l_0$ . For simplicity, we approximate the drag coefficient to be the same along all directions ( $\zeta_b = \zeta_{\perp} = \zeta_{\parallel}$ ). To estimate  $\zeta_b$ , we used  $\zeta_{\perp} = 4\pi\eta l_0 / [\ln(l_0/2a) + 0.84] = 0.216 \text{ pN s}/\mu\text{m}$  for a rod of length  $l_0$  and radius  $a = 3.5 \text{ nm}$  and  $\eta = 350 \eta_{\text{water}} = 0.301 \text{ Pa s}$  as the cytoplasmic viscosity [101]. The forces on the right hand side of Eq. (1) are as follows.

$$\textit{Spring force: } \mathbf{F}_i^{\text{sp}} = -\frac{\partial E^{\text{spring}}}{\partial \mathbf{r}_i} = -\frac{k}{2} \sum_{j=1}^{N-1} \frac{\partial (|\mathbf{r}_{j+1} - \mathbf{r}_j| - l_0)^2}{\partial \mathbf{r}_i}.$$

This is the force by the neighboring springs, where  $E^{\text{spring}}$  is the total spring energy. We used a spring constant  $k = 150 \text{ pN}/\mu\text{m}$ , a value large enough to maintain filament length but also small enough to allow small enough forces and thus use of large integration time steps (we note that this value is smaller than the value of the spring constant corresponding to the Young's

module  $E$  of an actin filament,  $k = ES/l_0 \approx 346 \cdot 10^3$  pN/ $\mu\text{m}$  where  $S$  is actin filament cross-section area [102]).

Bending force:  $\mathbf{F}_i^{\text{bend}} = -\frac{\partial E^{\text{bend}}}{\partial \mathbf{r}_i} = \frac{\kappa}{l_0} \sum_{j=2}^{N-1} \frac{\partial (\mathbf{t}_j \cdot \mathbf{t}_{j-1})}{\partial \mathbf{r}_i}$  is the force due to the elastic energy of bending,  $E^{\text{bend}}$  [71, 103, 104]. Here  $\mathbf{t}_j \equiv \frac{\mathbf{r}_{j+1} - \mathbf{r}_j}{|\mathbf{r}_{j+1} - \mathbf{r}_j|}$  is the local unit tangent vector. The flexural rigidity  $\kappa$  in thermal equilibrium satisfies  $\kappa = k_B T / l_p$ , where  $k_B$  is Boltzmann's constant,  $T$  is temperature, and  $l_p = 10 \mu\text{m}$  the equilibrium persistence length [105].

Thermal force:  $\mathbf{F}_i^{\text{stoch}}$  is a random force satisfying  $\left\langle \mathbf{F}_i^{\text{stoch}} \mathbf{F}_i^{\text{stoch} T} \right\rangle_{\alpha, \beta} = \frac{2k_B T \zeta_b}{\Delta t} \hat{I}_{\alpha, \beta}$ ,

where  $\hat{I}_{\alpha, \beta}$  is the second order unit tensor, and  $\Delta t$  is the simulation time step [70].

### Equilibrium properties of semi-flexible filaments

We verified that the equilibrium properties of simulated filaments match with the theoretical expressions derived from previous analytical calculations. The persistence length of simulated filament was calculated using three different methods, as follows:

(i) The first method involves measuring the tangent correlation function as in [101], see Figure 30A and B. The tangent correlation function for semi-flexible filaments in 2D satisfies the following equation [101]:

$$\langle \hat{t}(l) \cdot \hat{t}(l + \Delta l) \rangle = e^{-\Delta l / 2l_p}. \quad 17$$

Here  $l_p$  is the persistence length of the filament. Using different filament contour lengths, we confirmed that the tangent correlation function of simulated filaments decays exponentially, and maintains the correct persistence length over time, see Figure 30.

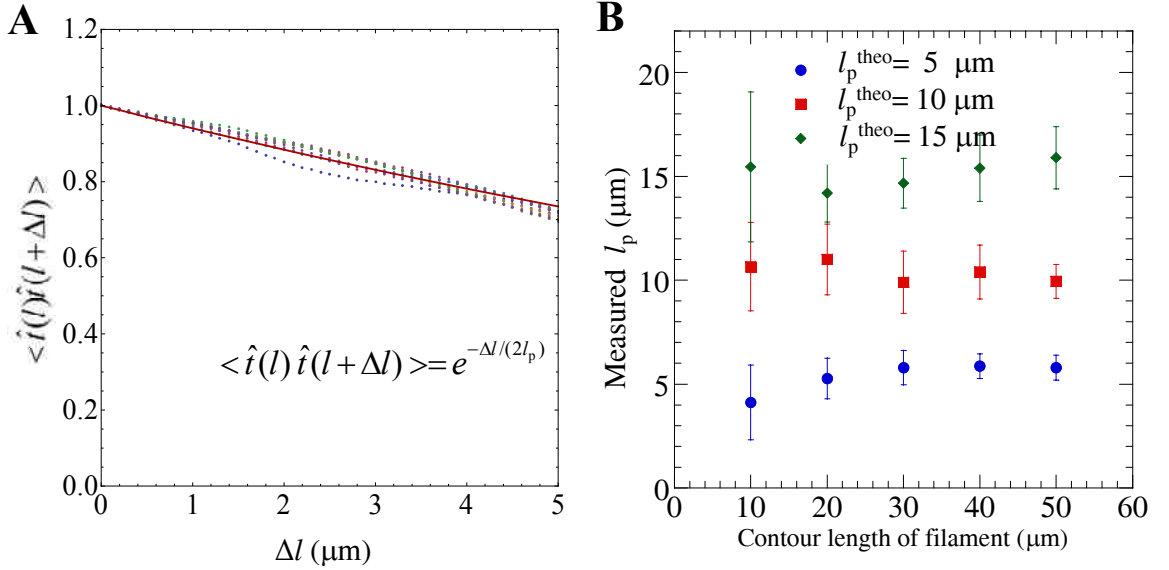


**Figure 30:** Tangent correlation function analysis of semi-flexible filaments in thermal equilibrium. (A) Tangent correlation function for a semi-flexible filament collected every second for times between 50s and 60s.  $N = 300$ ,  $l_0 = 0.1 \mu\text{m}$ ,  $l_p = 10 \mu\text{m}$ ,  $k = 150 \text{ pN}/\mu\text{m}$ ,  $dt = 10^{-5} \text{ s}$ . Measurements were collected between 50-60s every 1s and are plotted with dashed lines. Thick red line is a theoretical curve plotted with  $l_p = 10 \mu\text{m}$ . The average of the tangent correlations is calculated as an average along the filament. (B) Persistence length is measured using method as in (A). Each measurement is repeated 10 times and the average  $\pm$  STD is plotted, for different total lengths.

(ii) The second method involves measuring the curvature distribution statistics

[52]. The curvature distribution obeys Boltzmann distribution and for 2D is given by:

$$P_{2D}(\kappa) = \sqrt{\frac{2l_0 l_p}{\pi}} e^{-l_0 l_p \kappa^2 / 2}. \quad 18$$

Here  $l_0$  is the equilibrium distance between neighboring filament beads and

$\kappa \equiv \left| \frac{d\hat{t}}{ds} \right| = \left| \frac{d^2\vec{r}}{ds^2} \right|$  is the local curvature of the filament. Using this method we confirmed

that simulations maintain the right thermal-equilibrium persistence length, see Figure 31.

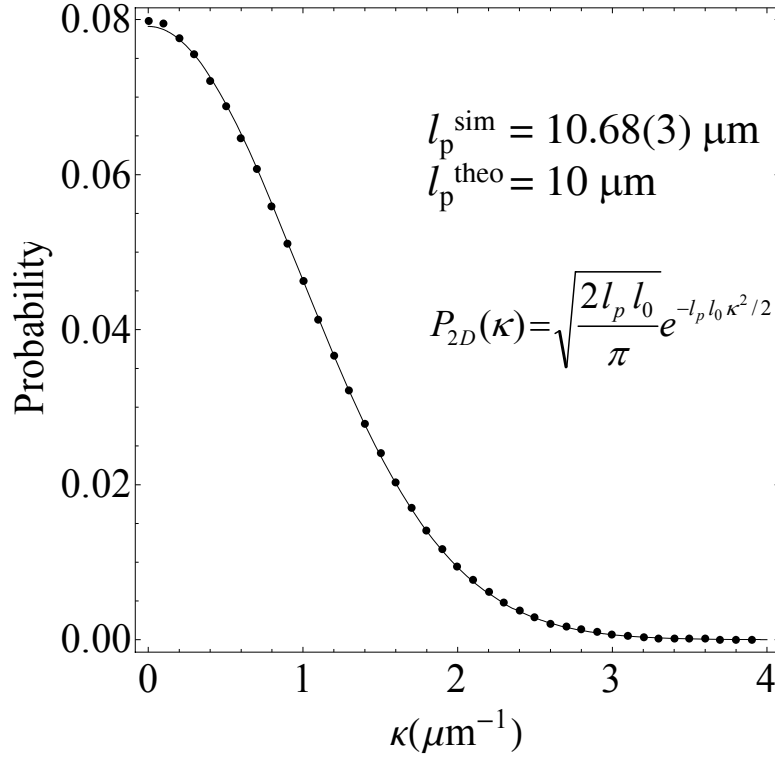


**Figure 31:** Curvature distribution of semi-flexible filaments. Curvature distribution of semi-flexible filament ( $N = 40$ ,  $l_0 = 0.1 \mu\text{m}$ ,  $l_p = 10 \mu\text{m}$ ,  $k = 150 \text{ pN}/\mu\text{m}$ ,  $dt = 10^{-6} \text{ s}$ ) is measured every  $dt$  between 10s and 10.05s. Curvatures are collected for all filament segments except for the first two and last two. Line is a Gaussian fit.

(iii) The third method involves measuring filament Fourier modes as in [105], see

Figure 32. For a given  $n^{\text{th}}$  Fourier mode amplitude,  $a_n$ , it holds:

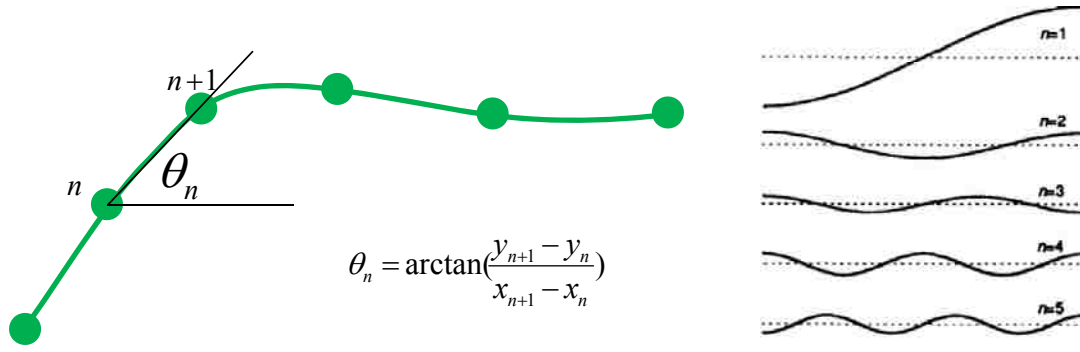


**Figure 32:** Cartoon showing how the Fourier modes are calculated [105].

$$\theta(s) = \sum_{n=1} \theta_n(s) = \sum_{n=1} a_n \cos\left(\frac{n\pi s}{L}\right), \quad 19$$

where

$$a_n = \sqrt{\frac{2}{L}} \int_0^L ds \theta(s) \cos\left(\frac{n\pi s}{L}\right); \quad \langle a_n^2 \rangle = \frac{1}{l_p} \left(\frac{L}{n\pi}\right)^2. \quad 20$$

Here  $L$  is the total length of the simulated filament. In Figure 33 we confirmed that simulations agree with Equation 20 (right), with the correct value of  $l_p$ .

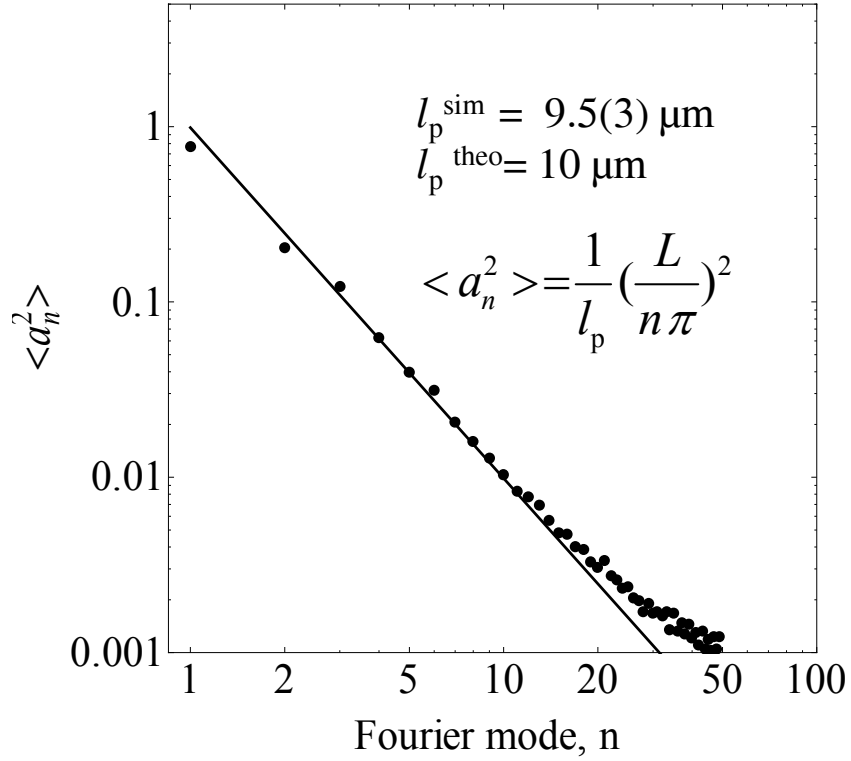


**Figure 33:** Fourier mode analysis. Amplitude of Fourier modes were collected every 1s, during 10-800s of simulation ( $N = 100$ ,  $l_0 = 0.1 \mu\text{m}$ ,  $dt = 10^{-5} \text{ s}$ ,  $k = 150 \text{ pN}/\mu\text{m}$ ).

The above all three methods show that simulations reproduce the correct equilibrium statistics. Once the static properties were confirmed, we investigated the dynamic properties of simulated semi-flexible filaments, see the next Section.

### **Dynamic properties of semi-flexible filaments**

To study the dynamic properties of semi-flexible filaments we measured the relaxation time of each Fourier mode, see Figure 34. In the inset of Figure 34 the amplitude of the

first three Fourier modes is plotted vs time. From these measurements we calculated auto-correlation function for each mode,  $R_{a_n}(\tau)$  :

$$R_{a_n}(\tau) = \frac{\int_0^{T-\tau} dt (a_n(t) - \bar{a}_n)(a_n(t+\tau) - \bar{a}_n)}{\int_0^T dt (a_n(t) - \bar{a}_n)^2}, \quad \bar{a}_n = \int_0^T dt a_n(t) / T. \quad 21$$

$R_{a_n}(\tau)$  vs  $\tau$  is shown in Figure 34 A. Each  $R_{a_n}(\tau)$  satisfies  $R_{a_n}(\tau) \propto e^{-\tau/\tau_n}$  [105], where

$\tau_n = \frac{c_{\perp}}{\kappa} \left( \frac{L}{\pi(n+1/2)} \right)^4$  is the typical decay time of the  $n^{\text{th}}$  Fourier mode amplitude. In

Figure 34B we show that simulations reproduce the correct dependence of the  $\tau_n$ .



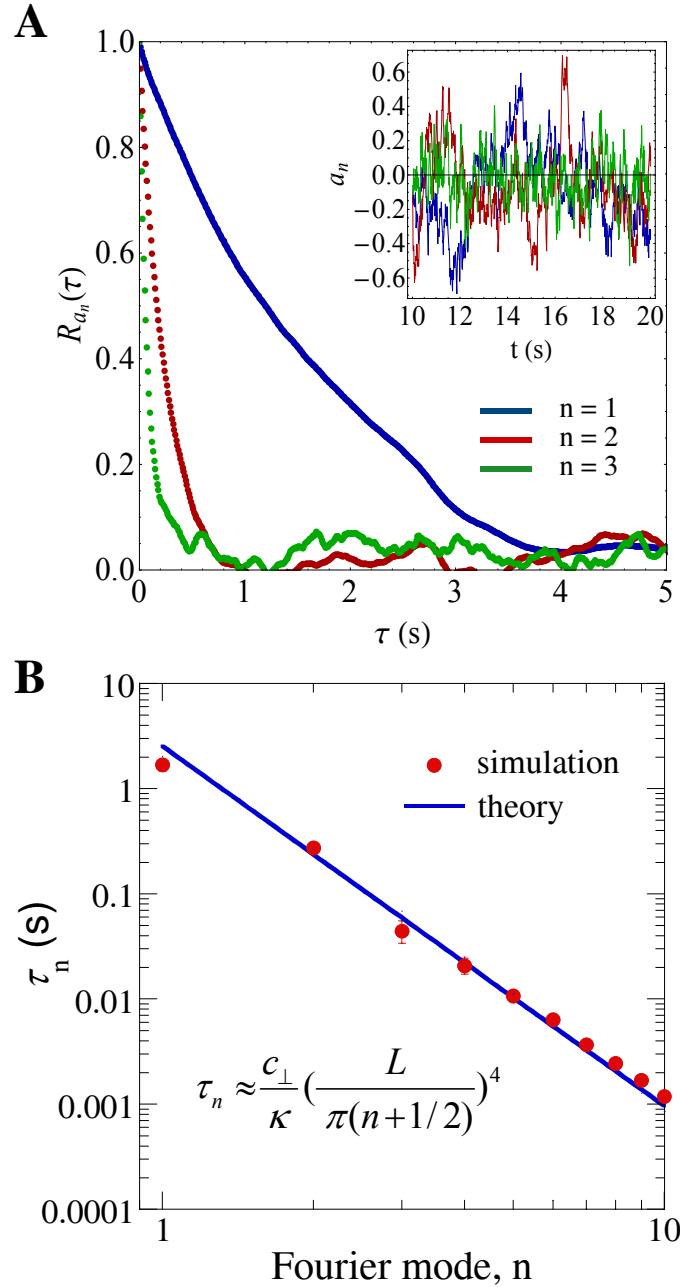
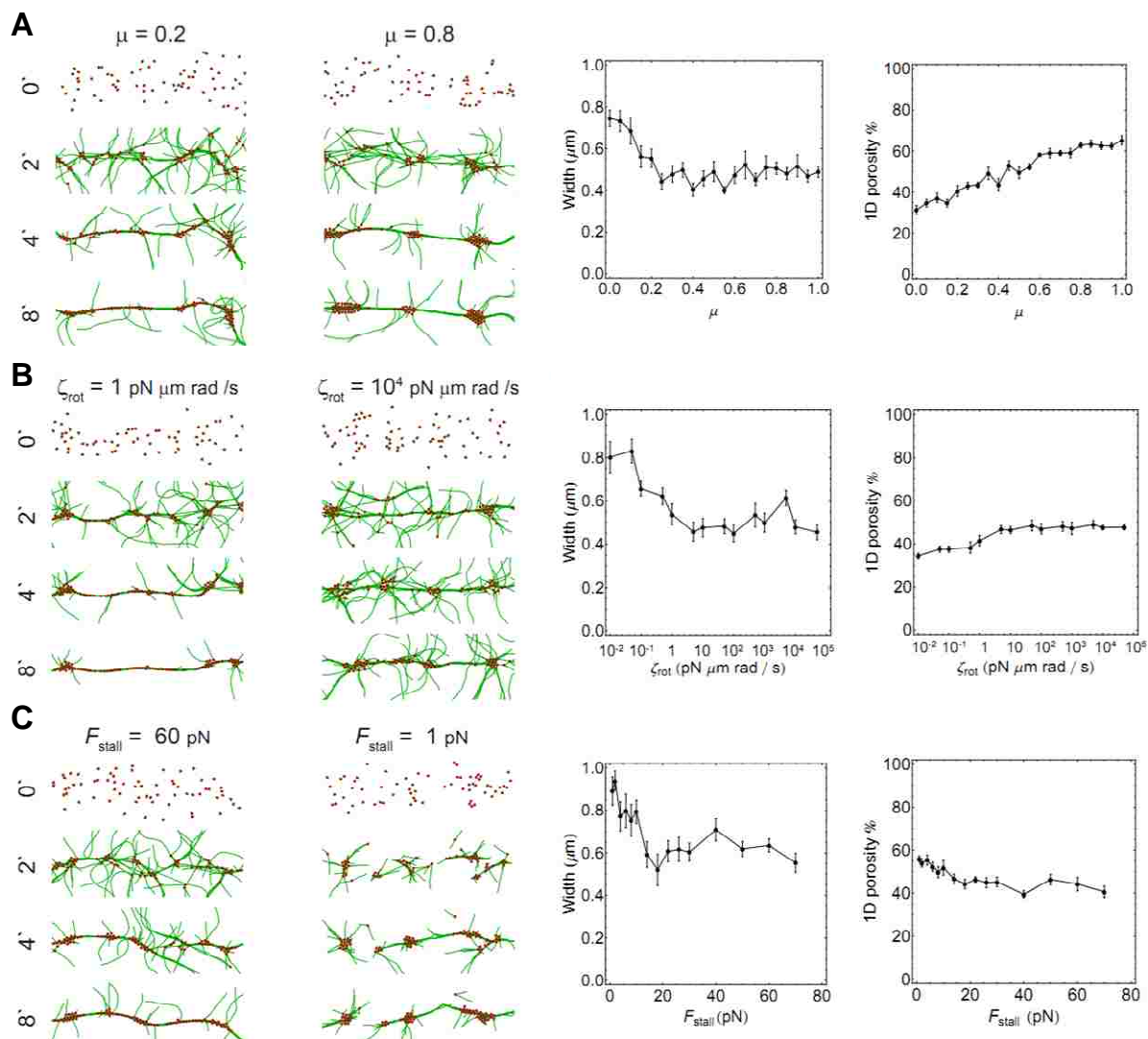
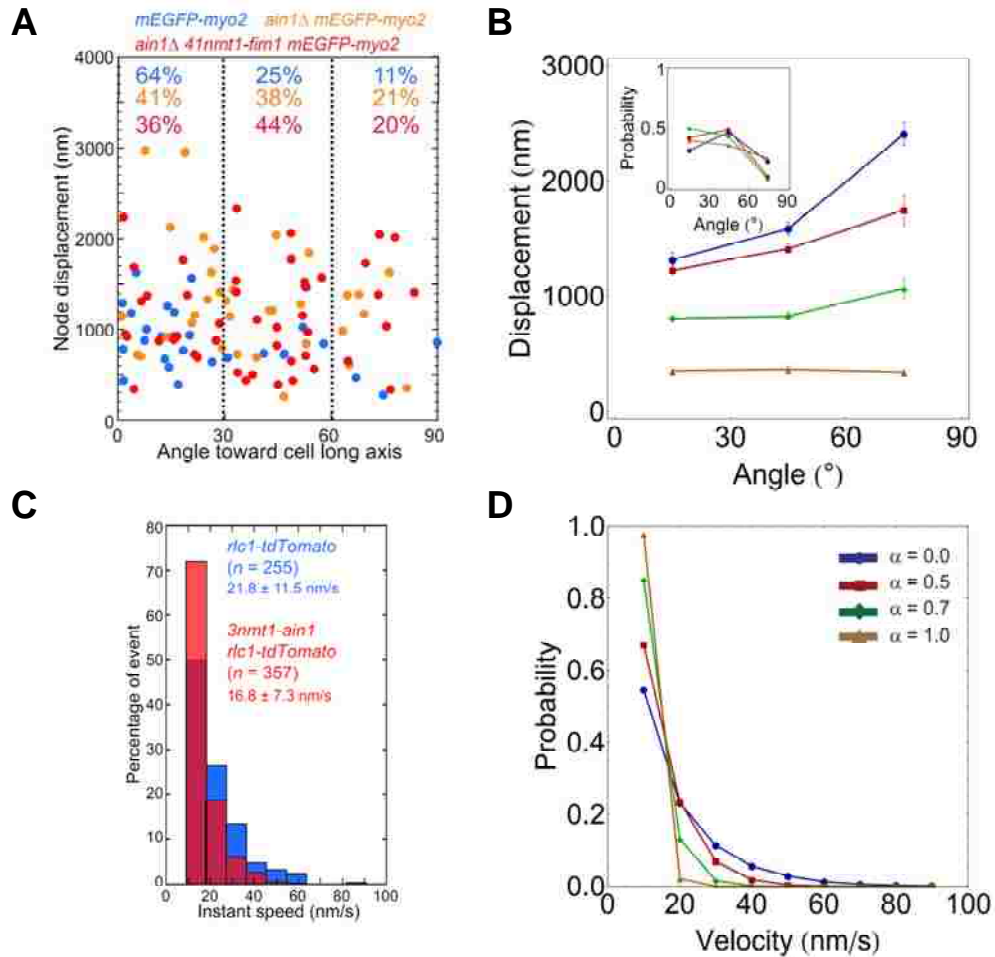


**Figure 34:** Dynamic properties of semi-flexible filaments in the thermal equilibrium. In all simulations we used  $N = 100$ ,  $l_0 = 0.1 \mu\text{m}$ ,  $dt = 10^{-5} \text{ s}$ ,  $k = 150 \text{ pN}/\mu\text{m}$ , and  $\eta = \eta_{\text{water}}$ . (A) Amplitudes of Fourier modes over time for a semi-flexible filament are shown in inset of panel (A). Autocorrelation function was calculated for each  $a_n$  and plotted in (A). Calculation is only shown for first 3 Fourier mode amplitudes. Calculated autocorrelation functions are fitted to exponentials and the decay time is obtained for each mode. (B) Decay times vs Fourier mode is plotted. First three Fourier modes are collected between 10-200s, every 0.01s, while all higher modes are collected between 10-13s every 0.0001s. Each measurement is repeated 10 times and average  $\pm$  STD is plotted.

## Supplementary figures



**Supplementary Figure 1:** Node condensation dependence on parameters of model described in Chapter 6. (A) Snapshots and graphs (calculated at 500 s, mean of 10 simulations, error bars:  $\pm$  SEM), showing the effect of changes in model parameter  $\mu$  describing the reduction of myosin pulling force per filament by nodes inside actin bundles, with all other parameters unchanged. For large  $\mu$  (small reduction), myosin pulling forces inside bundles become too strong to maintain ring integrity. We used  $\mu = 0.3$  in the Chapter 6. (Figure 23). (B) Same as A, but changing parameter  $\zeta_{rot}$  describing resistance to rotation of polymerization direction. For small  $\zeta_{rot}$ , filaments rotate and align within a single bundle. (C) Same as A and B, but changing the polymerization stall force  $F_{stall}^{pol}$ . In the presence of cross-linking, force-induced reduction of the polymerization rate causes the nodes to align in small disconnected clumps.



**Supplementary Figure 2:** Node movement statistics. Experimental data in left column (D. Laporte); simulation data in right column. (A) Angles between directions of node displacements and the long cell axis were plotted versus the node displacements observed during ~3 min. The percentage of measurements in each category for each strain is indicated. (B) Node displacement vs. angle of displacement. Nodes whose initial distance from the center was larger than 0.9  $\mu\text{m}$  were tracked in the simulations for the first 150 s. We then measured the angle between a line joining the initial node position to the final node position and the axis parallel to the long axis of the cell. The displacement was the Euclidean distance between initial and final points. We grouped displacement measurements into three bins: 0-30, 30-60, and 60-90 degrees. Without cross-linking, nodes travel longer distances within the same time; those that move at larger angles also move over longer distances, similarly to experiment. Error bars are  $\pm$  SEM ( $n = 10$  simulations). Inset: Probability of node displacements vs. angle of displacement and cross-linking parameter  $\alpha$  shows a trend similar to experiment. (C) Rlc1-tdTomato node movements were tracked every 10 s after the beginning of node condensation; node speed distribution is shown. Nodes in *3nmt1-ain1* strains (red) display a slower speed compare to those in wild-type (blue) (D) Probability of node velocities for different values of parameter  $\alpha$ . Node velocities were measured over a 5 s interval during the first 200 s after onset of condensation. Only velocities larger than 10 nm/s are shown.

## Supplementary Tables

Parameter	Successful range	Used value	Comments
$l_x$ (nm)	0 - 80	50	Effective cross-linker size. For values larger than 80 nm, actin filaments form thick bundles.
$r_{\text{capt}}$ (nm)	100 - 200	150	Value representing the node size. For values less than $\sim 100$ nm, connections are rare and condensation is slower than experiments. Values larger than 200 nm lead to multiple connections and fast condensation.
$k_{\text{bead-node}}$ (pN/ $\mu\text{m}$ )	1 - 3	2	This empirical parameter was tuned to allow long-lived connections between nodes and filament beads, without simultaneously pinning the beads to the nodes. Values less than 1 pN/ $\mu\text{m}$ are too weak to keep actin filament beads near nodes. Values larger than 3 pN are too strong to allow passage of myosin nodes from bead to bead along growing actin filaments.
$t_{\text{turn}}$ (s)	15 - 30	20	Lifetime of actin filaments. Values less than 15 s lead to very short actin filaments that promote clump formation. Values of order 40 s or larger generate very long filaments that cross-link into bundles, which run through nodes and promote node clump formation.
$F_{\text{myo}}$ (pN)	2 - 12	4	Myosin pulling force. Value that reproduces observed node speeds.
$F_{\text{rep}}$ (pN)	> 5	80	Short-range node repulsive force. Forces less than 5 pN cannot counteract the forces due to node connections

**Supplementary Table 1:** SCPR model parameters used in simulations of Chapter 6.

## Bibliography

1. Liverpool, T.B. and M.C. Marchetti, *Instabilities of isotropic solutions of active polar filaments*. Phys Rev Lett, 2003. **90**: p. 138102.
2. Cytrynbaum, E.N., V. Rodionov, and A. Mogilner, *Computational model of dynein-dependent self-organization of microtubule asters*. J. Cell Sci., 2004. **117**(Pt 8): p. 1381-1397.
3. Kruse, K., et al., *Asters, Vortices, and Rotating Spirals in Active Gels of Polar Filaments*. Phys. Rev. Lett., 2004. **92**(7): p. 078101--.
4. Haviv, L., et al., *Reconstitution of the transition from lamellipodium to filopodium in a membrane-free system*. Proc Natl Acad Sci U S A, 2006. **103**(13): p. 4906--4911.
5. Liverpool, T.B. and M.C. Marchetti, *Rheology of active filament solutions*. Phys. Rev. Lett., 2006. **97**: p. 268101.
6. Ziebert, F., I.S. Aranson, and L.S. Tsimring, *Effects of cross-linkers on motor-mediated filament organization*. New Journal of Physics, 2007. **9**: p. 421.
7. Shlomovitz, R. and N.S. Gov, *Membrane waves driven by actin and Myosin*. Phys Rev Lett, 2007. **98**(16): p. 168103.
8. Shlomovitz, R. and N.S. Gov, *Physical model of contractile ring initiation in dividing cells*. Biophys. J., 2008. **94**: p. 1155--1168.

9. Kraikivski, P., B.M. Slepchenko, and I.L. Novak, *Actin bundling: initiation mechanisms and kinetics*. Phys. Rev. Lett., 2008. **101**: p. 128102.
10. Chelakkot, R., R. Lipowsky, and T. Gruhn, *Self-assembling network and bundle structures in systems of rods and crosslinkers - A Monte Carlo study*. Soft Matter, 2009. **5**: p. 1504-1513.
11. Brill-Karniely, Y., et al., *From branched networks of actin filaments to bundles*. Chemphyschem, 2009. **10**(16): p. 2818--2827.
12. Walcott, S. and S.X. Sun, *A mechanical model of actin stress fiber formation and substrate elasticity sensing in adherent cells*. Proc Natl Acad Sci U S A, 2010. **107**(17): p. 7757--7762.
13. Vavylonis, D., et al., *Assembly mechanism of the contractile ring for cytokinesis by fission yeast*. Science, 2008. **319**: p. 97--100.
14. Zumdieck, A., et al., *Continuum description of the cytoskeleton: ring formation in the cell cortex*. Phys. Rev. Lett., 2005. **95**: p. 258103.
15. Nédélec, F.J., et al., *Self-organization of microtubules and motors*. Nature, 1997. **389**: p. 305--308.
16. Mogilner, A., R. Wollman, and W.F. Marshall, *Quantitative modeling in cell biology: what is it good for?* Dev. Cell, 2006. **11**(3): p. 279-287.
17. Wu, J.Q., et al., *Assembly of the cytokinetic contractile ring from a broad band of nodes in fission yeast*. J. Cell Biol., 2006. **174**: p. 391--402.
18. Wu, J.Q. and T.D. Pollard, *Counting cytokinesis proteins globally and locally in fission yeast*. Science, 2005. **310**: p. 310--314.

19. Drake, T. and D. Vavylonis, *Cytoskeletal dynamics in fission yeast: a review of models for polarization and division*. HFSP J, 2010. **4**: p. 122-130.
20. Arai, R. and I. Mabuchi, *F-actin ring formation and the role of F-actin cables in the fission yeast *Schizosaccharomyces pombe**. J. Cell Sci., 2002. **115**: p. 887--898.
21. Yonetani, A. and F. Chang, *Regulation of cytokinesis by the formin *cdc12p**. Curr Biol, 2010. **20**(6): p. 561--566.
22. Wachtler, V., et al., *Cell cycle-dependent roles for the FCH-domain protein *Cdc15p* in formation of the actomyosin ring in *Schizosaccharomyces pombe**. Mol Biol Cell, 2006. **17**(7): p. 3254-66.
23. Huang, Y., H. Y, and M.K. Balasubramanian, *Assembly of normal actomyosin rings in the absence of *Mid1p* and cortical nodes in fission yeast*. J. Cell Biol., 2008. **183**: p. 979--988.
24. Laporte, D., et al., *Assembly and architecture of precursor nodes during fission yeast cytokinesis*. J Cell Biol, 2011. **192**(6): p. 1005-21.
25. Ojkic, N. and D. Vavylonis, *Kinetics of Myosin node aggregation into a contractile ring*. Phys. Rev. Lett., 2010. **105**(4): p. 048102.
26. Coffman, V.C., et al., *Roles of Formin Nodes and Myosin Motor Activity in *Mid1p*-dependent Contractile-Ring Assembly during Fission Yeast Cytokinesis*. Mol. Biol. Cell, 2009. **20**(24): p. 5195--5210.
27. Chen, Q. and T.D. Pollard, *Actin filament severing by cofilin is more important for assembly than constriction of the cytokinetic contractile ring*. J Cell Biol, 2011. **195**(3): p. 485-98.

28. Hachet, O. and V. Simanis, *Mid1p/anillin and the septation initiation network orchestrate contractile ring assembly for cytokinesis*. Genes Dev, 2008. **22**: p. 3205--3216.
29. Ojkic, N., J.Q. Wu, and D. Vavylonis, *Model of myosin node aggregation into a contractile ring: the effect of local alignment*. J Phys Condens Matter, 2012. **23**(37): p. 374103.
30. Sagot, I., S.K. Klee, and D. Pellman, *Yeast formins regulate cell polarity by controlling the assembly of actin cables*. Nat. Cell Biol., 2002. **4**: p. 42--50.
31. Kovar, D.R., J.Q. Wu, and T.D. Pollard, *Profilin-mediated competition between capping protein and formin Cdc12p during cytokinesis in fission yeast*. Mol. Biol. Cell, 2005. **16**: p. 2313--2324.
32. Kovar, D.R. and T.D. Pollard, *Insertional assembly of actin filament barbed ends in association with formins produces piconewton forces*. Proc. Natl. Acad. Sci. U S A, 2004. **101**: p. 14725--14730.
33. Vavylonis, D., et al., *Model of formin-associated actin filament elongation*. Mol. Cell, 2006. **21**: p. 455-466.
34. Pruyne, D., et al., *Role of Formins in Actin Assembly: Nucleation and Barbed-End Association*. Science, 2002. **297**(5581): p. 612-615.
35. Michelot, A., et al., *Actin-Filament Stochastic Dynamics Mediated by ADF/Cofilin*. Current Biology, 2007. **17**: p. 825-833.
36. Nakano, K. and I.i. Mabuchi, *Actin-depolymerizing protein Adf1 is required for formation and maintenance of the contractile ring during cytokinesis in fission yeast*. Mol. Biol. Cell, 2006. **17**: p. 1933--1945.



37. Coffman, V.C., et al., *Roles of Formin Nodes and Myosin Motor Activity in Mid1p-dependent Contractile-Ring Assembly during Fission Yeast Cytokinesis*. Mol. Biol. Cell, 2009: p. E09-05-0428.
38. Yonetani, A., et al., *Regulation and Targeting of the Fission Yeast Formin cdc12p in Cytokinesis*. Mol. Biol. Cell, 2008.
39. Bathe, M. and F. Chang, *Cytokinesis and the contractile ring in fission yeast: towards a systems-level understanding*. Trends in Microbiology, 2010. **18**(1): p. 38--45.
40. Mishra, M. and S. Oliferenko, *Cytokinesis: catch and drag*. Curr. Biol., 2008. **18**: p. R247--R250.
41. Koenderink, G.H. and et al., *An active biopolymer network controlled by molecular motors*. Proc. Natl. Acad. Sci. U.S.A, 2009. **106**(36): p. 15192-15197.
42. Haviv, L., et al., *A cytoskeletal demolition worker: myosin II acts as an actin depolymerization agent*. J. Mol. Biol., 2008. **375**: p. 325--330.
43. O'Shaughnessy, B. and D. Vavylonis, *The Ultrasensitivity of Living Polymers*. Phys. Rev. Lett., 2003. **90**: p. 118301.
44. de Gennes, P.G., *Kinetics of diffusion-controlled processes in dense polymer systems. I. Nonentangled regimes*. J. Chem. Phys., 1982. **76**(6): p. 3316-3321.
45. Tostevin, F., P.R. ten Wolde, and M. Howard, *Fundamental limits to position determination by concentration gradients*. PLoS Comput. Biol., 2007. **3**(4): p. e78.

46. Wu, J.Q., J. Bähler, and J.R. Pringle, *Roles of a fimbrin and an alpha-actinin-like protein in fission yeast cell polarization and cytokinesis*. Mol. Biol. Cell, 2001. **12**: p. 1061--1077.
47. Skau, C.T. and D.R. Kovar, *Fimbrin and tropomyosin competition regulates endocytosis and cytokinesis kinetics in fission yeast*. Curr Biol, 2010. **20**(16): p. 1415--1422.
48. Takaine, M., O. Numata, and K. Nakano, *Fission yeast IQGAP arranges actin filaments into the cytokinetic contractile ring*. EMBO J, 2009. **28**(20): p. 3117--3131.
49. Celton-Morizur, S., et al., *C-terminal anchoring of mid1p to membranes stabilizes cytokinetic ring position in early mitosis in fission yeast*. Mol. Cell Biol., 2004. **24**: p. 10621--10635.
50. Isambert, H., et al., *Flexibility of actin filaments derived from thermal fluctuations. Effect of bound nucleotide, phalloidin, and muscle regulatory proteins*. J. Biol. Chem., 1995. **270**: p. 11437--11444.
51. McCullough, B.R., et al., *Cofilin increases the bending flexibility of actin filaments: implications for severing and cell mechanics*. J Mol Biol, 2008. **381**(3): p. 550--558.
52. Smith, M.B., et al., *Segmentation and Tracking of Cytoskeletal Filaments Using Open Active Contours*. Cytoskeleton, 2010. **67**(11): p. 693-705.
53. Yang, Y., R.B. Meyer, and M.F. Hagan, *Self-limited self-assembly of chiral filaments*. Phys Rev Lett, 2010. **104**(25): p. 258102.

54. Pollard, T.D. and J.-Q. Wu, *Understanding cytokinesis: lessons from fission yeast*. Nat Rev Mol Cell Biol, 2010. **11**(2): p. 149--155.
55. Roberts-Galbraith, R.H. and K.L. Gould, *Stepping into the ring: the SIN takes on contractile ring assembly*. Genes Dev., 2008. **22**: p. 3082--3088.
56. McCollum, D. and K.L. Gould, *Timing is everything: regulation of mitotic exit and cytokinesis by the MEN and SIN*. Trends Cell Biol, 2001. **11**(2): p. 89--95.
57. Bartles, J.R., *Parallel actin bundles and their multiple actin-bundling proteins*. Curr Opin Cell Biol, 2000. **12**(1): p. 72-8.
58. Nakano, K., et al., *Interactions among a fimbrin, a capping protein, and an actin-depolymerizing factor in organization of the fission yeast actin cytoskeleton*. Mol Biol Cell, 2001. **12**(11): p. 3515-26.
59. Xu, J., D. Wirtz, and T.D. Pollard, *Dynamic cross-linking by alpha-actinin determines the mechanical properties of actin filament networks*. J. Biol. Chem., 1998. **273**: p. 9570-9576.
60. Skau, C.T., et al., *Actin filament bundling by fimbrin is important for endocytosis, cytokinesis, and polarization in fission yeast*. J Biol Chem. **286**(30): p. 26964-77.
61. Skau, C.T. and D.R. Kovar, *Fimbrin and tropomyosin competition regulates endocytosis and cytokinesis kinetics in fission yeast*. Curr Biol. **20**(16): p. 1415-22.
62. Klein, M.G., et al., *Structure of the actin crosslinking core of fimbrin*. Structure, 2004. **12**(6): p. 999-1013.
63. Sjoblom, B., A. Salmazo, and K. Djinovic-Carugo, *Alpha-actinin structure and regulation*. Cell Mol Life Sci, 2008. **65**(17): p. 2688-701.

64. Maciver, S.K., et al., *The actin filament severing protein actophorin promotes the formation of rigid bundles of actin filaments crosslinked with alpha-actinin*. J. Cell Biol., 1991. **115**(6): p. 1621-1628.
65. Sato, M., W.H. Schwarz, and T.D. Pollard, *Dependence of the mechanical-properties of actin alpha-actinin gels on deformation rate*. Nature, 1987. **325**: p. 828-830.
66. Janson, L.W., J.R. Sellers, and D.L. Taylor, *Actin-binding proteins regulate the work performed by myosin II motors on single actin filaments*. Cell Motil Cytoskeleton, 1992. **22**(4): p. 274-80.
67. Alberts, B., et al., *Molecular biology of the cell*. 4th ed. 2002, New York: Garland Science.
68. Wu, J.Q., J. Bahler, and J.R. Pringle, *Roles of a fimbrin and an alpha-actinin-like protein in fission yeast cell polarization and cytokinesis*. Mol. Biol. Cell, 2001. **12**(4): p. 1061-1077.
69. Ojkcic, N., J.Q. Wu, and D. Vavylonis, *Model of myosin node aggregation into a contractile ring: the effect of local alignment*. J Phys Condens Matter. **23**(37): p. 374103.
70. Kim, T., W. Hwang, and R.D. Kamm, *Computational Analysis of a Cross-linked Actin-like Network*. Experimental Mechanics, 2009. **49**(1): p. 91-104.
71. Pasquali, M. and D.C. Morse, *An efficient algorithm for metric correction forces in simulations of linear polymers with constrained bond lengths*. Journal of Chemical Physics, 2002. **116**(5): p. 1834-1838.

72. Coffman, V.C., et al., *Roles of formin nodes and myosin motor activity in Mid1p-dependent contractile-ring assembly during fission yeast cytokinesis*. Mol Biol Cell, 2009. **20**(24): p. 5195-210.
73. Wu, J.-Q. and T.D. Pollard, *Counting cytokinesis proteins globally and locally in fission yeast*. Science, 2005. **310**(5746): p. 310-314.
74. Laporte, D., et al., *Assembly and architecture of precursor nodes during fission yeast cytokinesis*. J Cell Biol. **192**(6): p. 1005-21.
75. Xu, J.Y., D. Wirtz, and T.D. Pollard, *Dynamic cross-linking by alpha-actinin determines the mechanical properties of actin filament networks*. Journal of Biological Chemistry, 1998. **273**(16): p. 9570-9576.
76. Strehle, D., et al., *Transiently crosslinked F-actin bundles*. European Biophysics Journal with Biophysics Letters, 2011. **40**(1): p. 93-101.
77. Stark, B.C., et al., *Tropomyosin and myosin-II cellular levels promote actomyosin ring assembly in fission yeast*. Mol Biol Cell. **21**(6): p. 989-1000.
78. Mukhina, S., Y.L. Wang, and M. Murata-Hori, *Alpha-actinin is required for tightly regulated remodeling of the actin cortical network during cytokinesis*. Dev Cell, 2007. **13**(4): p. 554-65.
79. Greenberg, M.J. and J.R. Moore, *The molecular basis of frictional loads in the in vitro motility assay with applications to the study of the loaded mechanochemistry of molecular motors*. Cytoskeleton (Hoboken), 2010. **67**(5): p. 273-85.
80. Meyer, R.K. and U. Aebi, *Bundling of actin-filaments by alpha-actinin depends on its molecular length*. J. Cell Biol., 1990. **110**: p. 2013-2024.

81. Kamasaki, T., M. Osumi, and I. Mabuchi, *Three-dimensional arrangement of F-actin in the contractile ring of fission yeast*. J Cell Biol, 2007. **178**(5): p. 765-71.
82. Balasubramanian, M.K., E. Bi, and M. Glotzer, *Comparative analysis of cytokinesis in budding yeast, fission yeast and animal cells*. Curr Biol, 2004. **14**(18): p. R806-18.
83. Barr, F.A. and U. Gruneberg, *Cytokinesis: placing and making the final cut*. Cell, 2007. **131**(5): p. 847-60.
84. Pollard, T.D., *Mechanics of cytokinesis in eukaryotes*. Current Opinion in Cell Biology, 2010. **22**(1): p. 50-56.
85. Wu, J.Q., et al., *Cooperation Between the Septins and the Actomyosin Ring and Role of a Cell-Integrity Pathway During Cell Division in Fission Yeast*. Genetics, 2010. **186**(3): p. 897-U232.
86. Zumdieck, A., et al., *Stress generation and filament turnover during actin ring constriction*. PLoS ONE, 2007. **2**(1): p. e696.
87. Carlsson, A.E., *Contractile stress generation by actomyosin gels*. Phys. Rev. E, 2006. **74**: p. 051912.
88. Thoresen, T., M. Lenz, and M.L. Gardel, *Reconstitution of contractile actomyosin bundles*. Biophys J, 2011. **100**(11): p. 2698-705.
89. Rauzi, M., P.F. Lenne, and T. Lecuit, *Planar polarized actomyosin contractile flows control epithelial junction remodelling*. Nature, 2010. **468**(7327): p. 1110-U515.
90. Sanger, J.W., et al., *How to build a myofibril*. J Muscle Res Cell Motil, 2005. **26**(6-8): p. 343-54.

91. Kumar, S., et al., *Viscoelastic Retraction of Single Living Stress Fibers and Its Impact on Cell Shape, Cytoskeletal Organization, and Extracellular Matrix Mechanics*. *Biophys J*, 2006. **90**: p. 3762-3773.
92. Aratyn-Schaus, Y., P.W. Oakes, and M.L. Gardel, *Dynamic and structural signatures of lamellar actomyosin force generation*. *Mol Biol Cell*, 2011. **22**(8): p. 1330-9.
93. Wolfe, B.A. and K.L. Gould, *Split decisions: coordinating cytokinesis in yeast*. *Trends Cell Biol.*, 2005. **15**: p. 10-18.
94. Moseley, J.B., et al., *A spatial gradient coordinates cell size and mitotic entry in fission yeast*. *Nature*, 2009. **459**: p. 857--860.
95. Martin, S.G. and M. Berthelot-Grosjean, *Polar gradients of the DYRK-family kinase Pom1 couple cell length with the cell cycle*. *Nature*, 2009. **459**: p. 852--856.
96. Xu, K., H.P. Babcock, and X. Zhuang, *Dual-objective STORM reveals three-dimensional filament organization in the actin cytoskeleton*. *Nat Methods*, 2012. **9**(2): p. 185-8.
97. Lew, M.D., et al., *Three-dimensional superresolution colocalization of intracellular protein superstructures and the cell surface in live *Caulobacter crescentus**. *Proc Natl Acad Sci U S A*, 2011. **108**(46): p. E1102-10.
98. Manley, S., et al., *High-density mapping of single-molecule trajectories with photoactivated localization microscopy*. *Nat Methods*, 2008. **5**(2): p. 155-7.
99. Betzig, E., et al., *Imaging intracellular fluorescent proteins at nanometer resolution*. *Science*, 2006. **313**(5793): p. 1642-1645.

100. Huang, B., et al., *Whole-cell 3D STORM reveals interactions between cellular structures with nanometer-scale resolution*. Nat Methods, 2008. **5**(12): p. 1047-52.
101. Howard, J., *Mechanics of Motor Proteins and the Cytoskeleton*. 2001: Sinauer Associates.
102. Kojima, H., A. Ishijima, and T. Yanagida, *Direct measurement of stiffness of single actin filaments with and without tropomyosin by in vitro nanomanipulation*. Proc Natl Acad Sci U S A, 1994. **91**(26): p. 12962-6.
103. Pasquali, M., V. Shankar, and D.C. Morse, *Viscoelasticity of dilute solutions of semiflexible polymers*. Phys. Rev. E, 2001. **64**: p. 020802.
104. Montesi, A., D.C. Morse, and M. Pasquali, *Brownian dynamics algorithm for bead-rod semiflexible chain with anisotropic friction*. Journal of Chemical Physics, 2005. **122**(8).
105. Gittes, F., et al., *Flexural rigidity of microtubules and actin filaments measured from thermal fluctuations in shape*. J. Cell Biol., 1993. **120**(4): p. 923-34.



# Vita

**Name and last name:** Nikola Ojkic

**Present address:** 16 Memorial Drive East, Bethlehem, PA 18015, USA

**Phone number:** +1-484-821-7243

**E-mail:** [nidzaojkic@yahoo.com](mailto:nidzaojkic@yahoo.com)

**Date of birth:** January 29<sup>th</sup> 1982

## Education

---

### PhD

2007-2012: *Lehigh University*

*Department: Physics*

*PhD in Physics*

*PhD advisor: Dimitrios Vavylonis*

**GPA: 3.83 / 4.00**

### College

2001-2006: *Faculty of Science, University of Novi Sad*

*Department: Physics*

*Diploma in Physics*

**Average grade: 9.56 / 10.00**

**The 4<sup>th</sup> year at the University of Aveiro in Portugal,  
"Campus Europae" project.**

### Secondary education

1997-2001: *Secondary school: "Jovan Jovanovic Zmaj", Novi Sad, Serbia*

*Course: Science*

**Graduated as valedictorian, class 1997/98**

## Journal articles and conference proceedings

---

1. D. Laporte, **N. Ojkic**, D. Vavylonis and J.-Q. Wu, "Alpha-actinin and fimbrin organize actomyosin bundles during the self-assembly of the contractile ring" (submitted, 2012)
2. **N. Ojkic**, J.-Q. Wu and D. Vavylonis, "Model of Myosin Node Aggregation into a Contractile Ring: the Effect of Local Alignment", *J. Phys.: Condens. Matter*, **23**, 374103 (2011)
3. T. Xu, H. Li, T. Shen, **N. Ojkic**, D. Vavylonis, X. Huang "Extraction and analysis of actin networks based on open active contour models," *Proc. of the IEEE Int'l, Symposium on Biomedical Imaging: From Nano to Macro*, **8**, 1334 (2011)
4. **N. Ojkic** and D. Vavylonis, "Kinetics of Myosin Node Aggregation into a Contractile Ring," *Phys. Rev. Lett.*, **105**, 048102 (2010)

## Conference presentations

---

**APS:** American Physical Society, **ASCB:** The American Society for Cell Biology, **BPS:** Biophysical Society, **EMBO:** European Molecular Biology Organization

- **EMBO** course: Mesoscopic Origins of Cell Behaviors during Tissue Morphogenesis: Biochemical Circuits and Mechanics, 2012, Cargèse, France; talk: “The role of actin filament cross-linker proteins during contractile ring formation in fission yeast”
- **BPS** 2012, San Diego, CA; poster: “Model of condensation of an actomyosin network into a contractile ring for fission yeast cell division: the effects of actin cross-linkers alpha-actinin and fimbrin”
- **ASCB** 2011, Denver, CO; poster: “The condensation of actomyosin network into a contractile ring depends on actin cross-linkers alpha-actinin and fimbrin during fission yeast cytokinesis”
- **BPS** 2011, Baltimore, MD; poster: “Model of the role of actin cross-linker proteins during contractile ring assembly in fission yeast”
- **ASCB** 2010, Philadelphia, PA; poster: ” Model of fission-yeast contractile ring formation with short-range alignment of myosin nodes”
- **Pierre-Gilles de Gennes winter school** 2010, Cargèse, France; poster: “Kinetics of self assembly of the contractile ring from a broad band of cortical nodes”
- **APS** 2009, Pittsburg, PA; oral presentation: “Self-assembly of the yeast actomyosin contractile ring as an aggregation process”
- **BPS** 2009, Boston, MA; poster: “Self-assembly of the yeast actomyosin contractile ring as an aggregation process: kinetics of formation and instability regimes”
- **ASCB** 2008, San Francisco, CA; poster: “Contractile ring assembly in fission yeast: parameter dependence of search, capture, pull and release model”

## Additional Information

---

### Languages:

- Serbian, English: Fluent
- German, Portuguese: Basic level

**Computer skills:** Java, Mathematica, MATLAB

**Interests:** Music, Cycling, Hiking, Biology, Mathematics

Bethlehem PA, USA, May 2012